Integrated Acousto-optics: Steering light with sound waves on a chip

Bingzhao Li

A dissertation
submitted in partial fulfillment of the
requirements for the degree of

Doctor of Philosophy

University of Washington

2022

Reading Committee:

Mo Li, Chair

Arka Majumdar

Sajjad Moazeni

Program Authorized to Offer Degree:
Electrical and Computer Engineering

University of Washington

Abstract

Integrated Acousto-optics: Steering light with sound waves on a chip

Bingzhao Li

Chair of the Supervisory Committee:
Mo Li
Department of Electrical and Computer Engineering

When an acoustic wave propagate inside an optical transparent material, it periodically modulates the permittivity medium due to the elasto-optical effect. This can generate a moving phase grating that can diffract the incident light into one or more orders. Such phenomenon is known as acouto-optic (AO) diffraction which leads to a various of applications such as temporal modulators, spatial modulators, spectral modulators and more.

Historically, the AO diffraction (so called, Brillouin scattering (BS)) was first predicted by Brillouin in 1922 [1]. Ten years later, the phenomenon was experimentally observed by Debye and Sears [2], and Lucas and Biquard [3] successively. Other than than Brillouin's predictions, instead of only one order of diffracted beam, there are many more orders observed. which was later theoretical analyzed by Raman and Nath [4]. Therefore, in terms of the Brillouin scattering, there are two diffraction regimes, the Raman-Nath regime, characterized by the multiple of diffraction orders, and the Bragg regime, characterized by a single diffraction order [5, 6].

The exploitation of acouto-optics has led to demonstrations of a variety of applications and novel physical phenomena in a lot of optical systems and devices [1, 6–12]. The elastic wave can be spontaneously produced by thermal agitation of the environment (i.e., spontaneous Brillouin scattering), or stimulated (narrowly defined to be optically excited) by a strong

light source (i.e., stimulated Brillouin scattering (SBS)). The elastic wave can also be excited by external stimuli, such as optical pulses, thermal shocks, and electrical and magnetic fields.

The acoustic wave involved in the acousto-optical scattering process can be launched in different ways. For example, the elastic wave can be spontaneously produced by thermal agitation of the environment (i.e., spontaneous Brillouin scattering), or thermal excitation and the optomechanical stimulation by radiation pressure and electrostriction. While the former method is the original Brillouin's description, the later one is more explored by recent researchers, especially for the stimulated Brillouin scattering (SBS), [13–15] [15–21] as well as in cavity optomechanical systems [22–25], which feature many intriguing photon-phonon interactions [26]. Meanwhile, the acoustic waves can be also electromechanically excited by the interdigital transducers (IDT) on the piezoelectric material. The IDTs convert radio frequency (RF) and microwave (MW) electromagnetic waves to propagating elastic waves, or in some cases, localized mechanical modes. The advanced electromechanical transducer can achieve near-unity transfer efficiency with compact footprint [27–29].

Such strong acoustic waves have the high scattering efficiency [30], which is essential for the practical applications, especially for the nowadays quantum transduction [31]. The high transfer efficiency from RF power to acoustic power, generated from the electromechanical excitation, leading to a high acoustic wave intensity, is unparalleled with other methods forementioned. In the contrast, in the SBS process, each pump photo can generate at most one phonon. Due to the large frequency difference, (in more than 3 orders), the excitation efficiency is no larger than 10-3. Recently, there are several works using gigahertz electromechanically generated acoustic wave to modulate the guide optical waves inside the waveguides and the cavities [32–38]. Novel physical phenomena has been explored in these works, such as induced transparency [35] and nonreciprocal mode conversion [36], and other advanced optical functionalities [30, 32–35, 37, 38]. Thanks to the development of nanofabrication technology, the state-of-art integrated guided wave acousto-optical device succeed

the conventional acousto-optical devices with significant advances in terms of the power consumption and physical footprint [10, 39–42]. The frequency of the nowadays device can also exceed 10 GHz easily, compared to the previous acousto-optic devices.

More interestingly, the newly emerging integrated phononic circuit is anticipated to complement the functionalities of the photonic and electronic circuits, leading to integrated nano-opto-electro-mechanical systems (NOEMS). Such exciting prospect of integration of the three "x-ons" (photons, phonons and electrons), that implement sophisticated sensing and information processing functionalities through Brillouin scattering in the classical and quantum regimes is attracting increasing research efforts.

In this dissertation, a brief overview of BS processes is introduced first in Chapter 1, including the electromechanical excitation of acoustic waves based on piezoelectric IDTs, configurations of such devices, and some prospective applications of the BS devices in reviewed. What follows the introduction and the theory review is the revised compilation of the author's selected research work, including the acousto-optic beamsteering (AOBS) and the scaling integrated photonic computing in the synthetic frequency dimension.

AOBS device has been successfully simulated and fabricated for the first time in 2021. When light interacts with guided acoustic wave inside the acousto-optic waveguide, the scattered beam can be deflected into the designated directions by controlling the acoustic wave frequency. The introduced frequency upshift of the deflected light beam obeys the BS process, mapping the deflection angle to the controlled acoustic wave frequency. Since the angular position of the object is "labeled" by the frequency of the reflected light, the receiver can determine the object's position without *a priori* knowledge of the outgoing beam angle. Based on this property, a prototype frequency angular resolving (FAR) light-detection-and-ranging (LiDAR) system based on chip-scale AOBS devices has been demonstrated. This work is presented in Chapter 2.

The scaling integrated photonic computing in the synthetic frequency dimension has been successfully demonstrated in 2020. [43] The optomechanical coupling is improved by one order in our heterogeneous AlN-on-SOI platform. With such a strong AO modulation, the large scale vector multiplier in frequency domain is achieved. This work is presented in Chapter 3.

TABLE OF CONTENTS

LIST OF FIGURES

LIST OF TABLES

ACKNOWLEDGMENTS

Pursuing the doctoral degree is one of the most difficult accomplishment I have ever done in my life and there are lots of people I owe thanks to.

First of all I would like to acknowledge my advisor, Prof. Mo Li. I should admit I am very lucky to have such a brilliant supervisor, who is clever, patient, and always hardworking. He not only gave me tons of insightful ideas about my research every time I stuck at some points, but also taught me the right research taste and always keep optimistic to every difficulties. He always encouraged me to broaden my knowledge and view to find my true interests, which made this dissertation thesis possible.

Then I would like to acknowledge all my colleagues in our group, especially, Dr. Huan Li, who taught me almost every single skill I need in my research. He taught me how to start a research in a scientific manner, how to be rigorous in the deduction yet flexible enough in the experiment, and how to assess the whole idea thoroughly. I also want to thank Dr. Han Zhao, who taught me how to wrap up a work and always had inspiring discussions with me, which helps me a lot. I would also thank Dr. Qiyu Liu and Qixuan Lin, without your help, the work in this dissertation cannot be accomplished.

I would like to acknowledge Prof. Arka MaMajumdar, Prof. Sajjad Moazeni, and Prof. Junlan Wang, for reviewing this thesis and serving as my defense committee. I always benefits a lot from the discussion I had with Arka and Sajjad.

I would like to acknowledge my friends in the past six years. Without you I couldn't pass those hard time I have been through. That means a lot to me.

In the end I would like to acknowledge my whole family especially my parents for your endless support and forever love. Mom and dad, to me you are the best parents I could ever have in the world. Although emotional expression is always hard for me, who grew up in a traditional eastern family, I still want to say it loudly, mom and dad, I love you, and

thank you for all what you did.

DEDICATION

To my grandma, Shu-ni Liang, a Chinese lady who cannot read, yet read me the best story in my life. May you rest in peace.

Chapter 1

INTRODUCTION

1.1 Theory of Acousto-Optic Interaction

1.1.1 Elasto-optic effect

The elasto-otpic effect is one of the basic mechanism involved in the AO interaction. It describes the change of refractive index of a transparent optical medium due to the presence of an acoustic wave. Here we first introduce the elasto-optic tensor based on Pockels' phenomenological theory [1]. The acoustic wave propagating inside the medium can be described by the strain tensor S, which is defined as the symmetric part of the deformation gradient

$$S_{ij} = \left(\frac{\partial u_i}{\partial x_j} + \frac{\partial u_j}{\partial x_i} \right) /2 \quad i,j = 1,2,3 \tag{1.1}$$

where u_i is the displacement. Since the strain tensor is symmetric, we can have a contracted notation.

$$S_1 = S_{11}, \quad S_2 = S_{22}, \quad S_3 = S_{33}, \quad S_4 = S_{23}, \quad S_5 = S_{13}, \quad S_6 = S_{12} \tag{1.2}$$

The elasto-optic effect, can be then described by the nonlinear polarization resulting from the change of dielectric tensor $\Delta\varepsilon_{ij}$.

$$\Delta\varepsilon_{ij} = -\varepsilon_{ii}\Delta B_{ij}\varepsilon_{jj} = -n_i^2 n_j^2 \Delta B_{ij} \tag{1.3}$$

where n_i is the refractive index, $\Delta B_{ij} = p_{ijkl}S_{kl}$ is the impermeability tensor, where p_{ijkl} is the elasto-optic tensor. We can further get,

$$\Delta\varepsilon_{ij} = \chi_{ijk}S_{k\ell} \tag{1.4}$$

with the elasto-optic susceptibility tensor,

$$\chi_{ijk\ell} = -n_i^2 n_j^2 p_{ijk\ell} \tag{1.5}$$

Moreover, for anisotropic material, such as alluminum nitride and gallium phosphide, roto-optic effect also needs consideration, as Nelson and Lax discovered. [14] They pointed out that there exists an additional roto-optic susceptibility due to the antisymmetric rotation part of the deformation gradient.

$$\Delta B'_{ij} = p'_{ijkl} R_{kl} \tag{1.6}$$

where $R_{ij} = (S_{ij} - S_{ji})/2$.

For the theory completeness, in the piezoelectric crystal, an indirect elasto-optic effect occurs as the result of the piezoelectric effect and electro-optic effect in succession. The effective elasto-optic tensor is introduced here, [15]

$$p^*_{ij} = p_{ij} - \frac{r_{im} S_m e_{jn} S_n}{\varepsilon_{mn} S_m S_n} \tag{1.7}$$

where p_{ij} is the direct elasto-optic tensor, r_{im} is the electro-optic tensor, e_{jn} is the piezoelectric tensor, ε_{mn} is the dielectric tensor , and S_m is the unit acoustic wave vector. Since we only use nonpiezoelectric material, or low piezoelectric material to achieve the AO interaction in our work, the indirect elasto-optic effect is negligible in our calculation.

1.1.2 Phase matching condition

The phase-matching conditions for the Brillouin scattering process include frequency and wave-vector matching due to the energy and momentum conservation law. Such conditions need to be satisfied in both Brillouin scattering and simulated Brillouin scattering. However, there are two main differences between the phase matching conditions of these two processes. First, for SBS, the process lasts only when phonons are emitted, so the anti-Stokes process can only occur spontaneously, i.e. via thermal phonons. When the pump is completely depleted, the SBS process stops and the Stokes photons are not converted back to pump photons. In contrast, for BS, due to the abundance of electromechanically excited phonons, both Stokes and anti-Stokes processes can occur, and the conversion be-

tween pump and Stokes/anti-Stokes photons can occur in two way happens.

Another major difference is that SBS was only observed in the in-line configuration, while the BS was also demonstrated in the transverse and 2D free-space configurations. The different configurations are classified by the dimensions of the the acoustic beam and optical beam propagation directions. In the in-line configurations, the acoustic beam and the optical beam either co-propagate or counter-propagate in a 1D waveguide. In this case, the phase matching conditions are the same for both SBS and BS process. On the other hand, in a 2D free-space configuration, acoustic and light waves co-propagate in the same 2D waveguide (e.g., a slab waveguide), but in arbitrary directions. Therefore, the phase-matching conditions must be satisfied in two dimensions to account for the different orientations of the wave-vectors. Moreover, with higher acoustic frequency, the optical beam could be even deflected into the light cone inside the free space, requiring the phase matching condition expand to three dimensions. The later two cases apply to BS process only.

Three possible BS configurations are presented in Fig. 1.1, including in-line, lateral, and 2D free-space configurations. For each configuration, EBS processes can be further classified according to the direction (forward, backward, or arbitrary) and wavelength band (interband or intraband) of the scattered light mode relative to the pump light mode.

1.2 Electromechanical excitation of acoustic waves.

In order to excite acoustic waves electromechanically in integrated photonic devices, piezoelectric materials are required [45]. While silicon photonics dominates in integrated photonics applications, it lacks piezoelectricity to excite acoustic waves. Despite its widespread adoption in nanofabrication and semiconductors, silicon is difficult to utilize in AO applications. This is due to the absence of a direct bandgap in silicon, which limits its use in photonics, especially in realizing active optoelectronic devices. In this case, one possible solution could be integrating the piezoelectric materials with silicon to introduce the desired functionality. In addition to silicon, photonic devices can also be also made of transparent

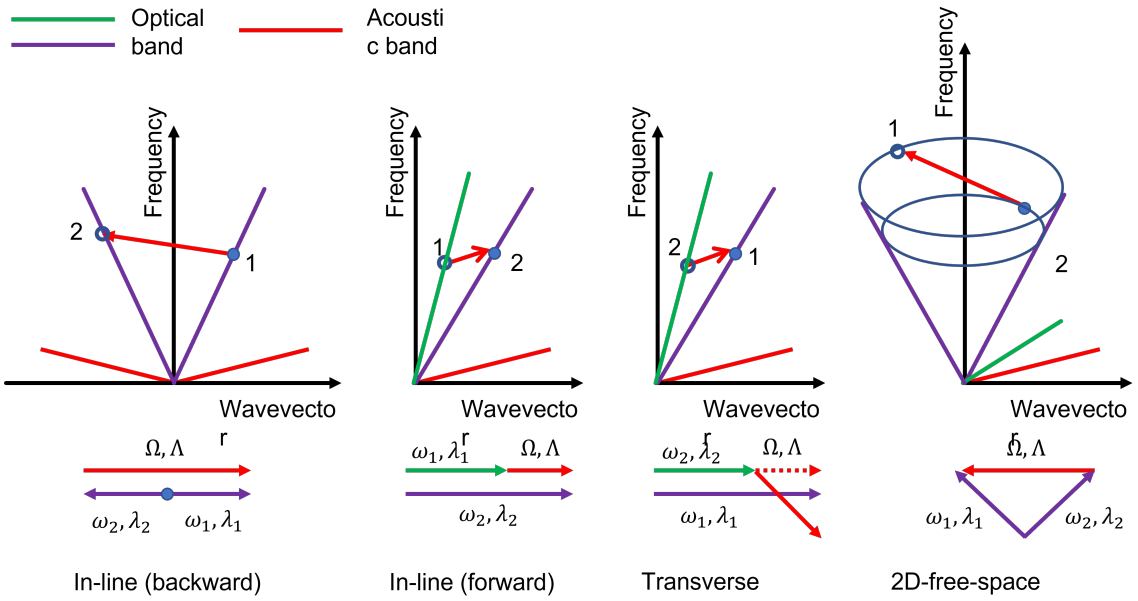

Figure 1.1: **Phase-matching conditions representative configurations.** a. in-line backward intraband BS. b. in-line forward interband BS. c. Transverse forward interband BS. d. 2D-free-space any-direction intraband.

materials with strong piezoelectric properties such as lithium niobate ($LiNbO_3$), zinc oxide (ZnO), and III-V materials, especially aluminum nitride (AlN).

1.2.1 Common Piezoelectric Materials

lithium niobate

Lithium niobate ($LiNbO_3$) [46] has been on of the most popular waveguiding acousto-optic material since the early 1970s. Below the Curie temperature of about 1210 °C, $LiNbO_3$ is a ferroelectric material with a triangular crystal structure and has large piezoelectric, electro-optic, photoelastic coefficients, and acousto-optic figures of merit. $LiNbO_3$ is a uniaxial crystal with a wide transparency window from 0.4 to 5 μm. Its ordinary and extraordinary refractive indices in the telecommunications C-band are $n_o = 2.21$ and $n_e = 2.14$, respectively. Its rich optical and acoustic properties make lithium niobate one of the most widely used materials in applications such as integrated dielectric waveguides, acoustic wave transducers, acoustic delay lines, acoustic filters, acousto-optic Q switches, light deflector and more.

Traditional $LiNbO_3$ guided-wave acousto-optic devices [47] are based on bulk crystal substrates, where surface acoustic waves (SAW) and diffusion-based optical waveguides are often used to achieve acousto-optic interactions. In the 2010s, lithium niobate on insulator (LNOI), fabricated with Smart-Cut technology, is the rising-star as a promising material platform for the AO devices. With the rapid commercialization of LNOI wafers and a major breakthrough in argon-based inductively coupled plasma reactive ion etching (ICP-RIE) technology for LNOI in the past decade, the next-generation integrated BS devices [48, 49] has been widely explored. Such BS devices feature strong co-confinement of acoustic and optical modes in high-quality LNOI acousto-optic waveguides with wavelength-scale cross-sections, enabling an unprecedentedly compact footprint and significantly enhanced scattering efficiency.

Zinc oxide

Zinc oxide (ZnO) [47] has been extensively studied as a waveguiding acousto-optic material platform since the 1970s. ZnO is a direct wide band gap (3.37 eV) semiconductor of the II-VI semiconductor group. It has the transparent window from 0.4 to 2 μm with ordinary and extraordinary refractive indices $n_o = 1.93$ and $n_e = 1.94$, respectively. Zinc oxide crystallizes in main in forms of hexagonal wurtzite and cubic zincblende, which have no inversion symmetry and resulting in the strong piezoelectricity. Its elastic softness also enable it as a promising acoustic waveguided material, thus make it an ideal material platform in the AO applications.

Group III-V materials

Group III-V materials semiconductors find wide applications in high-performance optoelectronic devices from classical to quantum regime owing to their superior optical and electronic properties including high electron mobility, direct band gap, and low exciton binding energy. Inspired by the prospect of manipulationg all the three "x-ons" (photons, phonons, and electrons) on the same platform, a growing research effort uses III-V materials to generate, guide, and interact with sound waves. Commonly used III-V materials for electromechanical excitation and manipulate acoustic modes include aluminum nitride (AlN) [38, 50], gallium arsenide (GaAs), and/or aluminum gallium arsenide (AlGaAs or AlxGa1-xN) [33, 51, 52], gallium nitride (GaN) [53] and gallium phosphide (GaP) [54].

AlN [55] is the most representative and widely used III-V material for AO devices. It is a wide bandgap (6.2 eV) semiconductor material with a wurtzite crystal structure. Using the magnetron sputtering deposition technique, c-axis oriented polycrystalline AlN films can be sputtered onto various substrates, including Si and SiO2, and retain piezoelectricity. The sputtered AlN films can be further patterned with CMOS compatible fabrication processes. Thanks to its excellent piezoelectric and acoustic properties, fabrication compatibility with CMOS processes, and wafer availability, AlN is widely used in high frequency

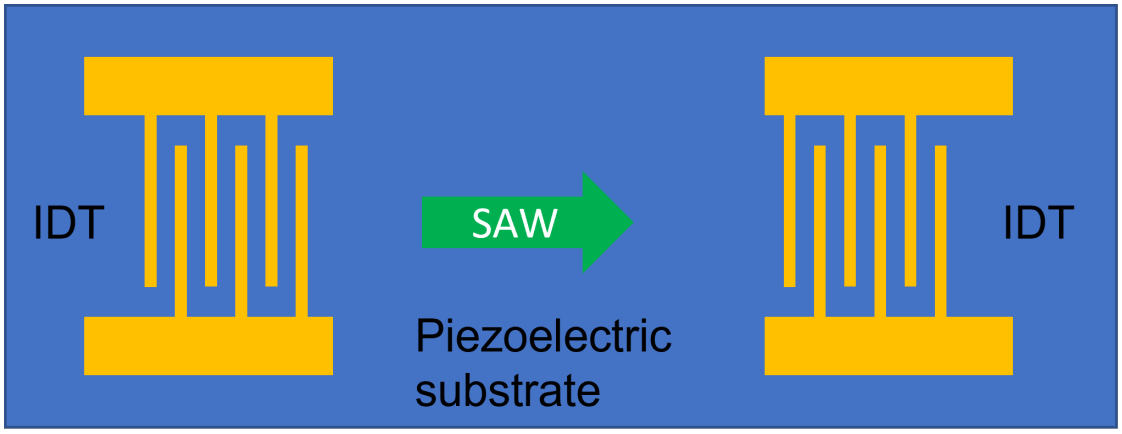

Figure 1.2: **Illustration of interdigital transducers.**

RF filters based on film bulk acoustic resonators (FBARs) [56] with superior performance that outperforms its electronic counterpart and is widely deployed in latest cellular phones and networks.

Furthermore, AlN thin films have been extensively studied as a material platform for AO devices in the past decade [34] because of their excellent optical and acoustic properties. It has a wide transparency window from 0.2 to 13.6 μm. with the ordinary and extraordinary refractive indices are n_o= 2.12 and n_e= 2.16 at telecom C-band, respectively, thus make it an ideal material platform in the AO applications.

1.2.2 Interdigital transducers

Generally, the efficiency of BS scattering is proportional to the total power flow of the incident acoustic wave beam. The efficiency and frequency response of AO devices, therefore, are a strong function of the characteristics of the transducer used to excite the incident acoustic beam. As aforementioned, the interdigital transducer, illustrated in Fig. 1.2, could be utilized as the acoustic excitation source in AO devices.

Interdigital transducers are the most direct and efficient way to excite surface acoustic waves (SAW) on piezoelectric substrates. IDTs can be conveniently patterned in thin metal films deposited on substrates due to its planar format. Then, sending an RF signal to the counter electrode in the IDT will excite mechanical vibrations through the piezoelectricity of the material. Basically, IDTs generate sound waves through the spatial-temporal periodic modulation created by the IDT geometry and the alternating electric potential applied to it. On the unsuspended bulk substrate, the excited acoustic wave is usually in the Rayleigh mode. The propagation polarization of such mode is a mixture of longitudinal and transverse modes. On the other hand, on the free-standing thin film, the excited acoustic wave could be either in the Lamb mode, whose polarization is mainly out-of-plane, or Love mode, whose polarization is mainly in-plane. The wavelength λ of the sound wave and the frequency Ω are determined by the period (Λ) of the IDT. It is important to note that, the acoustic wave is generated inside the IDT region, only the frequency is the invariant of the whole system. Therefore, due to the dispersion differences among different regions, the acoustic wavelength and thus wave vector varies. In the IDT region, due to the load mass and the softness of the metal thin film, the acoustic wave speed is normally lower than the open region, resulting in a longer acoustic wavelength and smaller wavevector. Therefore, when considering the phase-matching condition for the Brillouin scattering process, it is important to know the rate of change in different regions of the device, i.e. the dispersion relation.

The most common IDT has a uniform periodicity, so it is symmetric and bidirectional, emitting sound waves in both directions, which is undesirable in most cases. Unidirectional IDTs can be realized with more advanced designs [28, 57]. Moreover, it is possible to fabricate multiple transducer arrays [10] which greatly extend the bandwidth of acousto-optic interaction by optimizing the spatial phase match of the acoustic and optic beams over a wide range of frequency. Various types (or modes) of sound waves can be generated using various types of electromechanical transducers on bulk or thin films of piezoelectric material. These acoustic transducers have important applications in RF/MW signal processing as filters and delay lines. The reader is referred to a number of monographs on acoustic devices for RF/MW signal processing [27, 28, 58, 59].

The IDT is a natural candidate to meet the low power and compactness requirements of an integrated AO device. Over the past decade, fundamental research into phonons and their interactions with light, electrons, or other quantum degrees of freedom has sparked intense interest in developing new designs that perform in the 100s MHz to GHz frequency range. Such a frequency range is consistent with the optical linewidth of nanocavities in the telecommunications field, leading to significant cavity optomechanical dynamics research. Furthermore, acoustic waves in this frequency range have comparable wavelengths (and thus wave vectors) to their optical counterparts in the telecommunications domain, satisfying the phase-matching condition for Brillouin scattering.

1.3 Applications

1.3.1 Next-generation acousto-optics

The integrated AO device is ready to completely transform from the traditional guided-wave acousto-optic (AO) with an extraordinary compact footprint, enhanced scattering efficiency and high acoustic frequency. Many applications demonstrated in traditional AO devices [47] are still relevant to next-generation AO, including AO modulators, AO filters, freuqency shifters, signal processors and beam steering.

Here is a simplified demonstration of the scaling effect of an AO device. If the acoustic power density is held constant, so is the change in refractive index it induces, then the total acoustic power consumption to achieve the same function is proportional to the cross-sectional area of the AO interacting acoustic wave. From the conventional bulk guided wave acousto-optic devces to the integrated AO devcies, the cross-sectional area of the acoustic wave could be reduced from millimeters square to microns square, resulting in three or even four orders of reduction of the power consumption, from few watts level, down to the milliwatts or even smaller level.

In addition to significantly reducing acoustic power consumption, the performance indicators of the most representative AO equipment will also be greatly improved. For beam steers, the steering angle is expected to increase from just a few degrees to potentially 180°, which means any angle is feasible. For optical tuning filters, the operating wavelength can be extended to the telecom band or even mid-infrared, and the entire device can be monolithically integrated with other peripheral devices on an LNOI chip to realize a complete signal processing system, or a fully CMOS compatible AlN on SOI chip. For frequency shifters and single sideband modulators, operating frequencies are expected to increase from 100s MHz up to 10s GHz. For example, a state-of-art 16 GHz AO modulator has been demonstrated in a suspended thin-film AlN strip waveguide [38], which naturally enables single-sideband modulation, which could be used for the optical communication applications. Moreover, an interband BS device has been demonstrated in suspended thin-film LiNbO3 strip waveguides [48], with the highest EBS efficiency of 18% to date, with only an acoustic power of 30 μW. Other works including acousto-optic Mach-Zehnder modulators [33,49,60], arrayed waveguide gratings (AWGs) [32], racetrack resonators [61], photonic crystal nanocavities [62, 63] and an optomechanical adiabatic frequency shifter [64] etc has also been demonstrated to show the advantages of integrated AO devices over the conventional bulky one. However, a key prerequisite for the aforementioned performance improvements is that the acoustic losses remain sufficiently low, especially at frequencies of GHz and above. Such a premise may not be valid at room temperature due to the large number of thermal phonons interacting with the sound waves of interest. Nonetheless, at low temperatures, acoustic losses have been experimentally shown to be low enough to support propagation lengths on the meter scale and beyond [65], promising for quantum applications.

1.3.2 Non-reciprocal devices and circuits

The BS process induced by propagating acoustic modes is inherently non-reciprocal unless the acoustic wave vector is perpendicular to the light wave vector. In such a process, the time-reversal symmetry of light propagation is broken, since the acoustic modes of propaga-

tion are not correspondingly reversed when time is reversed. Therefore, such nonreciprocity of the integrated AO devices can be exploited as the optical isolator or the circulator with potentially sub-milliwatt acoustic power consumption. More interestingly, since acoustic modes can be excited and manipulated with phonon circuits, it is possible to realize reconfigurable nonreciprocal devices and circuits, which cannot be conveniently achieved using magneto-optical thin-film devices. Such applications has already demonstrated by many groups, with either integrated AO waveguide [38], or resonated AO device [66].

1.3.3 Quantum transduction

The ideal platform for realizing RF-to-optical conversion and vice versa is to combine optomechanics with photonic and electromechanical control.The interface between the RF superconducting quantum computer and optical quantum communication network is expected as the next-generation distribution cloud computer. Therefore, the efficient interconnect link between RF qubit and optical qubit is expected. However, there is a huge gap between the optical frequency (100s THz) and RF frequency (GHz) and a significantly mode mismatch between them, making the direct RF-to-optical conversion extreme difficult. Thanks to the nature of the acoustic wave, despite the huge frequency gap, the slow sound speed, enabling the phase matching as aforementioned, and thus the strong AO interaction. Moreover, with the high electromechanical coupling efficiency, the efficient RF-acousitc-optical conversion link could be achieved. Therefore, a new approach combining photonic and phononic circuits on the same platform is proposed. For example, realizing on-chip quantum coherent interconnection between superconducting quantum processors remains an important challenge to scale computing systems while limiting the power consumption of cryogenic systems. In this context, optomechanical systems can be an ideal candidate for performing microwave-to-optical conversion of quantum states [31, 67, 68]. This hybrid integration platform combining an optomechanical cavity with electromechanical actuation has been proposed [54] and fabricated using gallium phosphide (GaP) bonded to a silicon chip.

Chapter 2

FREQUENCY-ANGULAR RESOLVING LIDAR USING CHIP-SCALE ACOUSTO-OPTIC BEAM STEERING

2.1 Introduction

Non-mechanical, solid-state optical beam steering is critical to the next-generation light detection and ranging (LiDAR) technology that is indispensable for 3D imaging in automation, navigation, and robotics [69–71]. Various beam steering technologies [72] have been developed, including optical phased array [73–76], spatial light modulation [77–79], focal plane switch array [80, 81], dispersive frequency comb [82, 83], and spectro-temporal modulation [84]. Here, we report a new beam steering technique and the LiDAR system it enables, based on acousto-optic beam steering (AOBS) integrated on a chip where gigahertz frequency acoustic waves are generated to scatter light from a planar waveguide into free space. The physics of the Brillouin scattering of light by sound waves [1, 11] not only enables the control of light scattering angle by the acoustic frequency—therefore beam steering using only a single transducer, but also "labels" beams steered at different angles with unique frequency shifts. The latter allows using a single receiver to resolve the reflecting object's angular position from the frequency of the light it reflects and thus enables a new LiDAR imaging scheme, which we name frequency-angular resolving (FAR) LiDAR. Thanks to the gigahertz acoustic frequency, FAR LiDAR has enough bandwidth to afford frequency-modulated continuous-wave (FMCW) ranging simultaneously and thus 3D imaging. A single AOBS device achieves an 18° angular field of view (FOV) and 0.12° diffraction-limited angular resolution for near-infrared light. The FAR LiDAR architecture requires only a single microwave drive without the need for sophisticated control electronics, affords broadband operation, and uses simple fabrication processes for monolithic integration. The chip-scale AOBS device can be readily scaled up to an array, realizing FAR LiDAR imaging systems with a wide 2D FOV in a miniature, low-cost form factor for widespread

applications.

LiDAR affords superior 3D imaging resolution and range, therefore is considered an indispensable optical perception technology for intelligent automation systems including autonomous vehicles and robotics [69–71]. At the heart of a scanning LiDAR is the optical beam steering system that scans the laser beams in space19. Non-mechanical beam steering systems are highly desirable to replace the current mechanical scanners for the advantages of compactness, robustness, speed, and cost4. Methods of non-mechanical optical beam steering are generally based on diffractive or dispersive principles [72]. Diffractive methods control the wavefront of the optical beam through a synthetic aperture which emits light with a tunable phase front toward a controlled direction. Such an artificial aperture can be created using an optical phase array (OPA) [73–76] or a spatial light modulator (SLM) [77–79]. An alternative technology is the focal plane switch array (FPSA) [80,81], in which an array of emitters is placed at the focal plane of a lens, and the beams from different emitters are refracted by the lens to different angles. To achieve a large steering angle and a high angular resolution, OPA, SLM, and FPSA universally require a large number of discrete elements [**?**,80,81], each individually controlled and having a size on the order of the optical wavelength. The need for sophisticated systems to control a large array of elements and the complex fabrication processes needed are outstanding challenges faced by these technologies.

On the other hand, dispersive optical elements, such as prisms and gratings, can diffract light of different wavelengths in different directions. Therefore, beam steering can be achieved through chromatic dispersion by changing the input optical frequency using, a tunable laser, a broadband source, or a frequency comb as the light source [82–84]. These sources themselves, however, are sophisticated and expensive. If the dispersive property of the optical element can be tuned, rather than tuning the optical wavelength, in principle beam steering can also be realized. The dispersion of an optical element depends on its material's property (e.g., for a prism) and its structure (e.g., for a grating). It is, however, impractical to tune those parameters over a wide enough range to achieve realistic beam steering.

Interestingly, nature provides a means to generate a dynamically tunable index grating—acoustic waves propagating in a material mechanically undulate its refractive index and thus produce a moving index grating [1]. For a given material, the spatial period of this grating is determined by the acoustic wavelength in the material, and the phase contrast is controlled by the acoustic intensity. These dispersive properties can be conveniently tuned by controlling the acoustic wave frequency and power. This moving grating can scatter light through Brillouin scattering, which is an inelastic scattering process of light by the acoustic waves [1, 11]. Given the acoustic frequency (Ω) and phase velocity (v), momentum conservation (or equivalently, phase-matching condition) determines the angle of light scattering, while energy conservation dictates that the frequency of the scattered light is shifted by the amount of the acoustic frequency. These principles have been utilized in various types of acousto-optic devices, such as acousto-optic deflectors, switches, frequency shifters, and filters [85]. Conventional acousto-optic devices use bulk crystals and MHz frequency acoustic waves to realize a large optical aperture and achieve a high angular resolution [86], but deflect light only by a small angle. A paradigm shift is the advancement of guided-wave acousto-optic devices, which confine both optical and acoustic waves in planar waveguiding structures, leading to significantly enhanced light-sound interaction and consequently acousto-optic performance and efficiency [17, 37, 38, 47, 61]. In those devices, the scattering of light mainly remains in the plane of the 2D waveguide.

2.2 Frequency-angular resolving LiDAR schematics

If the acoustic frequency is sufficiently high, the acoustic wavenumber $K = \Omega/v$ will be large enough such that it can scatter the counter-propagating optical waveguide mode into the light cone, thereby steering a beam into free space [41, 87]. Fig. 2.1a schematically illustrates this effect, which is the base of the acousto-optic beam steering (AOBS) we report here. The dispersion diagram in Fig. 2.1b depicts the phase-matching condition of AOBS: $k_0 cos(\theta) = k_g - K$, where k_g is the guided optical mode wavenumber, $k_0 = \omega_0/c$ is free space optical wavenumber, and θ is the scattering angle measured from the surface of the waveguide. At the same time, the scattered light frequency is shifted up from ω_0 to the anti-Stokes sideband at $\omega_0 + \Omega$. Therefore, we can find a frequency-angular relation $(\Omega - \theta)$

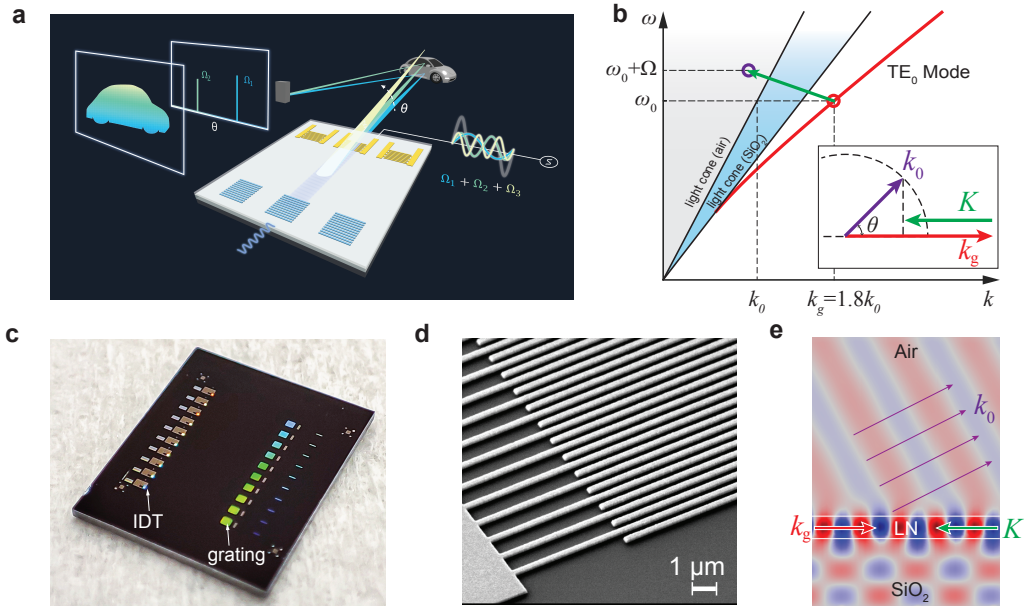

Figure 2.1: **Principle of FAR LiDAR based on acousto-optic beam steering and chip-scale devices.** a. Schematic illustration of the FAR LiDAR scheme based on AOBS. b. Dispersion diagram of the acousto-optic Brillouin scattering process. The dispersion curve of the TE0 mode of the LN planar waveguide is simulated and plotted as the orange curve. At frequency ω_0 (wavelength 1.55 μm), the mode wavenumber is $1.8k_0$ (red circle). The counter-propagating acoustic wave (green arrow) scatters the light into the light cone of air (purple circle in the grey-shaded area). For clarity, the frequency axis is not to the scale. Inset: momentum vector relation of the Brillion scattering. The light is scattered into space at an angle θ from the surface. c. Photograph of an LNOI chip with ten AOBS devices. d. Scanning microscope image of the IDT. The period is chirped from 1.45 μm to 1.75 μm. e. Finite-element simulation of the AOBS process, showing light is scattered into space at 30° from the surface.

for AOBS:

$$cos(\theta) = \frac{k_g - K}{k_0} = n_e - \left(\frac{c}{\omega_0 v}\right)\Omega \tag{2.1}$$

where $n_e = k_g/k_0$ is the effective mode index of the waveguide mode. The simple relation 2.1 has two implications. First, the light scattering angle θ is controlled by the acoustic frequency Ω such that beam steering out of the substrate (i.e., $cos(\theta) < 1$) can be achieved with $\Omega/2\pi$ in the GHz range for typical planar waveguides (e.g., with $n_e > 1.5$) and near-infrared light. Second, since the frequency of the scattered light is shifted up to $\omega_0 + \Omega$, by measuring the frequency of the reflected light from an object, one can use equation 2.1 to resolve the object's angular position θ. Thereby, an image of the object can be reconstructed from frequency domain measurement when the steered light beam is scanned in the scene by AOBS. Combining these two essential principles, we propose the frequency-angular resolving (FAR) LiDAR, as illustrated in Fig. 2.1a, which consists of a transmitter using AOBS as the beam scanner and a coherent receiver to measure the frequency of the reflected light. FAR LiDAR has several important advantages. First, since the angular position of the object is "labeled" by the frequency of the reflected light, the receiver can determine the object's position without *a priori* knowledge of the outgoing beam angle. This novel scheme thus allows the transmitter and the receiver to be separated and use different optical apertures in a bistatic configuration and operated asynchronously, affording much flexibility in designing the receiver to improve signal-to-noise ratio and detection speed. Second, AOBS uses a single microwave drive to excite the acoustic wave, whose frequency determines the steering angle. Random access is achieved by changing the drive frequency arbitrarily within the system bandwidth. Third, AOBS uses coherent acoustic waves so that multiple tones of different frequencies can copropagating in the device to scatter light into multiple directions simultaneously. Therefore, parallel scanning and detection of multiple beams can be achieved. Finally, since the acoustic frequency used in the FAR LiDAR is in the GHz range, the system affords sufficient bandwidth to perform FMCW for coherent ranging. Combining FAR and FMCW, full 3D imaging will be achieved. In this paper, we demonstrate all of the above-mentioned capabilities with a prototype FAR LiDAR system based on chip-scale AOBS devices.

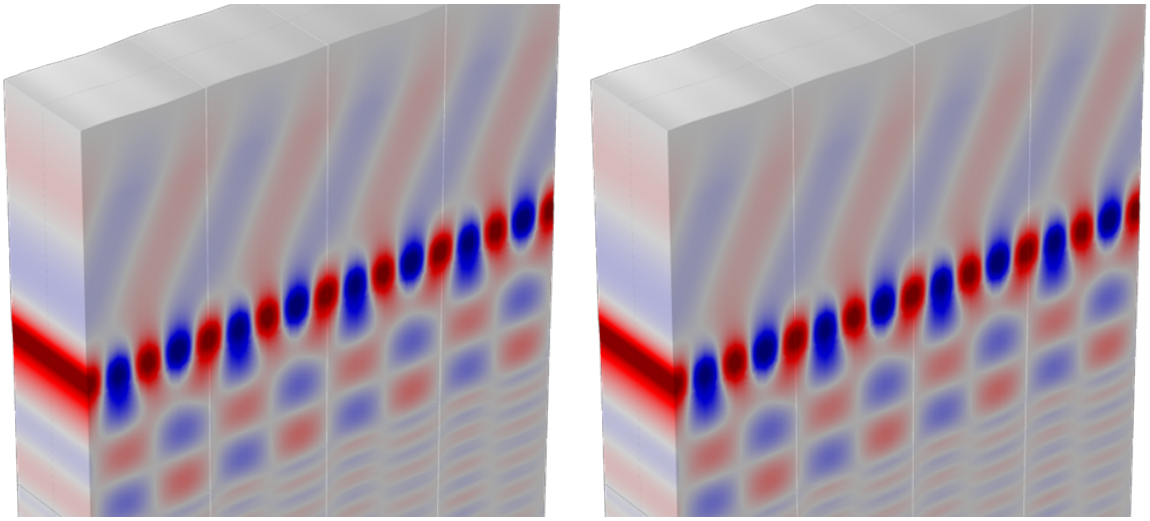

Figure 2.2: **3D (left) and 2D (right) simulation of the SAW-perturbed eigenmode by COMSOL.**

2.3 Acousto-optic beam steering device

2.3.1 Simulation and optimization

We simulate the AOBS scattering and optimize the device design using the finite element method (FEM) software, COMSOL Multiphysics [44]. The simulated unit cell model is shown in Fig. 3.2. As discussed in S1, due to the acoustic wave induced periodic perturbation to the permittivity of the waveguide, the guided optical mode is scattered to the radiative modes, and the new eigenmode of the perturbed waveguide becomes a weakly-guided mode with the scattering rate α, with P_g being the guide optical power and $\partial P_{\mathrm{g}}/\partial z = -\alpha P_{\mathrm{g}}$. The output optical power of the simulation domain is, $P_{\mathrm{out}} = P_{\mathrm{in}} = P_{\mathrm{g}} + P_{\mathrm{su}} + P_{\mathrm{sl}}$, where Pin is the injected optical power, P_{su} and P_{sl} are the upward and downward radiative mode power, respectively. From energy conservation, $\frac{\partial P_g}{\partial z} + \frac{\partial (P_{su}+P_{sl})}{\partial z} = 0$, we can have $\frac{\partial (P_{su}+P_{sl})}{\partial z} = -\frac{\partial P_g}{\partial z} = \alpha P_{in}$. By setting the upper and lower boundary of the simulation domain as the perfect-matched-layer, the vertically outgoing optical power could be con-

sidered as the radiative loss. Therefore, similar to the previous perturbation theory, the eigenfrequency becomes complex, where $\omega \to \omega - i\kappa$ and the scattering rate is $\alpha = 2\kappa/v_{\mathrm{g}}$. We performed both 2D and 3D simulations to optimize the LN thin film thickness and the buried oxide (BOX) thickness to maximize the upward scattering rate. In the 2D simulation, we only considered the moving boundary effect, which is modeled as the sinusoidal deformation at the waveguide boundary. In the 3D simulation, we considered both the photoelastic effect and the moving boundary effect. In both simulations, we assume that the orientation of LN is x-cut and the acoustic wave propagates along the y-axis to have a high Rayleigh mode excitation efficiency.

The full simulation includes three steps: First, the group velocity of the optical slab mode of the LNOI substrate (or LN only) is simulated. Then the acoustic mode, which is the Rayleigh-like acoustic mode, is simulated to calculate the displacement field. The acoustic wavelength was selected to meet the phase matching conditions. Finally, the acoustic wave induced permittivity changing is introduced to solve for the new eigenmodes.

Besides the moving boundary effect and the direct photoelastic effect, we also included the roto-optic effect and the indirect elasto-optic effect in our simulation since lithium niobate is both birefringent and piezoelectric. The latter two effects introduce an extra permittivity perturbation due to the additional elasto-optic component. For the roto effect, the permittivity changing is, $\Delta\left(\varepsilon_{ij}\right)' = p_{ijkl}R_{kl}$, where $R_{kl} = \frac{S_{kl}-S_{lk}}{2}$. The indirect elasto-optic effect occurs as the result of the piezoelectric effect and electro-optic effect in tandem, and the effective elasto-optic tensor for such effect is given by, $p^*_{ij} = p_{ij} - \frac{r_{im}\Lambda_m e_{jn} S \Lambda_n}{\varepsilon_{mn}\Lambda_m\Lambda_n}$, where p_{ij} is the direct elasto-optic tensor, r_{im} is the electro-optic tensor, e_{jn} is the piezoelectric tensor , and Λ_m is the unit acoustic wave vector. The material parameters are taken from [45]. To start the optimization, we defined the effective acousto-optic (AO) scattering length as $L = 1/\alpha$. Neglecting acoustic wave decaying, the solution of the optical power gives,

$$(P_{su} + P_{sl}) = P_0 - P_g = P_0\left(1 - \exp\left(-\frac{Z}{L}\right)\right) \tag{2.2}$$

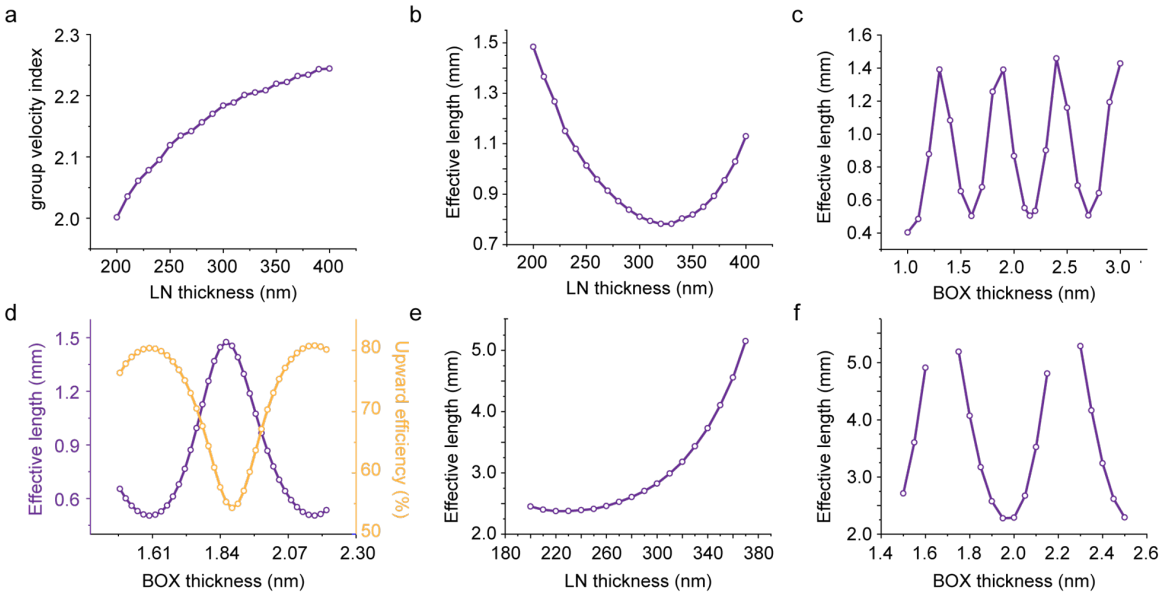

Figure 2.3: **Simulation and optimization results.**a, The group velocity of the LNOI TE0 slab mode with different thicknesses of the LN layer. b, 2D optimization of the thickness of LN thin film. c, d, 2D optimization of the thickness of the BOX layer. e, 3D optimization of the thickness of LN. f, 3D optimization of the thickness of the BOX layer.

. The upward scattering efficiency is then defined as $\rho = P_{\text{sul}} / (P_{\text{sul}} + P_{\text{si}})$.

We first optimized the thickness of the LN thin film of a free-standing LN waveguide. Afterward, we search for the optimal thickness of the BOX layer of the LNOI when the back reflection from the BOX/silicon interface can enhance the upward scattering.

Fig. 3.3a shows the optical group index of the TE0 slab mode as a function of the LN layer thickness. When optimizing the LN thickness, a boundary deformation amplitude of 5 nm is assumed. Fig. 3.3b shows that the simulated effective AO scattering length L dependence on the LN thickness reaches a minimum at 330 nm, corresponding to the highest scattering efficiency. Fig. 3.3c and d show that L and η have a periodic dependence on the BOX thickness, as expected from the interference effect.

Fig. 3.3e and f show the 3D optimization results in which L as a function of the LN layer and the BOX layer thickness are plotted. An acoustic power of 10 mW/μm is assumed. The minimal L is reached at the LN thickness of 220 nm, which differs from the 2D results. Nevertheless, the difference of L between 220 and 330 nm is quite small. For practical considerations of a better LN thin film quality and stronger piezoelectricity, we chose LNOI substrates with 300 nm thick LN with a moderate compromise of the scattering efficiency as predicted by the simulation. With 300 nm LN thickness, Fig. 3.3f shows a periodic dependence of L to the BOX thickness. Based on that, we chose the 2 µm thick BOX such that the corresponding upward scattering efficiency reaches 80%, and the effective scattering length L is as short as 2.2 mm.

2.3.2 Structure of AOBS devices

We build AOBS devices using the lithium niobate on insulator (LNOI) platform (330 nm thick LN layer and 2 μm buried oxide). Fig. 2.1c shows an image of an array of ten AOBS devices fabricated on an LNOI chip. Each AOBS device has a very simple construction consisting of only two components. On one end, an interdigital transducer (IDT) made of 180 nm aluminum film, as shown in Fig. 2.1d, is patterned and used to electromechanically excite acoustic waves utilizing LN's strong piezoelectricity. On the other end, an optical grating coupler is patterned in hydrogen silsesquioxane (HSQ) electron beam resist. The grating couples light from a laser to the transverse-electric field (TE) mode of the planar waveguide formed by the LN layer. The space between the IDT and the grating coupler, which is w=100 μm wide and l=2 mm long, is the AOBS' nominal beam steering aperture. The acoustic waves are generated by the IDT and propagate to fill this aperture, scattering the counter-propagating light coupled in from the grating coupler. The dispersion relation of the TE mode (Fig. 2.1e) at 1.55 μm optical wavelength is simulated and plotted in Fig. 2.1b, from which we can calculate the required acoustic wavenumber from equation 2.1. At a given frequency, the acoustic wavelength (Λ) and wavenumber (K) are determined by the

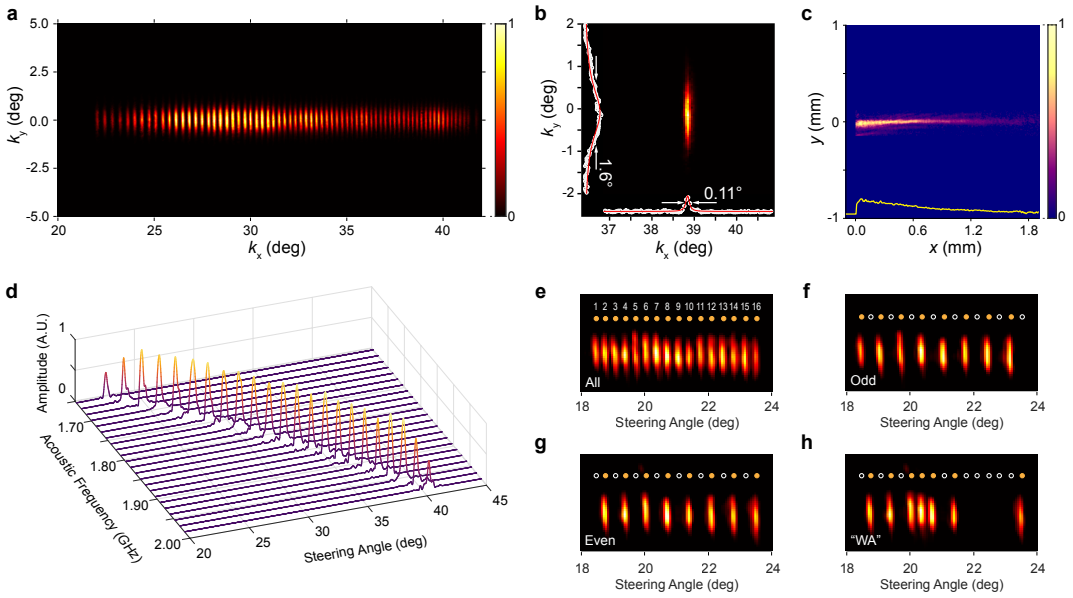
a
b
c
d
e
f
g
h
k_y (deg)
k_x (deg)
1.6°
0.11°
y (mm)
x (mm)
Amplitude (A.U.)
Acoustic Frequency (GHz)
Steering Angle (deg)
1 2 3 4 5 6 7 8 9 10 11 12 13 14 15 16
All
Odd
Even
"WA"

Figure 2.4: **Characterization of AOBS and multi-beam generation.** a. Superimposed image of the focal plane when the beam is scanned across a FOV from 22° to 40°, showing 66 well-resolved spots. b. Magnified image of one spot at 38.8°. The beam angular divergence along k_x is 0.11° (bottom inset) and along k_y is 1.6° (left inset), due to the rectangular AOBS aperture. c. Real-space image of light scattering from the AOBS aperture. The light intensity decays exponentially from the front of the IDT (x=0), due to the propagation loss of the acoustic wave. Fitting the integrated intensity along the x-axis (bottom inset, yellow line) gives an acoustic propagation length of 0.6±0.1 mm. d. The measured frequency-angle relation when the beam is steered by sweeping the acoustic frequency. e-f. Dynamic multi-beam generation and arbitrary programming of 16 beams (e) at odd (f) and even (g) sites, and in a sequence of the ASCII code of characters "WA" (h).

period of the IDT and the phase velocity (v) of the acoustic mode that is excited. Of interest for the AOBS purpose is the Rayleigh type mode (Fig. 2.5) which is confined in the LN layer and thus efficiently interacts with the TE mode. To achieve a large range of steering angles, that is, a large angular FOV, the AOBS device needs to have a widely tunable acoustic frequency. To this end, we use a broadband IDT design with chirped periods to achieve Δf=350 MHz bandwidth at a central frequency of 1.8 GHz. Our simulation results in Fig. 2.1e show that the TE mode is scattered from the chip surface into free space at an angle (θ) of 30° with a theoretical FOV of 20°. Another important metric for acousto-optic devices is the number of resolvable spots (equivalently, the time-bandwidth product) [86]22, which is given by $N = \Delta f \cdot \tau$, $\tau = l/v$ is the acoustic transit time across the aperture of length l, where v=3,100 m/s is the phase velocity of the Rayleigh mode. Therefore, a theoretical value of N=226, comparable to bulk acousto-optic devices, despite a much smaller aperture because of a much larger absolute bandwidth.

2.3.3 IDT characterization

The reflection coefficient (S_11) of the IDT was measured with a vector network analyzer (VNA). From the S_11 spectra, we characterized the electromechanical coupling of the IDT using the modified Butterworth-Van Dyke (mBVD) model, from which the electromechanical conversion efficiency can be calculated. Fig. 3.5a shows the measured S_11 spectra and the electromechanical conversion efficiency of the Rayleigh mode. Fig. 3.5b shows the equivalent circuit model with parameters extracted from the experimental data. The series resistor R_s accounts for the total series resistance between the RF probe and the IDT fingers. The admittance of IDT fingers can be written as,

$$Y(f) = R_l + j\omega C_e + G_a(f) + j\omega B_a(f) \tag{2.3}$$

, where the shunt resistor R_l and the capacitor C_e accounts for the effective leakage resistance and electrode capacitance between the IDT fingers, respectively. The complex, frequency-dependent admittance $Y_a(f) = G_a(f) + j\omega B_a(f)$, represents the electromechanical response of the IDT, where the dissipated power is transduced into the acoustic wave.

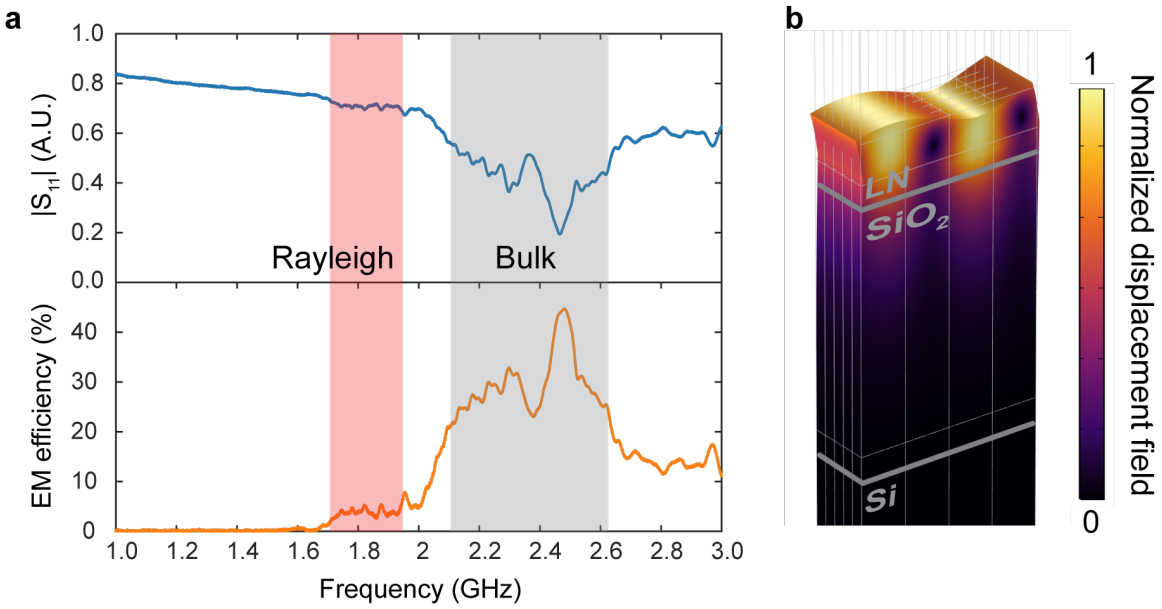

Figure 2.5: **Acoustic mode characteristics.** a. The RF reflection coefficient S11 and the electromechanical conversion efficiency of the chirped IDT based on the modified Butterworh-Van Dyke (mBVD) model. The red shaded area marks the Rayleigh mode acoustic wave that is responsible for acousto-optic beam steering in our device and has an electromechanical conversion efficiency of 5.1% within a bandwidth of 200 MHz. The grey shaded area marks the bands of multiple bulk modes that are inefficient in acousto-optic beam steering because they are largely confined in the SiO2 layer, although more efficiently excited. b. Simulation of the Rayleigh mode acoustic wave, showing the mode is confined in the LN layer.

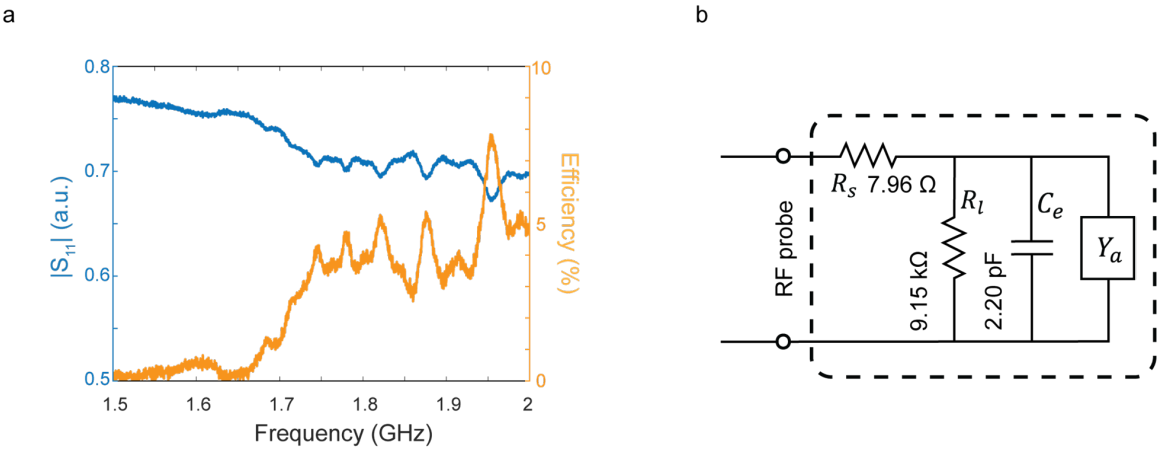

Figure 2.6: **IDT characteristic.** a, The RF reflection coefficient and the electromechanical conversion efficiency of the Rayleigh mode generated by the chirped-IDT and b, the equivalent circuit model.

From the measured S11, the load impedance $Z_L(f)$ can be calculated from the equation $Z_L = R_0 \times (1 + S_{11}) / (1 - S_{11})$, where the characteristic resistance $R_0 = 50\Omega$. Assuming the R_s, R_l and Ce are constant over the IDT bandwidth, the three parameters can be estimated by fitting the Z_L around the frequency of interest with Y_a open-circuited. $Y_a(f)$ is thus obtained. Then the power distribution on each component can be calculated according to the equivalent circuit model. The electromechanical conversion efficiency can be calculated by the power dissipated on Y_a over the total input power,

$$\eta_{EM} = P_{Ya}/P_{in} \tag{2.4}$$

.

2.3.4 Characteristic of AOBS devices

The beam steering results of the AOBS device are shown in Fig. 2.4. A fiber-coupled, near-IR diode laser is used as the light source. A CCD camera is placed at the focal plane of a lens to image the steered beam in the momentum-space (k-space) (Fig. 2.7). Fig. 2.4a shows the superimposed images captured by the camera, showing 66 spots when the beam

is scanned in angles of 22° to 40° (18° FOV) by sweeping the frequency of the microwave source that drives the IDT. The variation in the intensity among the spots is attributed to the uneven electromechanical conversion efficiency within the bandwidth of the IDT (Fig. 2.5). Fig. 2.4b shows the detailed profile of one spot, which has an angular divergence of 0.11° (full-width half-maximum (FWHM)) along the k_x-axis and 1.6° along the k_y-axis. The elliptical spot shape is diffraction-limited by the rectangular acousto-optic aperture. The average kx-axis angular divergence of the beams across the FOV is 0.12° so the number of resolvable spots along is thus N=150, lower than the theoretical value. Fig. 2.4c shows the real-space image of light scattering from the AOBS aperture. The intensity of scattered light appears to decay from the front edge (x=0) of the IDT, where the acoustic wave intensity is the highest, toward the grating coupler. Since the optical propagation loss of the TE mode is expected to be low, fitting the results in Fig. 2.4c with a model (see Supplementary Info.) reveals that the acoustic wave suffers a high loss with a propagation length (1/e) of ∼0.6±0.1 mm, which reduces the effective AOBS aperture length from the nominal length. In comparison, acoustic waves of similar frequencies in bulk $LiNbO_3$ have a propagation length of centimeters [41, 88]. The relatively high acoustic loss can be attributed to the bonding interfaces of the LNOI wafer and the leakage to the substrate. By using a free-standing LN membrane or LN on sapphire substrates where the acoustic wave is confined in the LN layer [89, 90], the acoustic loss can be significantly reduced. The highest overall beam steering efficiency in Fig. 2.4a is determined to be 2.8% at 30°, based on fitting the results in Fig. 2.4c with a model, when 20 dBm microwave power is applied to drive the IDT. The limiting factors of the current device in efficiency include the broadband IDT's low electromechanical conversion efficiency of only 5.1% (Fig. **??**) and the small effective aperture size due to high acoustic loss. Our simulation (Fig. 2.1e and Supplementary Info) shows that if the effective aperture can be increased to 5 mm, the steering efficiency can be improved to 20% using a moderate microwave power of 20 dBm.

The AOBS frequency-angular relation $\theta(\Omega)$ described by Equation 2.1 is measured and plotted in Fig. 2.4d, which shows the beam steering angle as a function of a single-tone acoustic frequency. This measurement provides the calibration needed for using the AOBS

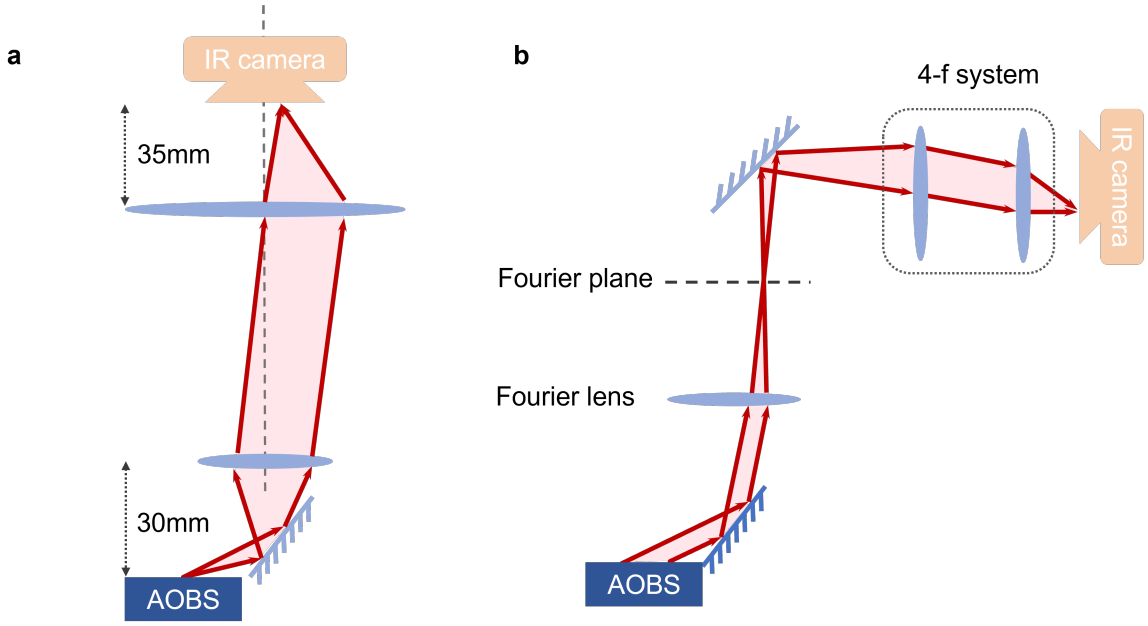

Figure 2.7: **Schematics of optical characterization setups.** a, 4f system directly imaging the real-space beam profile at the emission aperture. b, Setup for imaging the k-space beam profile.

in FAR LiDAR. In addition, the coherence of the AOBS process also allows multiple tones of acoustic waves to co-propagate in the aperture. Each tone scatters the light into a different angle and thus together they generate multiple beams simultaneously. Each beam is independently controlled in phase and amplitude by the corresponding RF drive. Such multi-beam steering capability is demonstrated in Fig. 2.4e-h. We drive the IDT with multi-tone waveforms that consist of 16 equally spaced frequency components to generate an array of 16 beams (Fig. 2.4e). The waveforms are synthesized by an arbitrary waveform generator (AWG). To demonstrate arbitrary programming of the beam array with random access, in Fig. 2.4f-h, respectively, we show beams generated at even and odd sites, and a sequence representing the ASCII code of "WA". It is worth noting that the multi-beam steering capability of acousto-optic deflectors plays an important role in neutral atom and trapped ion quantum computing for performing parallelized quantum gates [91]. The LNOI platform can support a broad optical spectral range, including those used in atom and ion quantum computing. In Supplementary Information, we include results of visible band AOBS with performance similar to the infrared. Therefore, we expect the integrated AOBS system we report will also have an impact on quantum technology.

2.4 Measurement results of FAR LiDAR

We then demonstrate LiDAR imaging using the FAR principle of AOBS. Fig. 2.8a shows the schematic of the FAR LiDAR system. In the transmitter, an AOBS device steers and scans the laser beam at an angle $\theta(\Omega)$ toward the object in the far field. If FMCW ranging is performed, an electro-optic phase modulator (EOM) is used to modulate the laser light to generate a chirped source. Without FMCW, the frequency of the steered beam is shifted by AOBS to the anti-Stoke sideband at $\omega_0 + \Omega$. To resolve this frequency shift, we use the coherent receiver scheme. The receiver taps 1% of the laser source as the local oscillator (LO). The reflected light from the object is collected with a lens and coupled into a 50/50 fiber coupler, where it combines with the LO. A balanced photodetector (BPD) is used to detect their beating signal at frequency Ω, which is digitized and analyzed. Fig. 2.8b shows the various beating signals measured at the receiver using a spectrum analyzer when the

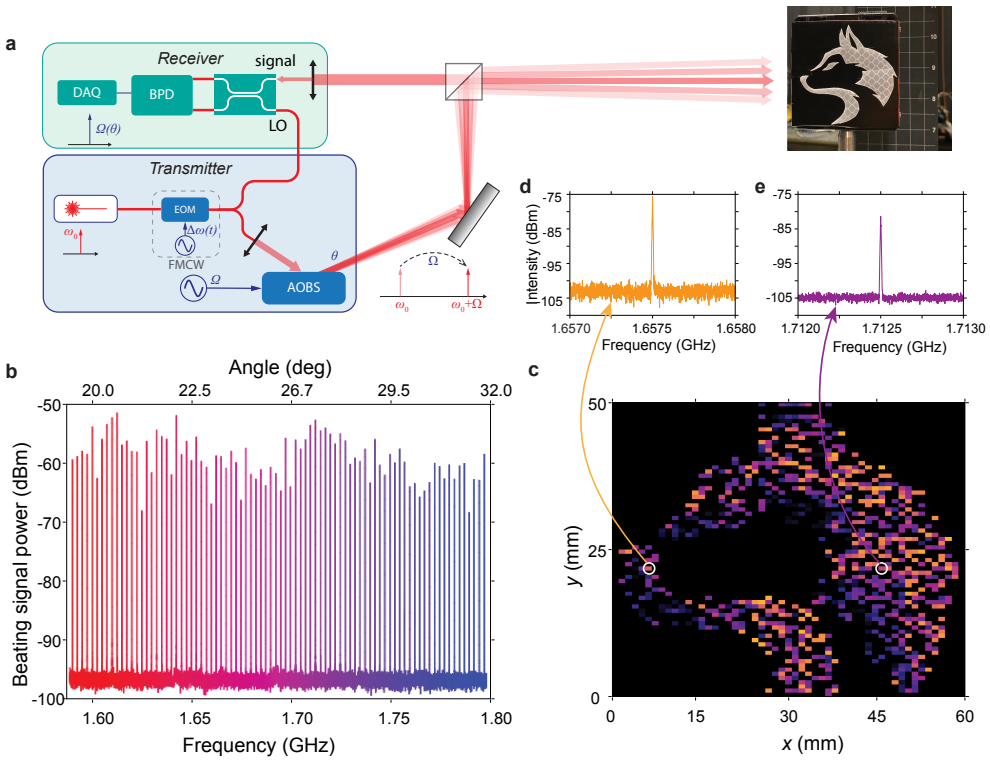
a
Receiver
signal
DAQ
BPD
LO
Transmitter
EOM
FMCW
AOBS
b
Angle (deg)
20.0
22.5
26.7
29.5
32.0
Beating signal power (dBm)
Frequency (GHz)
c
y (mm)
x (mm)
d
Intensity (dBm)
Frequency (GHz)
e
Frequency (GHz)

Figure 2.8: **FAR LiDAR Imaging.** a. Schematics of the FAR LiDAR system. The transmitter (Tx) includes a fixed-wavelength, fiber-coupled laser source, an EOM for FMCW, and an AOBS device driven by an RF source to steer the beam. An additional mirror is used to deflect the light toward the object. The coherent receiver (Rx) uses homodyne detection to resolve the frequency shift of the reflected light by beating it with the local oscillator (LO), which is tapped from the laser source. A balanced photodetector (BPD) is used to measure the beating signal, which is sampled and processed by a digital data acquisition (DAQ) system to perform spectrum analysis. As a demonstration, a 60 mm $\times$ 50 mm cutout of a husky dog image made of retroreflective film is used as the object. It is placed 1.8 meters from the LiDAR system. b. Spectral of the beating signal at the receiver when the AOBS scans beam across the FOV. Using the measured frequency-angular relation in Fig. 2.4d, the beating frequency can be transformed to angle of the object. c. FAR LiDAR image of the object. Each pixel's position and brightness are resolved from the signal's beating frequency and power, respectively. d and e. The raw beating signal of two representative pixels.

AOBS scans the beam across different angles. Based on Equation (1) and using the measured frequency-angular relation $\theta(\Omega)$ in Fig. 2.4c, we can transform the beating frequency Ω to the angle $\theta^{'}$ of the reflected light and reconstruct an image of the object. Since the linewidth of the beating peak is only ∼100 Hz, the angular resolution is diffraction limited. We demonstrate imaging of a cutout of a husky dog logo made of a retroreflective film with a size of 60 mm × 50 mm and placed at 1.8 meters from the LiDAR. Since AOBS scans the beam in the horizontal dimension, a galvo mirror is used to scan in the vertical direction. The acquired LiDAR image is shown in Fig. 2.8c. The position of each pixel in the image is resolved from the corresponding beating frequency, and the brightness from the signal intensity. Fig. 2.8d and e show the beating signals of two pixels in the image, centered at 1.6575 GHz and 1.7125 GHz, respectively. We note an important advantage of the FAR scheme demonstrated here. After the initial calibration of the $\theta(\Omega)$ relation (Fig. 2.4d), the receiver works independently from the transmitter to determine the angular position from the beating frequency. Because of this, the receiver does not need to share the optical aperture with the transmitter, so it has the freedom to use a much larger aperture, collecting reflected light more efficiently and improving detection sensitivity. In contrast, in other scanning LiDAR schemes, to retrieve the angular information the receiver needs to share the aperture and work synchronously with the transmitter, and thus faces limitations. We also measured the point-to-point switch speed of AOBS, which determines the imaging speed. The measured rising time is 1.5 μs (Fig. 2.11), likely limited by the electronic system as it is much longer than the fundamental limit of the acoustic wave transit time ∼0.19 μs in the effective aperture.

To achieve 3D imaging, we add FMCW ranging to the FAR LiDAR to measure the depth of the object. FMCW is a coherent ranging technique that is advantageous over incoherent techniques such as pulsed time-of-flight. Thanks to the use of GHz frequency acoustic waves, the AOBS affords enough bandwidth to accommodate both FAR and FMCW. To chirp the optical frequency, we drive the EOM (Fig. 2.8a) at frequency $\Delta\omega$, which creates two sidebands at $\omega_0 \pm \Delta\omega$. Both can be used as the chirped source by modulating the drive frequency with a triangular waveform $\Delta\omega(t)$ at a chirping rate $g = \frac{d(\Delta\omega/2\pi)}{dt}$. The receiver

measures the beating frequency f_B between the local reference signal and the reflected light to determine the distance of the object: $d = cf_B/2g$. Fig. 2.9a shows the time-frequency map of the chirped optical source at the transmitter, which is the reference signal, and the reflected optical signal from a reflector at the receiver. For clarity, both signals are offset to the baseband. Note that the reflected signal has an additional frequency offset of the acoustic frequency $\Omega/2\pi$ and has a delay due to the time of flight $2d/c$. The beating frequency between the reference signal and the reflected signal thus alternates between $\Omega/2\pi \pm f_B$ with time (Fig. 2.9b, upper panel). However, since both sidebands are involved and their frequencies are chirped in opposite directions, the beating signal at the receiver has frequencies at both $\Omega/2\pi \pm f_B$ all the time. The acoustic frequency $\Omega/2\pi$ is also present due to the unsuppressed carrier. This is shown in the measured time-frequency map in Fig. 2.9b (lower panel). Fig. 2.9c shows the spectra of the beating signal when three different acoustic frequencies $\Omega/2\pi$ are used to steer beams in different directions, where they are reflected by reflectors placed at different distances up to 3 meters. The spectra contain a frequency component at the acoustic frequency $\Omega/2$, which is used for FAR imaging, and a frequency component at $\Omega/2\pi + f_B$ ($\Omega/2\pi - f_B$ is not shown) with an MHz beating frequency f_B, which increases with the reflector's distance. Therefore, by resolving all these frequency components, simultaneous FAR and FMCW measurements and a full 3D LiDAR image can be acquired in one scan. This is what we demonstrate in Fig. 2.9d, where we image a pair of 1/2-20 stainless steel screw bolt and nut (inset, Fig. 2.9d) placed 0.5 m from the LiDAR. The acquired point cloud image in Fig. 2.9d clearly shows the shape of the two objects separated by 8 cm in the depth direction. Each point is reconstructed from the frequency-domain spectrum of the FAR+FMCW signal. The chirping rate used is 1.0 MHz/μs with a frequency excursion f_E=1 GHz. Fig. 2.9e shows the raw data for two points, A on the bolt and B on the nut. Fig. 2.9f shows the detail of the FMCW beating signals in Fig. 2.9e. The distance measurement resolution is 7.5cm, which can be improved by increasing f_E.

In conclusion, we have demonstrated 3D imaging using a novel FAR and FMCW LiDAR scheme enabled by an AOBS device, which harnesses the physics of Brillouin scattering

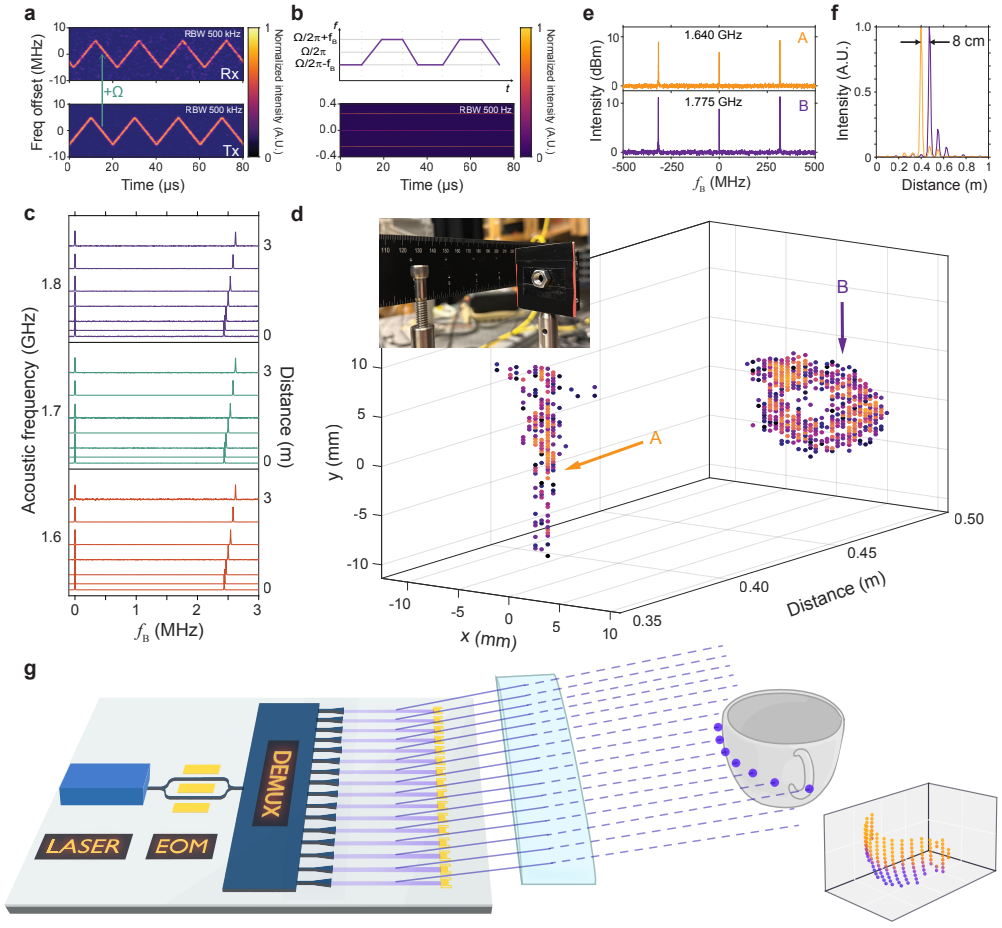
a
b
c
d
e
f
g
RBW 500 kHz
Rx
Tx
+Ω
Freq offset (MHz)
Time (μs)
Normalized intensity (A.U.)
RBW 500 Hz
Ω/2π+f_B
Ω/2π
Ω/2π-f_B
1.640 GHz
1.775 GHz
A
B
Intensity (dBm)
f_B (MHz)
Intensity (A.U.)
8 cm
Distance (m)
Acoustic frequency (GHz)
Distance (m)
y (mm)
x (mm)
LASER
EOM
DEMUX

Figure 2.9: **3D Imaging by FMCW and FAR LiDAR.** a. Time-frequency map of the transmitted light (bottom) and received light (top), both are chirped by a triangular waveform. The chirping rate is g=1 MHz/μs. The frequency of the received light is upshifted by the acoustic frequency $\Omega/2\pi$. b. Top: Schematic illustration of the FMCW signal's frequency as a function of time. The frequency alternates between $\Omega/2\pi \pm f_B$. Bottom: measured time-frequency map of the FMCW signal. Because of the USB and LSB generated by the EOM, the FMCW frequencies at $\Omega/2\pi \pm f_B$ are present all the time. Also present is the frequency component at $\Omega/2\pi$, which is from the unsuppressed optical carrier and used for FAR imaging. c. Spectra of FMCW signals when different acoustic frequencies (red:1.6 GHz, green: 1.7 GHz, purple:1.8 GHz) are used to steer the beam to reflectors placed at different angles and distances. d. 3D LiDAR image of a stainless-steel bolt and a nut, placed 8.0 cm apart from each other, acquired by combining FAR and FMCW schemes. The FMCW chirping rate is g=1 MHz/μs and frequency excursion f_E=1 GHz. Inset: photograph of the bolt and nut as the imaging objects. e. FMCW Spectra of two representative points (A and B) in d, showing signals at $\Omega/2\pi$ offset to zero frequency) and $\Omega/2\pi \pm f_B$ (offset to $\pm f_B$). f. Zoomed in view of the FMCW signals at f_B for point A and B. g, Our vision of a monolithic, multi-element AOBS system for 2D scanning and LiDAR imaging.

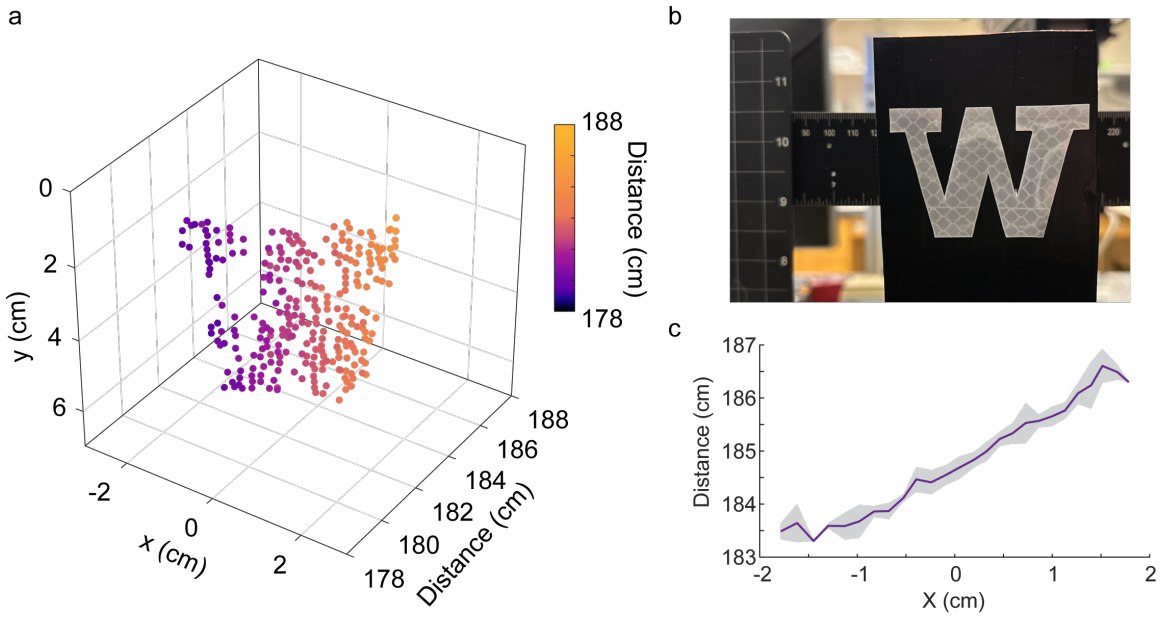

Figure 2.10: **3D imaging of an object.** a, A 3D FMCW and FAR LiDAR image of a letter "W" cutout made of a retroreflective film and placed 1.8 meters away. b, Photograph of the "W" cutout. c, X-Z plane projection of the captured image, showing sub-centimeter level depth measurement resolution (standard deviation, shaded area).

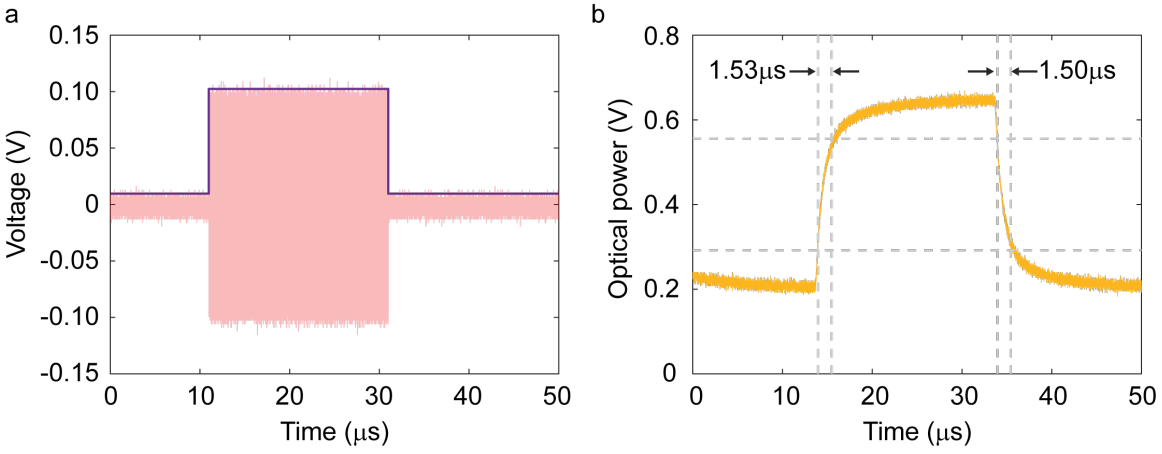

Figure 2.11: **AOBS dynamic response.** The temporal response of one AOBS pixel was characterized by measuring the output beam optical power (b) when the RF drive signal was modulated by a square wave (a). The 20%-80% rise time is measured to be 1.53 μs.

to achieve beam steering controlled by only one RF source. AOBS uniquely performs the transformation between the angle and frequency of the steered light, enabling imaging in the frequency domain. The single AOBS prototype demonstrates a FOV of 18°, an angular resolution of 0.12°, and an electronics-limited switching speed of 1.5 μs, which corresponds to an imaging rate of 0.67 megapixels/second. If using 16 channels (Fig. 2.4e) for LiDAR imaging, one AOBS device provides an imaging rate of more than 10 megapixels/second, which can be improved to much higher with faster electronics such as ASIC or FPGA. Looking forward, there is much room to improve the system's performance. With one IDT, each AOBS scans the beam in one dimension. 2D scanning can be achieved with an array of AOBS devices (Fig. 1c), each scanning independently to cover the horizontal dimension, as illustrated in Fig. 2.9g. Advanced IDT designs, such as single-phase unidirectional transducers (SPUDTs) [28,92], can not only increase the acoustic bandwidth and thus the AOBS FOV, but also afford much higher electromechanical conversion efficiency and unidirectional acoustic wave generation to increase beam steering efficiency. Furthermore, a few AOBS devices with different central acoustic frequencies can be combined to cover an even larger FOV. The steering efficiency of the current device is mainly limited by the relatively high acoustic loss which reduces the effective AOBS aperture to less than 1 mm. By using higher quality material platforms [89, 90], the acoustic loss can be reduced so that a much longer aperture can be achieved to significantly improve the efficiency based on our simulation (Supplementary Information). Moreover, the electro-optic modulator needed for FMCW can also be co-integrated on the LN platform (Fig. 2.9g) [90, 93], making a fully monolithic transmitter module. With these improvements and innovations, a multi-element, chip-scale AOBS system can afford efficient 2D beam steering covering a large FOV. The combined advantages of simple device structures, simple beam steering control, frequency domain resolving capability, miniature form factor, and low cost make the demonstrated AOBS-based LiDAR a promising technology for a wide range of applications, ultimately making LiDAR a commodity technology with widespread adoption in automation, industrial sensing, and consumer electronics for virtual and augmented reality.

2.5 Appendix

2.5.1 Perturbation theory of acosuto-optic scattering in a planar waveguide

In the Brillouin scattering process, the modulation of the material's refractive index by the acoustic wave is relatively small compared to fabricated photonic structures. The refractive index change induced by the photoelastic effect ($\Delta n/n$) is typically on the order of 10^{-4} or less while the mechanically induced geometry displacement is several orders smaller than the optical wavelength. To simulate the AOBS process with the finite-difference time-domain (FDTD) method, a large number of computational cells with sub-wavelength dimensions are required, making the calculation very inefficient. However, the AOBS process can be better modeled by a semi-analytical method using perturbation theory, where the acousto-optic interaction can be viewed as a perturbation to the light field. From [94], the Maxwell master equation can be described as,

$$\nabla \times \nabla \times E(r) = \omega^2 \mu_0 \varepsilon(r) E(r) \tag{2.5}$$

By choosing operators,$\Theta = \nabla \times \nabla \times, \hat{\varepsilon} = \varepsilon(r)$, the master equation of the electrical field can be treated as the generalized eigenvalue problem, $\Theta|E\rangle = \omega^2 \mu_0 \hat{\varepsilon}|E\rangle$, where the eigenvector *E(r)* is the spatial distribution of the waveguide mode and the eigenvalue ω is the mode frequency. Then the perturbation to the permittivity operator is introduced as follows, $\hat{\varepsilon} \to \varepsilon_0 + \lambda\varepsilon_1$.

Similar to the treatment of perturbation theory in quantum mechanics [95], the new eigenvector and eigenvalue can be expanded as Maclaurin power series,

$$\begin{aligned} |E\rangle &= |E_0\rangle + \lambda |E_1\rangle + \cdots \\ \omega &= \omega_0 + \lambda\omega_1 + \cdots \end{aligned} \tag{2.6}$$

, where the first order equation is,

$$\Theta |E_1\rangle = \omega_0^2 \mu_0 \varepsilon_1 |E_0\rangle + \omega_0^2 \mu_0 \varepsilon_0 |E_1\rangle + 2\omega_0 \omega_1 \mu_0 \varepsilon_0 |E_0\rangle \tag{2.7}$$

. By integrating the equation with the unperturbed eigenmode E_0, the perturbation of the eigenfrequency ω_1 (the frequency shift from the unperturbed mode E_0) can be described as

the following,

$$\omega_1 = -\frac{\omega_0}{2}\frac{\langle E_0 \left|\varepsilon_1\right| E_0\rangle}{\langle E_0 \left|\varepsilon_0\right| E_0\rangle} \tag{2.8}$$

. If we define an equivalent polarization current density as $J = -i\omega_0\varepsilon_1 E_0$, ω_1 can be expressed with the perturbation-induced current density J,

$$\omega_1 = -\frac{i}{2}\frac{\langle E_0 \mid J\rangle}{\langle E_0 \left|\varepsilon_0\right| E_0\rangle} \tag{2.9}$$

. In an AOBS device, the surface acoustic wave (SAW) forms a moving grating to scatter the guided optical mode into radiative modes. Therefore, the imaginary part of ω_1 corresponds to the propagation loss of the guided mode attributed to the acousto-optic scattering. Thus, the scattering rate (propagation loss) is $\alpha = 2\,\mathrm{Im}(\beta) = 2\,\mathrm{Im}\left(\omega_1\right)/v_g$, where β and v_g are the wavenumber and group velocity of the guided mode, respectively. The moving grating generated by the acoustic wave has two contributions: the geometry deformation at the boundary of the waveguide, and the refractive index changing induced by the photoelastic effect. Therefore, the SAW-induced equivalent polarization current density can be divided into two parts,

$$J = J_{mb} + J_{pe} \tag{2.10}$$

, where J_mb and J_pe are the polarization current produced the moving boundary effect and the photoelastic effect, respectively. According to [94], we can find that the moving boundary induced current density due to the displacement field u is,

$$J_{mb} = -i\omega_0 u \cdot n\left(\Delta\varepsilon_{12}E_{\parallel} - \varepsilon\Delta\varepsilon_{12}^{-1}D_{\perp}\right)\delta(\mathrm{z}) \tag{2.11}$$

, where the Dirac delta function $\delta(z)$ is to obtain a surface integral with z-direction along the surface normal, $\Delta\varepsilon_{12} = \varepsilon_1 - \varepsilon_2$ represents the permittivity difference across the boundary, ε_1^{-1} is the impermeability that $\Delta\varepsilon_{12^{-1}} = \varepsilon_1^{-1} - \varepsilon_2^{-1}$, $E_{\parallel}$ is the parallel component of E_0 to the interface, and $D_{\perp}$ is the perpendicular component of $D = \varepsilon E_0$. From this expression, the surface integral $\langle E_0 \mid J\rangle$ only has terms proportional to $\left|E_{\parallel}\right|^2$ and $|D_{\perp}|^2$, both of which are continuous across the interface, and can be numerically calculated. The photoelasticity induced current density J_pe can be expressed as,

$$J_{pe} = -i\omega_0\Delta\varepsilon_{pe}E_0 \tag{2.12}$$

, where $\Delta\varepsilon_{p\delta}$ is the permittivity changing inside the waveguide due to the photoelastic effect. Conventionally, such effect can be expressed as the change of the permittivity induced by the strain field S_{ij},

$$\begin{aligned} \Delta\varepsilon_{ij} &= -\frac{\varepsilon_i \varepsilon_j}{\epsilon_0} \sum_{kl} p_{ijkl} S_{kl} \\ S_{kl} &= \frac{1}{2}\left(\frac{\partial u_k}{\partial x_l} + \frac{\partial u_l}{\partial x_k}\right) \end{aligned} \tag{2.13}$$

, where p_{ijkk} are dimensionless elasto-optic coefficients and u is the displacement field. Therefore, the overall perturbed current density is as follows,

$$\begin{aligned} J &= J_{mb} + J_{pe} \\ &= -i\omega_0 \left[u \cdot n \left(\Delta\varepsilon_{12} E_{\parallel} - \varepsilon \Delta\varepsilon_{12}^{-1} D_{\perp} \right) \delta(\mathrm{z}) - \frac{\varepsilon_i \varepsilon_j}{2\epsilon_0} \sum_{kl} p_{ijkl} \left(\frac{\partial u_k}{\partial x_l} + \frac{\partial u_l}{\partial x_k} \right) E_0 \right] \end{aligned} \tag{2.14}$$

. For our interests of AOBS efficiency, the acousto-optic scattering rate α of the guided mode E_0 can be found from the equation,

$$\alpha = \frac{2\,\mathrm{Im}\,(\omega_1)}{v_g} = -\,\mathrm{Re}\left(\frac{\langle E_0 \mid J \rangle}{v_g \langle E_0 \left| \varepsilon_0 \right| E_0 \rangle} \right) \tag{2.15}$$

, which can be numerically calculated based on simulation results.

2.5.2 Real-space AOBS beam profile fitting model

The real-space beam-profile image shown in Fig. 2.4c indicates that the emission from the AOBS decays along the acoustic wave propagation direction, due to the significant acoustic propagation loss in the waveguide. We can write down the differential equations to describe the scattering process of both acoustic waves and optical waves. Both the acoustic wave and the optical modes decay when propagating due to the AO scattering and intrinsic loss. To estimate the AO scattering rate and acoustic propagation loss, we assume the intrinsic optical loss is low and the optical loss is dominated by the AO scattering. The depletion of acoustic power during the AO scattering can also be neglected compared to its attenuation. Under these assumptions, the acoustic power density P_a and the input optical power P_o can

be written as,

$$\begin{aligned} \partial_x P_o &= \kappa P_a P_o \\ \partial_x P_a &= -\gamma P_a \end{aligned} \tag{2.16}$$

, where κ is the acousto-optic scattering rate. Suppose the source of the acoustic wave is at $x = 0$ (front edge of the IDT), by solving the above equations, the expressions for the acoustic mode, optical guided mode, and the AO scattering power P_r are expressed by, respectively,

$$\begin{aligned} P_a(x) &= e^{-\gamma x} P_a(0) \\ P_o(x) &= e^{\frac{\kappa'}{\gamma}\left(e^{-\gamma l} - e^{-\gamma x}\right)} P_o(l) \\ P_r(x) &= -\partial_x P_o(x) = \kappa' P_o(l) e^{\frac{\kappa'}{\gamma}\left(e^{-\gamma l} - e^{-\gamma x}\right) - \gamma x} \end{aligned} \tag{2.17}$$

, where $\kappa' = \kappa P_{\mathrm{a}}(0)$. The overall scattering efficiency is thus:

$$\eta = \frac{\int_0^l P_r(x)}{P_o(0)} = 1 - e^{\frac{\kappa'}{\gamma}\left(e^{-\gamma l} - 1\right)} \tag{2.18}$$

. The scattered optical power $P_r(x)$ is captured by the camera as the real-space image of the scattering intensity at the AOBS aperture. Therefore, by fitting the light intensity in Fig. 2.4c with $P_r(x)$, we can extract the AO scattering rate of κ' =0.23 dB/mm and an acoustic propagation loss of γ =7.08 dB/mm. The corresponding acoustic propagation length is 0.6 mm. The overall AO scattering efficiency is η =2.8%.

If the acoustic loss can be reduced, by improving the material quality, the efficiency η can be significantly improved. For example, if γ can be reduced to 0.2 CM^{-1} (acoustic decay length 5 cm), the efficiency η if 22% in an AOBS device with 5 mm long aperture and 1 mW/μm acoustic power density, while the efficiency can even reach 92%, with an increased 10 mW/μm acoustic power density, which are both realistic.

2.5.3 Analysis of the FMCW measurement

The chirping signal that is used to modulate the laser in the FMCW measurement was generated by AWG. It can be expressed as,

$$V_c = \sin\left[2\pi\left(f_0 t + F(t)\right)\right] \tag{2.19}$$

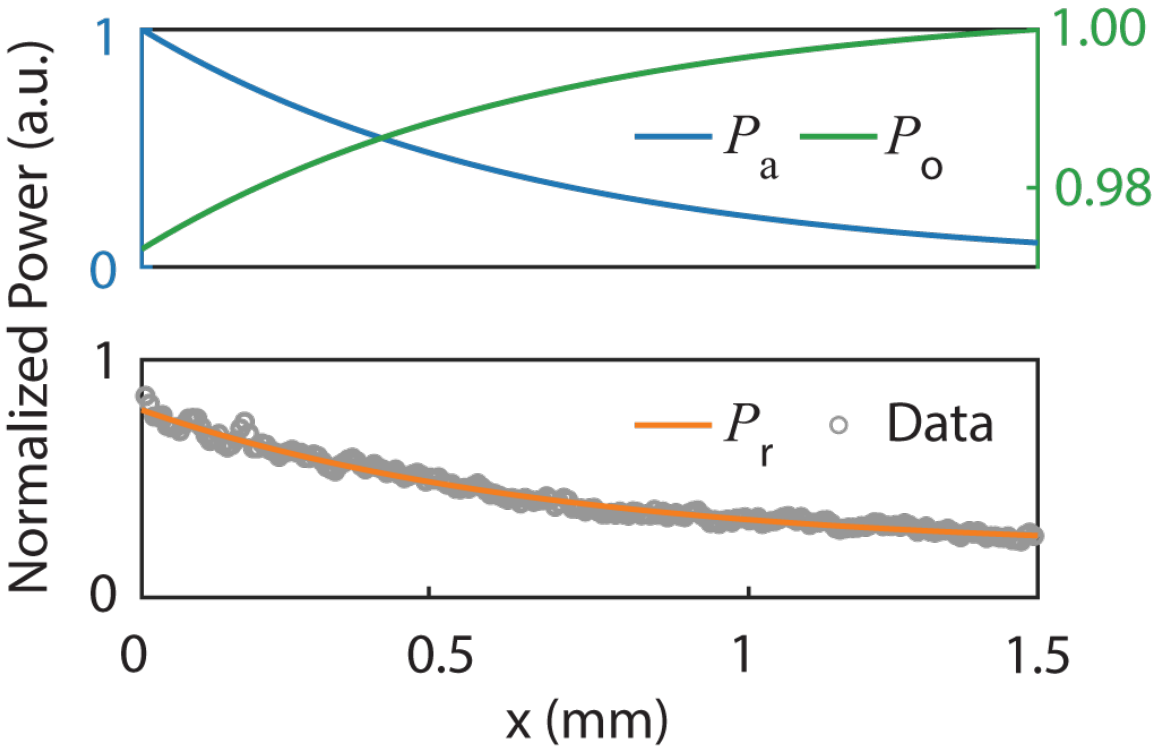

Figure 2.12: **Fitting result of the real-space AOBS scattering intensity.** The experimental data (gray circle) and the normalized fitted acoustic power density (Pa), guided optical modes power (P_o), and radiated power (P_r).

. $F(t)$ is characterized by $f_{\pm}(t) = \frac{dF_{\pm}(t)}{dt} = \pm f_{\mathrm{E}} t/T$, for the rising (+) and falling (−) edge of the chirping signal. The period is T , the frequency excursion is $f_E = f_1 - f_0$, and the chirp rate is $g_{\pm} = \pm 2\left(f_1 - f_0\right)/T$. This signal was then used to drive the EOM. The modulated optical field is,

$$\begin{aligned} E_m &= \widehat{E}_{\mathbf{0}} e^{j[\omega t + \delta \sin(2\pi F(t))]} \\ &= \widehat{E}_{\mathbf{0}} \sum_{-\infty}^{+\infty} J_n(\delta) e^{j(\omega t + 2n\pi F(t))} \end{aligned} \tag{2.20}$$

, where δ is the modulation strength and $J_v(x)$ is the v-th order Bessel function of the first kind. The chirped light was split to two parts. One was sent to the AOBS device, which was then diffracted by the acoustic wave of frequency Ω. The other part was used as the LO. The scattered light was frequency shifted by the acoustic such that it can be expressed by,

$$E_{bs} = \widehat{E}_a \sum_{-\infty}^{+\infty} J_n(\delta) e^{j(\omega t + \Omega t + 2n\pi F(t))} \tag{2.21}$$

The received field obtains a phase delay $\tau = 2R/c$ over a range R,

$$_r = \widehat{E}_a \sum_{-\infty}^{+\infty} J_n(\delta) e^{j[(\omega+\Omega)(t+\tau) + 2n\pi F(t+\tau)]} \tag{2.22}$$

The received signal was combined with the LO by a 50/50 fiber coupler. The output of the fiber coupler was detected by a BPD. The voltage output of the BPD can be written as,

$$V_B \propto 4\,\mathrm{Im}\left(E_r E_{LO}^*\right) \tag{2.23}$$

The generated beating signal was then measured by an RSA. If we only consider the first order sideband of the EOM modulated light, the output voltage of the BPD consists of nine terms. Within the RSA measurement bandwidth, there are three frequency components centered at Ω and $\Omega \pm f_{\mathrm{B}}$. The corresponding signals come from the following beating terms between the baseband and the frequency-shifted signals:

$$\begin{aligned} V_0(t,\tau) &\propto J_0(\delta)^2 \sin\left(\Omega t + \phi_0\right) \\ V_1(t,\tau) &\propto J_1(\delta)^2 \sin\left[\Omega t + 2\pi F(t-\tau) - 2\pi F(t) + \phi_1\right] \\ V_{-1}(t,\tau) &\propto J_{-1}(\delta)^2 \sin\left[\Omega t - 2\pi F(t-\tau) + 2\pi F(t) + \phi_{-1}\right] \end{aligned} \tag{2.24}$$

, where $\phi_{0,\pm1}$ are time independent phases in each term. We need to mention that V_0 is a single-frequency signal, while the signals of the V_1 and V_-1 are both phase modulated by the linear chirping drive $F(t)$. The angular information is carried by the RF frequency Ω, and distance information can be extracted from the beating between the LO and the received signal $[F(t-\tau)-F(t)]$, which is a periodic function with period T. To analyze the beating of the chirped signals, we use $V_1(t,)$ as an example and do Fourier expansion to obtain amplitudes at each harmonic,

$$\begin{aligned} V_1 &\propto \sin\left[\Omega t + 2\pi F(t-\tau) - 2\pi(t) + \phi_1\right] \\ &= \sin\left(\Omega t + \phi_1\right)\cos[2\pi F(t-\tau) - 2\pi F(t)] + \cos\left(\Omega t + \phi_1\right)\sin[2\pi F(t-\tau) - 2\pi F(t)] \end{aligned} \tag{2.25}$$

. For simplicity, we do not consider sampling time and considered the signal as an infinitely long periodic function. In this case, the frequency modulated sine and cosine terms can be expanded as Fourier series,

$$\begin{aligned} \cos[2\pi(F(t-\tau)-F(t))] &= \frac{\mathrm{a}_0}{2} + \sum_{n=1}^{\infty} a_n \cos\left(\frac{2\pi n t}{T}\right) \\ \sin[2\pi(F(t-\tau)-F(t))] &= \frac{\mathrm{b}_0}{2} + \sum_{n=1}^{\infty} b_n \sin\left(\frac{2\pi n t}{T}\right) \end{aligned} \tag{2.26}$$

. By calculating the Fourier coefficients and assuming $\tau << T$, the beating signal can be rewritten as,

$$\begin{aligned} V_1 &\propto \sin\left(\Omega t + \phi_1 \pm \phi'\right) \sum_{n=1}^{\infty} \left[\mathrm{sinc}\left(2f_E\tau + n\right) + \mathrm{sinc}\left(2f_E\tau - n\right)\right] \cos\left(\frac{2\pi n t}{T}\right) \\ &= \cos\left(\Omega t + \phi_1 \pm \phi'\right) \sum_{n=1}^{\infty} \mp \left[\mathrm{sinc}\left(2f_E\tau - n\right) - \mathrm{sinc}\left(2f_E\tau + n\right)\right] \sin\left(\frac{2\pi n t}{T}\right) \\ &= \mathrm{sinc}\left(2f_E\tau + n\right) \sin\left(\Omega t + \frac{2n\pi t}{T} + \phi_1 + \phi'\right) \\ &+ \mathrm{sinc}\left(2f_E\tau - n\right) \sin\left(\Omega t - \frac{2n\pi t}{T} + \phi_1 - \phi'\right) \end{aligned} \tag{2.27}$$

. The V_{-1} has a similar expression. The output voltage BPD at Ω and $\Omega \pm f_B$ are,

$$\begin{aligned}
&V_{FAR}(t,\tau) \propto J_0(\delta)^2 \cos(\Omega t) \\
&V_{USB}(t,\tau) \propto J_1(\delta)^2 \sum_{n=1}^{\infty} \operatorname{sinc}(2f_E\tau - n) \left\{ \cos\left[2\pi\left(\Omega + \frac{n}{T}\right)t + \phi_1 - \phi'\right]\right. \\
&\left. + \cos\left[2\pi\left(\Omega + \frac{n}{T}\right)t + \phi_{-1} - \phi'\right]\right\} \\
&V_{LSB}(t,\tau) \propto J_1(\delta)^2 \sum_{n=1}^{\infty} \operatorname{sinc}(2f_E\tau + n) \left\{ \cos\left[2\pi\left(\Omega + \frac{n}{T}\right)t + \phi_1 + \phi'\right]\right. \\
&\left. + \cos\left[2\pi\left(\Omega + \frac{n}{T}\right)t + \phi_{-1} + \phi'\right]\right\}
\end{aligned} \tag{2.28}$$

. It shows that the repetition of the chirp signal induced discrete peaks with an equal spacing $1/T$, starting from the RF frequency Ω. Therefore, ranging resolution by global maximum peak detection method is limited by,

$$\begin{aligned}
\frac{2\Delta R}{c}\frac{2f_E}{T} &\geq \frac{1}{T} \\
\Delta R &\geq \frac{c}{4f_E}
\end{aligned} \tag{2.29}$$

To achieve higher ranging resolution, we used sinc functions to fit the beating signal. The center of the sinc function shows a fitted depth and the resolution is defined by fitting error.

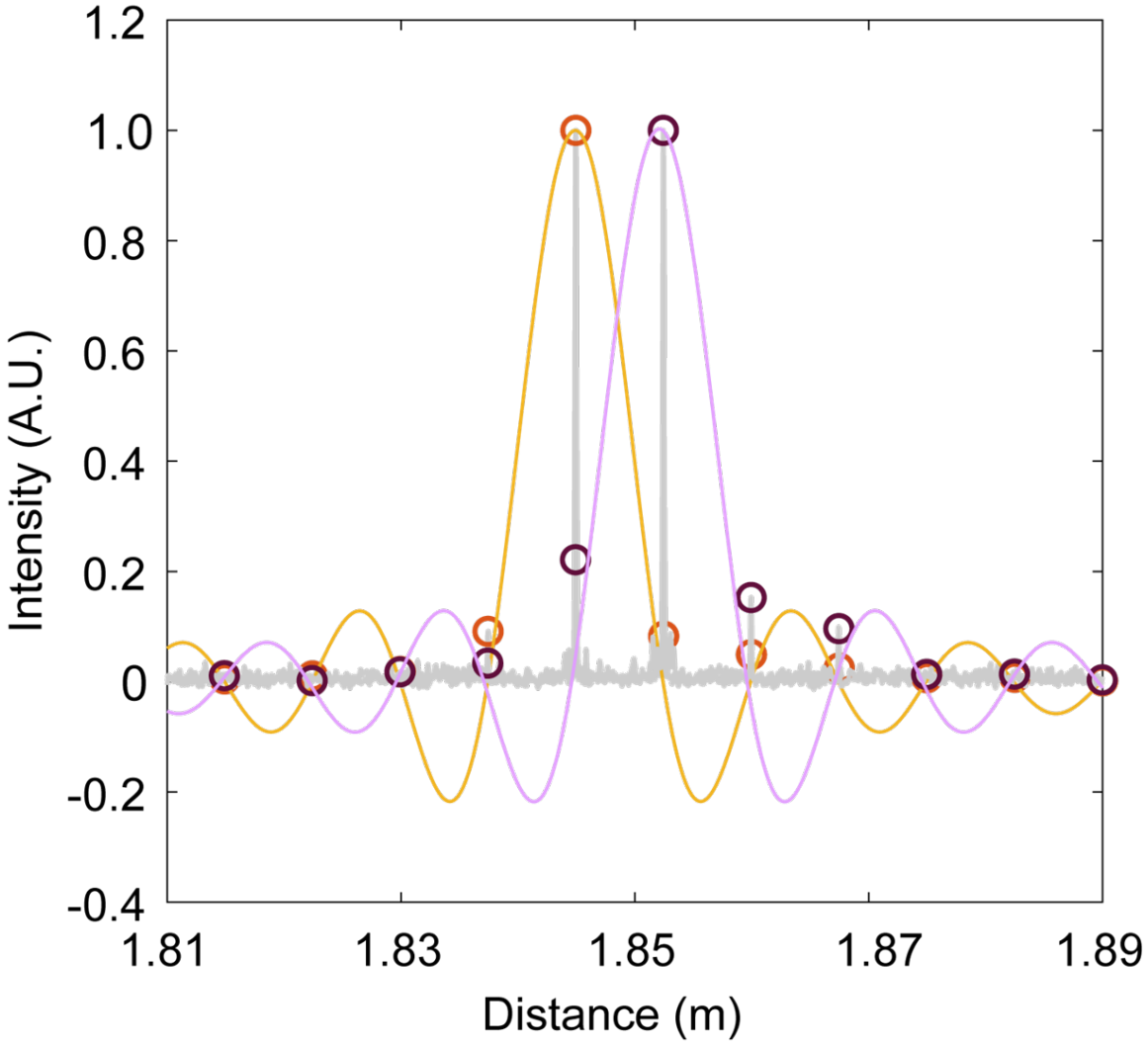

Figure 2.13: **Fitting result of two points captured in Fig. 2.10a.**

Chapter 3

SCALING SILICON PHOTONIC COMPUTING IN SYNTHETIC FREQUENCY DIMENSION

Optical computing with integrated photonics brings a pivotal paradigm shift to data-intensive computing technologies. However, the scaling of on-chip photonic architectures using spatially distributed schemes faces the challenge imposed by the fundamental limit of integration density. Synthetic dimensions of light offer the opportunity to extend the length of operand vectors within a single photonic component. Here, we show that large-scale, complex-valued matrix-vector multiplications on synthetic frequency lattices can be performed using an ultra-efficient, silicon-based nanophotonic cavity acousto-optic modulator. By harnessing the resonantly enhanced strong electro-optomechanical coupling, we achieve, in a single such modulator, the full-range phase-coherent frequency conversions across the entire synthetic lattice, which constitute a fully connected linear computing layer. Our demonstrations open up the route towards the experimental realizations of frequency-domain integrated optical computing systems simultaneously featuring very large-scale data processing and small device footprints.

3.1 Introduction

Analog optical computing encodes and processes data using continuously variable quantities of light [96–98]. While optical nonlinearity requires high power expense, linear optical components can perform data movement, temporal-spatial signal processing and multiply-accumulate operations with potentially unparalleled bandwidth, speed and energy efficiency [99–102]. As the current digital electronic computing technologies approach the physical limit, such advantages of optics motivate the recent development in building optical accelerators that can sustain the ever-growing data demand at the hardware level [93,103–110]. Integrated photonics provides a powerful optical computing platform that benefits from

scalable fabrications and integration compatibility with electronic circuits, affording architectures with rapid programmability [93, 106–110]. Considerable progress has been made in building integrated photonic neural networks with high data throughput by incorporating time and/or wavelength division multiplexing [109, 110]. However, realizing large-scale, fully connected networks on photonic chips can be very challenging. Most N × N optical computing layers based on spatial encoding require O(N2) scaling of photonic components, occupying huge device footprints compared to the electronic counterparts. Such footprint-inefficient scaling poses a major roadblock for integrated photonic computing from being applied in some important architectures such as the multilayer perceptron (MLP) [111].

The emerging notion of synthetic frequency dimension provides a promising strategy to drastically scale up the optical computing systems in both classical and quantum regimes [68,112–119]. Encoding information as coherent optical fields on a synthetic frequency lattice increases the fan-in/fan-out of a single photonic logic unit, thus improving the scalability of data processing by orders of magnitudes. The implementations of frequency-domain N×N optical networks require efficient modulators that simultaneously link the N discrete nodes via coherent frequency conversions [113, 119]. For this purpose, integrated acousto-optic modulators can stand out with high modulation efficiency and large modulation depth by exploiting the strong optomechanical interaction between co-localized optical and acoustic modes [49, 63, 67, 68, 120]. Recent thin-film lithium niobate modulators have reached modulation depth that can couple a few sidebands [49, 121]. Nonetheless, a single device that can compose a fully connected computing layer on a sizable synthetic frequency lattice remains unrealized. Achieving the most efficient on-chip acousto-optic modulation requires simultaneously optimized optomechanical coupling and piezoelectric transduction on a monolithic material platform. To this end, the heterogeneous integration of silicon on insulator (SOI) with complementary metal-oxide-semiconductor (CMOS)-compatible piezoelectric materials such as aluminum nitride (AlN) holds promise for high-performance integrated modulators [**?**, 31, 122], which will offer the key building blocks for data-intensive frequency-domain optical computing systems.

Here, we demonstrate scalable matrix-vector multiplications (MVM) in the synthetic fre-

quency dimension by leveraging an efficient nanophotonic cavity acousto-optic modulator on the AlN-on-SOI platform. The very large dynamic modulation depth arising from the engineered strong electro-optomechanical coupling enables the coherent frequency conversions among a myriad of sidebands spanning a synthetic frequency lattice. Thereby, with a single such modulator, we realize a large-scale, fully connected computing layer that performs linear transformations on the complex-valued vector inputs encoded as spectrally coherent optical fields (Fig. 3.1a). We highlight the advantage of the persistent long-range spectral phase coherence of the MVM operations performed by our modulator. Our device contributes the critical component to a highly scalable and hardware-efficient integrated photonic computing architecture based on concatenated layers of modulators.

3.2 Device Structure and Fabrication

3.2.1 Design of the Acousto-Optic Modulator

Fig. 3.1(b) shows a scanning electron microscopy (SEM) image of our device fabricated on an AlN-on-SOI substrate. The modulator consists of a one-dimensional photonic crystal cavity etched in a suspended silicon rib waveguide which is connected to the AlN/Si piezoelectric region with a silicon sleeve area in between. The nanophotonic cavity is end-coupled to a pair of grating couplers for optical input/output. We achieved a high loaded quality factor $Q_{\mathrm{L}} = 4.6 \times 10^5$, corresponding to a total cavity loss rate of $\kappa = (2\pi) \cdot 420\mathrm{MHz}$ (Fig. 3.1c). Acoustic waves are excited by driving a split-finger interdigital transducer (IDT) patterned on the free-standing AlN/Si region with an RF signal, and subsequently propagate to the optical waveguide via the silicon membrane. The IDT is designed with a period of 3 μm to excite a set of mechanical modes with angular frequencies $\Omega > \kappa$, reaching the sideband-resolved regime (Fig. 3.8a). By etching a free-edge reflector on the lower side of the waveguide, we create an acoustic resonator that coherently builds up a strong mechanical displacement field at the nanophotonic cavity.

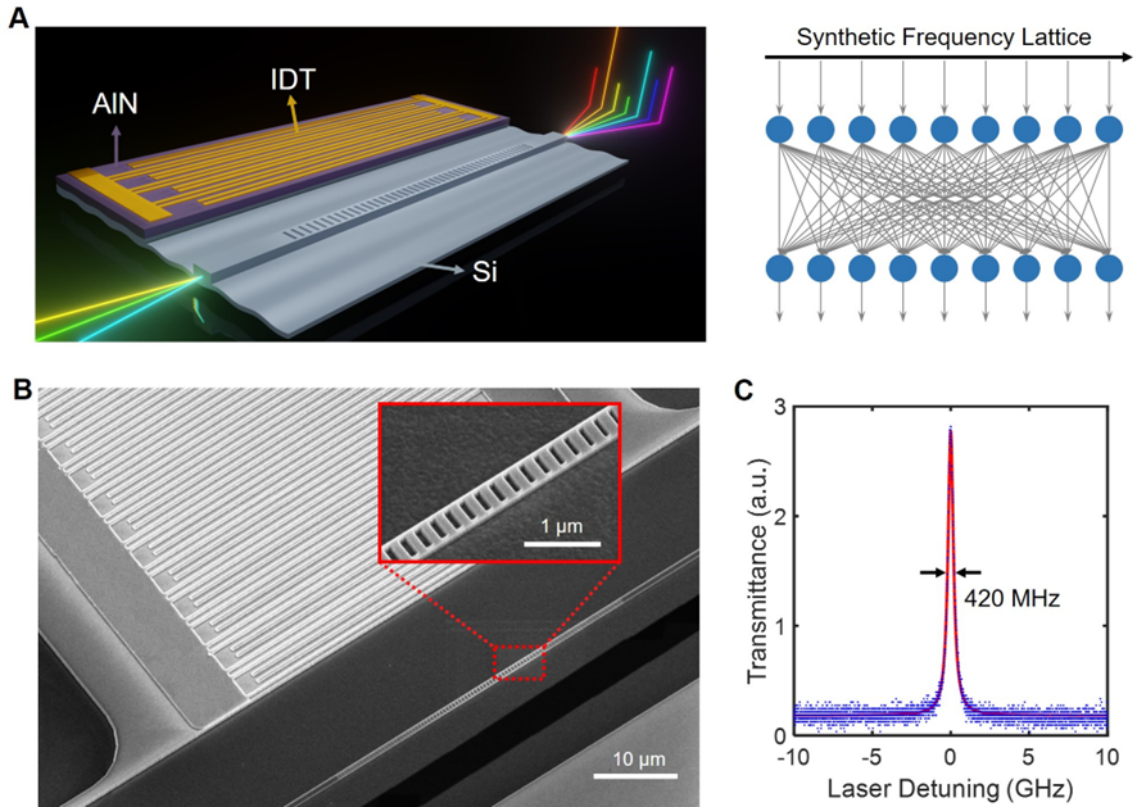

Figure 3.1: **Nanophotonic cavity acousto-optic modulator that performs scalable matrix-vector multiplications in the synthetic frequency dimension.** a. Schematic illustration of our acousto-optic modulator, which is equivalent to a fully connected linear optical computing layer on the synthetic frequency lattice. b. SEM image of the modulator fabricated on the AlN-on-SOI platform. Inset is the zoom-in image of the nanophotonic cavity. c. Measured optical transmission spectrum without modulation, showing a linewidth of 420 MHz. The center optical resonance wavelength is around 1547.5 nm.

3.2.2 Fabrication of the cavity acousto-optic modulator on the AlN-on-SOI platform.

Our cavity acousto-optic modulator was fabricated by the processes shown in Fig. 3.2. The substrate was prepared by sputtering 320-nm thick polycrystalline aluminum nitride (AlN) on silicon-on-insulator (SOI) wafer with 220-nm Si layer (grown by OEM group). Before patterning the structure, a layer of silicon dioxide (SiO_2) was deposited as a hard mask by plasma-enhanced chemical vapor deposition (PECVD). We first patterned the window for Si photonic structures by electron-beam lithography (EBL) with positive ZEP520 resist (developer: amyl acetate), which was subsequently transferred to the SiO_2 hard mask by fluorine-based inductively-coupled-plasma etching (ICP-F). The exposed AlN in the window was removed by another step of chlorine-based inductively-coupled-plasma etching (ICP-C) with $Cl_2/BCl_3/Ar$ chemistry followed by nitrogen plasma cleaning. The etching time was precisely controlled to remove only the targeted AlN layer. The Si photonic structures, including the one-dimensional photonic crystal cavity, grating couplers and waveguide, were patterned using aligned EBL and negative hydrogen silsesquioxane (HSQ) resist (developer: tetramethylammonium hydroxide, TMAH), followed by an ICP-C etching with Cl2 plasma. Another round of aligned EBL (resist: ZEP520) and ICP-C was applied to etch through the free-edge reflector and the releasing windows for the final releasing step. The remaining positive resist and on-top oxide (including the remaining HSQ) were removed by N-Methyl-2-pyrrolidone (NMP) and buffered oxide etchant (BOE), respectively. We then patterned the interdigital transducer (IDT) using a third-time aligned EBL (resist: ZEP520), followed by electron-beam evaporation (Evap) of aluminum and lift-off in NMP. Finally, the device was released by vapor hydrofluoric (HF) acid which etched away the buried oxide layer to achieve the suspended structures. The parameters of our fabricated device are listed in Table. 3.1.

3.3 Characterization of the AOM

Such mechanical motion effectively modulates the optical resonance through a combination of moving-boundary and photoelastic effects [13]. Under the modulation, the intra-cavity

Thickness of AlN (nm)	320	Thickness of Si (nm)	220
Thickness of buried oxide (μm)	3	Width of waveguide (nm)	550
Strip height of waveguide (nm)	150	Height of Si sleeve (nm)	70
Periodicity of photonic crystal (nm)	350	Depth of holes (nm)	150
Length of rectangular holes (nm)	375	Maximum hole width (nm)	180
Minimum hole width (nm)	80	Number of tapering	25
Thicknesses of Al electrodes (nm)	220	Periodicity of IDT (μm)	3
Width of IDT finger (nm)	375	Total IDT length (μm)	150
Distance from IDT to waveguide (μm)	10	Distance from waveguide to free-edge reflector (μm)	2.4

Table 3.1: **Parameters of the fabricated cavity acousto-optic modulator** BS: optical in-line beam splitter; DUT: device under test; AOFS: fiber acousto-optic frequency shifter; OS: optical switch; LPD: low-speed photodetector; EDFA: erbium-doped fiber amplifier; OBF: tunable optical bandpass filter; HPD: high-speed photodetector (12-GHz bandwidth); VNA: vector network analyzer.

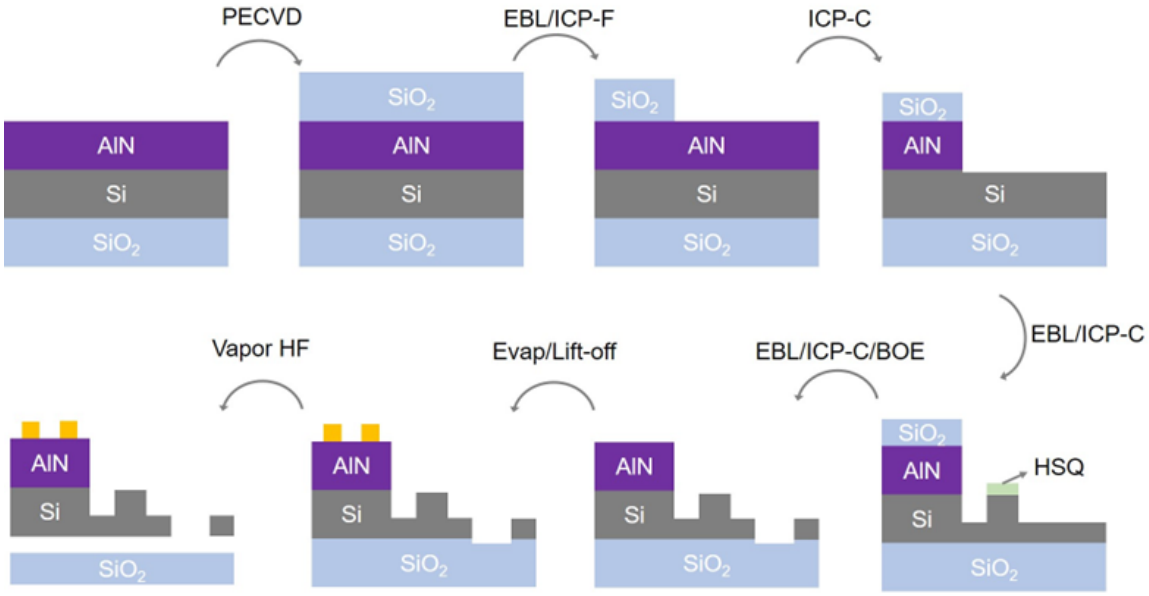

Figure 3.2: **Fabrication flow for the cavity acousto-optic modulator on hybrid AlN-on-SOI platform.**

photon dynamics can be described as,

$$\dot{a}(t) = [i(\Delta - \beta \cdot \hat{f}(t)) - \kappa/2]a(t) + \sqrt{\kappa_{\mathrm{ex}}}a_{\mathrm{in}}(t) \tag{3.1}$$

where κ_{ex} is the external coupling rate, $a_{\mathrm{in}}\ (t)$ is the input optical field, and $\Delta = \omega_{\mathrm{p}} - \omega_0$ is the detuning of the input laser (angular) frequency ω_{p} from the cavity center frequency ω_0. $\hat{f}(t)$ denotes the normalized acoustic waveform. $\beta = 2g_{\mathrm{om}}/\Omega$ is the modulation index that measures the dynamic modulation depth, where g_{om} is the optomechanical coupling proportional to the amplitude of the mechanical mode.

Our acousto-optic modulator features ultra-high modulation efficiency in the sideband-resolved regime. The resulting deep modulation can generate multiple resolved sidebands at $\omega_0 \pm s\Omega$ with integer sideband order s, forming a synthetic lattice in the frequency domain. To quantify the modulation efficiency and the achievable size of the synthetic lattice, we drive the IDT at the mechanical resonances and measure the optical transmission spectra

with varying RF power. Fig. 3.8b shows the results of the 2.903 GHz drive ($\Omega/\kappa \sim 7$), from which we infer a characteristic half-wave voltage $V_\pi = 580mV$ for $\beta = \pi$ by fitting the measurements with the theory. At an RF power of $3dBm$ ($\beta = 2.41$), we observe the emergence of multiple sidebands up to ±3rd orders, comprising a finite lattice of 7 sites. The 803 MHz drive ($\Omega/\kappa \sim 2$) can induce much more efficient modulation with the lowest $V_\pi = 19mV$ (Fig. 3.8c). We obtain the maximal $\beta = 22.9$ at an RF power of -7 dBm, which generates a synthetic lattice of approximately 50 sites over a wide frequency range of 40 GHz.

3.3.1 Analysis of the piezoelectrically transduced mechanical modes.

The IDT patterned on the heterogeneous AlN/Si region is used to resonantly excite multiple mechanical modes, which have very distinct acousto-optic modulation efficiencies on the nanophotonic cavity. To understand the relation between the acousto-optic modulations and these mechanical modes, we performed the numerical simulations (COMSOL Multiphysics 5.5) and show in Fig. 3.3 the displacement fields in the suspended AlN/Si layer, corresponding to the resonances measured by the IDT S_{11} response. The mechanical modes that are of the interest in the main text are the fundamental Lamb mode (large out-of-plane displacement) at 800 MHz and the fundamental compressional mode (large in-plane displacement) at 2.9 GHz. Because of the long wavelengths, these two modes strongly couple to the 70-nm Si membrane and the optical nanobeam cavity therefore can induce strong phase modulations. We characterize the acousto-optic modulations by measuring the microwave-to-optical transduction signal S_{OE} in Section 5 and exploit these modes for the frequency-domain matrix-vector multiplications.

Our IDT with the split-finger design can also excite higher-order mechanical modes with odd-number modal orders. In the 500 MHz to 8 GHz spectrum, Mode III is the 3rd-order Lamb mode; Mode V is the 5th-order compressional mode; Mode IV is the 3rd-oder Love mode; and Mode VII is the 3rd-oder AlN/Si Lamb-compression hybrid mode. These higher-order modes are associated with significantly reduced wavelengths which increase

the mechanical power dissipation and decrease the modal overlap between the mechanical modes and the optical cavity field (so weaker optomechanical coupling). Consequently, the higher-order mechanical modes have negligible acousto-optic phase modulation efficiencies (compared to the fundamental orders) and dominantly contribute to thermo-optic tuning of the optical cavity resonance. In addition, we also observe the excitations of a symmetric breathing mode (VI). Although this breathing mode shows a larger piezoelectric transduction efficiency, it does not couple to the acoustic wave in the silicon membrane (in Lamb mode) due to the mismatch of the modal symmetry, therefore has no phase modulation effect.

3.3.2 Analytical solutions to the intra-cavity photon dynamics.

The intra-cavity photon dynamics under the acousto-optic modulation (Eq. (1) in the main text) has explicit solutions when a single microwave tone is applied on the IDT, i.e. $\hat{f}(t) = \cos(\Omega t + \phi)$. The solution provides the insight of the physics under our interrogation. Therefore, before introducing our experimental characterizations, we show here the derivation of the analytical solutions of both the intra-cavity and the output optical fields.

We rewrite the dynamics with $\hat{f}(t) = \cos(\Omega t + \phi)$ as

$$\dot{a}(t) = i\Delta a(t) - i\beta \cdot \cos(\Omega t + \phi)a(t) - \kappa a(t)/2 + \sqrt{\kappa_{\mathrm{ex}}}a_{\mathrm{in}}(t) \tag{3.2}$$

, where $a(t)$ and $a_{in}(t)$ are the intra-cavity and input optical fields, respectively; κ and κ_{ex} denote the total optical cavity decay rate and external coupling rate, respectively; $\Delta = \omega_{\mathrm{p}} - \omega_0$ is the detuning of the input laser angular frequency ω_p from the cavity center frequency ω_0; Ω, ϕ are the frequency and phase of microwave drive applied to the IDT, respectively; $\beta = 2g_{\mathrm{om}}/\Omega$ is the modulation index; and g_{OM} is the total optomechanical coupling. By the transformation $a(t) = \alpha(t)\exp[-i\beta\sin(\Omega t + \phi)]$, we obtain

$$\dot{\alpha} = (i\Delta - \kappa/2)\alpha + \sqrt{\kappa_{\mathrm{ex}}}e^{i\beta\sin(\Omega+\phi)}a_{\mathrm{in}} \tag{3.3}$$

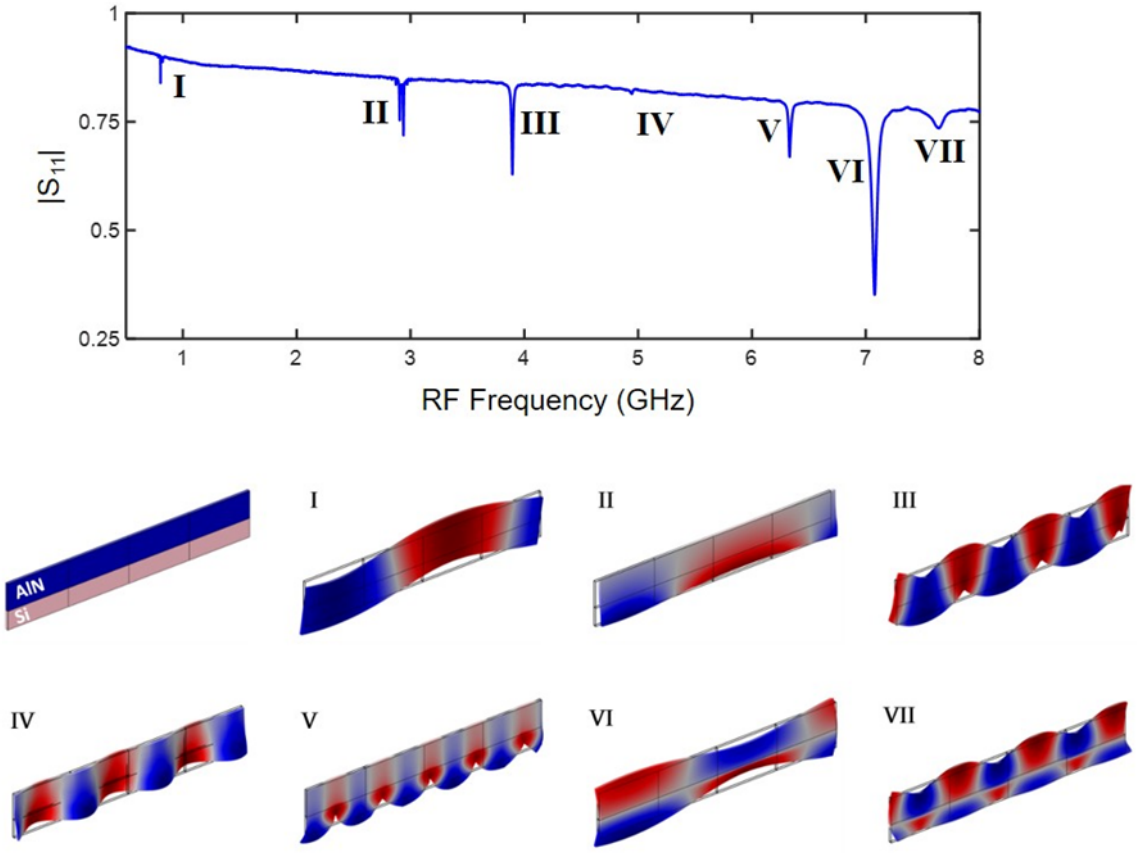

Figure 3.3: **Spectrum of the mechanical modes in the AlN/Si region when the IDT is driven in the RF frequency range of 500 MHz – 8 GHz.** I-VII show the simulated distributions of the displacement fields in a single IDT period (3 μm), which correspond to the resonance modes in the experimentally measured IDT spectrum, respectively.

. Using Jacobi–Anger expansion

$$\exp[i\beta\sin(\Omega t+\phi)]=\sum_k J_k(\beta)\exp[ik(\Omega t+\phi)] \tag{3.4}$$

, where $J_v(x)$ is the Bessel function of the first kind, we decompose Eq. 2 in Fourier series $\alpha(t)=\sum_k \alpha_k \exp(ik\Omega t)$, and obtain

$$ik\Omega\alpha_k(t)=(i\Delta-\kappa/2)\alpha_k+J_k(\beta)e^{ik\phi}a_{\text{in}} \tag{3.5}$$

, which leads to

$$\alpha_k=e^{ik\phi}J_k(\beta)\frac{a_{\text{in}}\sqrt{\kappa_{\text{ex}}}}{i(-\Delta+k\Omega)+\kappa/2}. \tag{3.6}$$

. The dynamics of the intra-cavity optical field can then be expressed as

$$\begin{aligned} a(t) &= e^{-i\beta\sin(\Omega t+\phi)}\cdot\sum_k \alpha_k\exp(ik\Omega t) \\ &= \sum_n e^{-in\Omega t}\sum_k J_{n+k}(\beta)J_k(\beta)e^{-in\phi}\frac{\sqrt{\kappa_{\text{ex}}}a_{\text{in}}}{i(-\Delta+k\Omega)+\kappa/2} \end{aligned} \tag{3.7}$$

. Thereby, the optical output at the exit facet of the end-coupled optical nanobeam cavity can be explicitly calculated as

$$a_{\text{out}}\,(t)=\sum_n e^{-i(\omega_{\text{p}}+n\Omega)t}\sum_k J_{n+k}(\beta)J_k(\beta)e^{-in\phi}\frac{\kappa_{\text{ex}}a_{\text{in}}}{i(-\Delta+k\Omega)+\kappa/2} \tag{3.8}$$

.

At high modulation index $\beta >> 0$, the Bessel functions $J_v(\beta)$ are non-vanishing for $>> 1$, leading to large amplitudes at higher order harmonic signals. Hence, the output optical signal for a single-frequency input at ω_p can be thought of as a compositional baseband of many RF harmonics modulated by the optical carrier frequency ω_p. In the following, we show our method to experimentally characterize each of the RF harmonics in the optical output.

3.3.3 Experimental characterization of the cavity acousto-optic modulator

We used homodyne and heterodyne measurement schemes to characterize the modulation in terms of the microwave-to-optical transduction signal (S_{OE}) and the harmonic signal generations (Figs. **??** in the main text), respectively. Fig. 3.4 shows the experimental setup.

The integrated interdigital transducer (IDT) was driven by one active port (Port 1) of a calibrated vector network analyzer (VNA) with tunable RF frequency and power output. The optical input was realized by coupling a continuous-wave (CW) laser to the on-chip grating coupler through a polarization-maintained fiber, and the output was collected from the output grating coupler by another aligned fiber. We measure the spectra of the direct-current (DC) transmitted optical power (Fig. 3.1D, Fig. 3.8B and Fig. 3.8C) by switching the optical output from our device to a low-speed photodetector (LPD) while sweeping the laser frequency. The high-frequency components of the transmitted optical signal are interrogated by a square-rule high-speed photodetector (HPD) with a bandwidth of 12 GHz, which down-converts the beating notes of the detected optical signal to corresponding RF voltages.

In the homodyne branch, we switched off the acousto-optic frequency shifter (AOFS) and sent the down-converted signal from the HPD to the passive Port 2 of the VNA. The S_{21} parameter of VNA then measured the HPD-generated RF signal at the driving microwave frequency normalized by the input RF complex amplitude, which is proportional to the first-order optical beating note in $a_{\text{out}} \cdot a^*_{\text{out}}$, where a_{out} is the output field in Eq. (7), i.e.,

$$S_{21} \propto \sum_n a_n \cdot a^*_{n-1}. \tag{3.9}$$

We note it is only possible for this S_{21} to take nonzero value if the electromechanically transduced acoustic wave modulates the optical field. It is therefore also named the microwave-to-optical transduction signal ($S_{OE} = S_{21}$). In most of previous works where the modulation index is small (only a_0, a_1 and a_{-1} are relevant), S_{OE} can be simplified to $S_{\text{OE}} \propto a_0 a^*_{-1} + a_1 a^*_0$, which is widely used as the metric to the modulation depth and bandwidth when the laser frequency is tuned at the red sideband ($\Delta = -\Omega, S_{\text{OE}} \propto a_1$) or the blue sideband ($\Delta = \Omega, S_{\text{OE}} \propto a^*_{-1}$) for sideband-resolved acousto-optic systems. Another functionality of our homodyne measurements is to identify the center optical resonance frequency ω_0 because S_{OE} equals zero at exactly zero detuning $\Delta = 0$ and has a large gradient in the

vicinity. We used the traces of the $|S_{21}|$ center local minimum shown in Fig. 3.5 to characterize the thermo-optic shift induced by the acoustic wave. For our acousto-optic modulator with high modulation index, however, S_{OE} is a complicated composition contributed from all of the induced harmonic signals a_n ($|n| > 1$), and therefore cannot fully characterize the dynamic phase modulation. This necessitates the heterodyne measurements that can spectrally resolve all the harmonic signals received by the HPD.

In the heterodyne branch, we drive the AOFS at an angular frequency $\omega_\mu = (2)\cdot 103$ MHz, which shifts the optical frequency of the local oscillator (LO) to $\omega_\mu + \omega_p$. When combined with the optical output from our acousto-optic modulator, the signal received at the HPD can be written as (by ignoring the high frequency components)

$$U_{\text{hetero}} \propto \left(c_0 e^{-i(\omega_{\text{p}}+\omega_{\text{p}})t} + \sum_n a_n e^{-i(\omega_{\text{p}}+n\Omega)t} \right) \left(c_0 e^{-i(\omega_{\text{p}}+\omega_{\text{p}})t} + \sum_n a_n e^{-i(\omega_{\text{p}}+n\Omega)t} \right)^* \tag{3.10}$$

. The down-converted RF voltage contains the frequency components at $\omega_\mu - n\Omega$ which have the amplitudes proportional to the corresponding n-th harmonic signals in the optical output by a factor of the LO amplitude h_0, i.e.

$$\left| u_{\omega_\mu - n\Omega} \right| \propto h_0 \left| a_n \right| \tag{3.11}$$

. Therefore, by mapping out all the RF frequency components in a real-time spectrum analyzer (RSA), we can capture all the amplitudes of the harmonic generations induced by the acousto-optic modulation. The heterodyne measurements were used to obtain the experimental results in Figs. 3.8D, E, Fig. 3.9 and Fig. 3.11.

3.3.4 RF spectra of the microwave-to-optical transduction.

We use the homodyne measurements to characterize the spectrum of the acousto-optic modulation and the associated thermo-optic shift for the RF drive at varying RF tone. Fig. 3.5 shows the spectrum of the measured microwave-to-optical transduction signal at the mechanical resonances, including the prominent fundamental Lamb mode and compressional

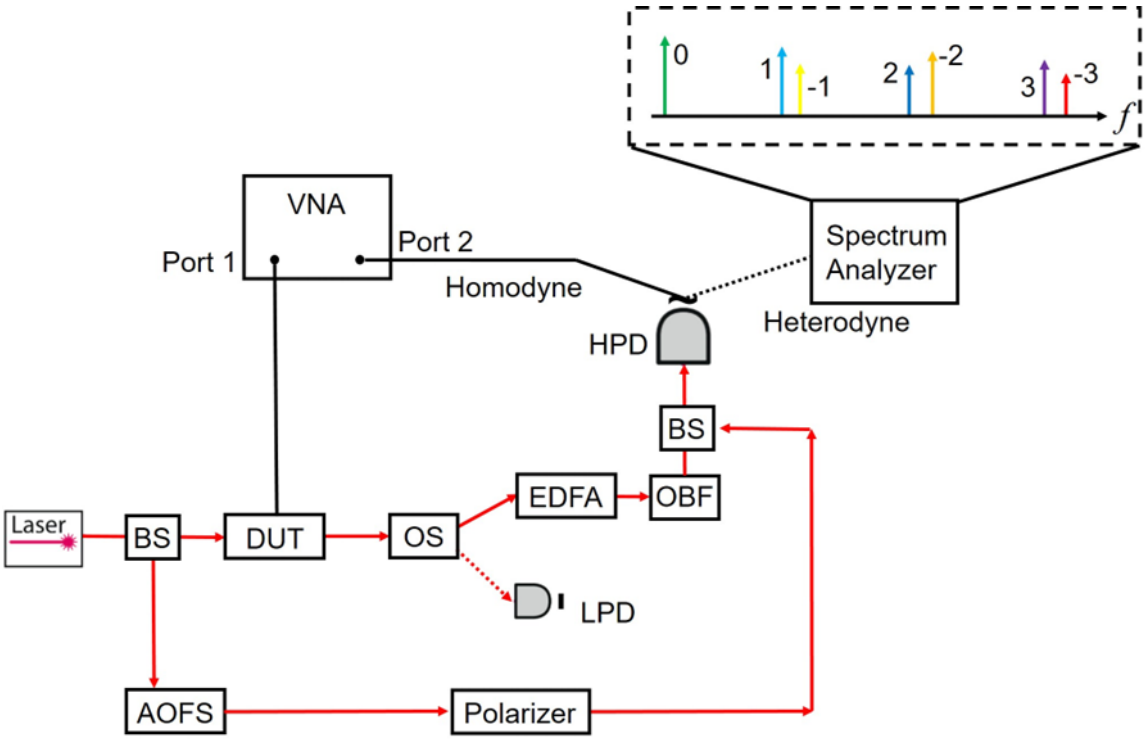
0
1
-1
2
-2
3
-3
f
VNA
Port 1
Port 2
Homodyne
Spectrum
Analyzer
Heterodyne
HPD
BS
EDFA
OBF
Laser
BS
DUT
OS
LPD
AOFS
Polarizer

Figure 3.4: **Experimental setup for the homodyne/heterodyne measurements.** BS: optical in-line beam splitter; DUT: device under test; AOFS: fiber acousto-optic frequency shifter; OS: optical switch; LPD: low-speed photodetector; EDFA: erbium-doped fiber amplifier; OBF: tunable optical bandpass filter; HPD: high-speed photodetector (12-GHz bandwidth); VNA: vector network analyzer.

mode. The acoustic resonator formed by the free-edge reflector gives rise to a series of resonances in the IDT bandwidth. By mapping out the RF spectrum of S_{OE}, we were able to identify the on-resonance microwave tones that can induce the most efficient modulation for each mechanical mode. The laser frequency is swept around the intrinsic nanophotonic cavity resonance to probe S_{OE} at all sidebands.

For the fundamental Lamb mode excitation at 800 MHz, we observed the appearance of S_{OE} at multiple resolved sidebands even at a low RF power of -16dBm. In particular, the 803 MHz drive with an RF bandwidth of 1.3 MHz induces a significantly increased number of sidebands, consistent with the most pronounced electromechanical conversion efficiency measured from S11. This RF tone thus facilitates the resonantly enhanced acousto-optic modulation, by which we demonstrated the scalable MVM at a large-scale synthetic frequency lattice. The minimum at zero laser frequency detuning indicates a constant optical center resonance frequency (no pronounced thermo-optic shift) at the -16 dBm RF power (Fig. 3.5A). For the fundamental compressional mode excitation at 2.9 GHz, the highest modulation efficiency is achieved at 2.903 GHz, where the optical mode overlaps with the anti-node of the acoustic resonator. The 2.935 GHz resonance has a weaker modulation because the optical mode primarily overlaps with the node of the mechanical standing wave. The acoustic resonances in this frequency range are subject to more mechanical power dissipation, evidenced by the increased linewidth of 7.5 MHz. As a result, a substantial red shift of the optical center resonance frequency can be observed at the RF power of -6 dBm, shown by the trace of the local minimum in the middle of Fig. 3.5B. As mentioned in Section 2, other higher-order mechanical modes have much reduced modulation efficiency. As an example, we show the spectrum of S_{OE} for the 5th-order compressional mode in Fig. 3.5D, which is barely measurable even at the RF power of 0 dBm. We remark that the excitations of higher-order mechanical modes, while contributing negligibly to the dynamic phase modulation, can function as thermo-optic resonance tuning, beneficial for aligning the operation frequencies in concatenated modulator networks.

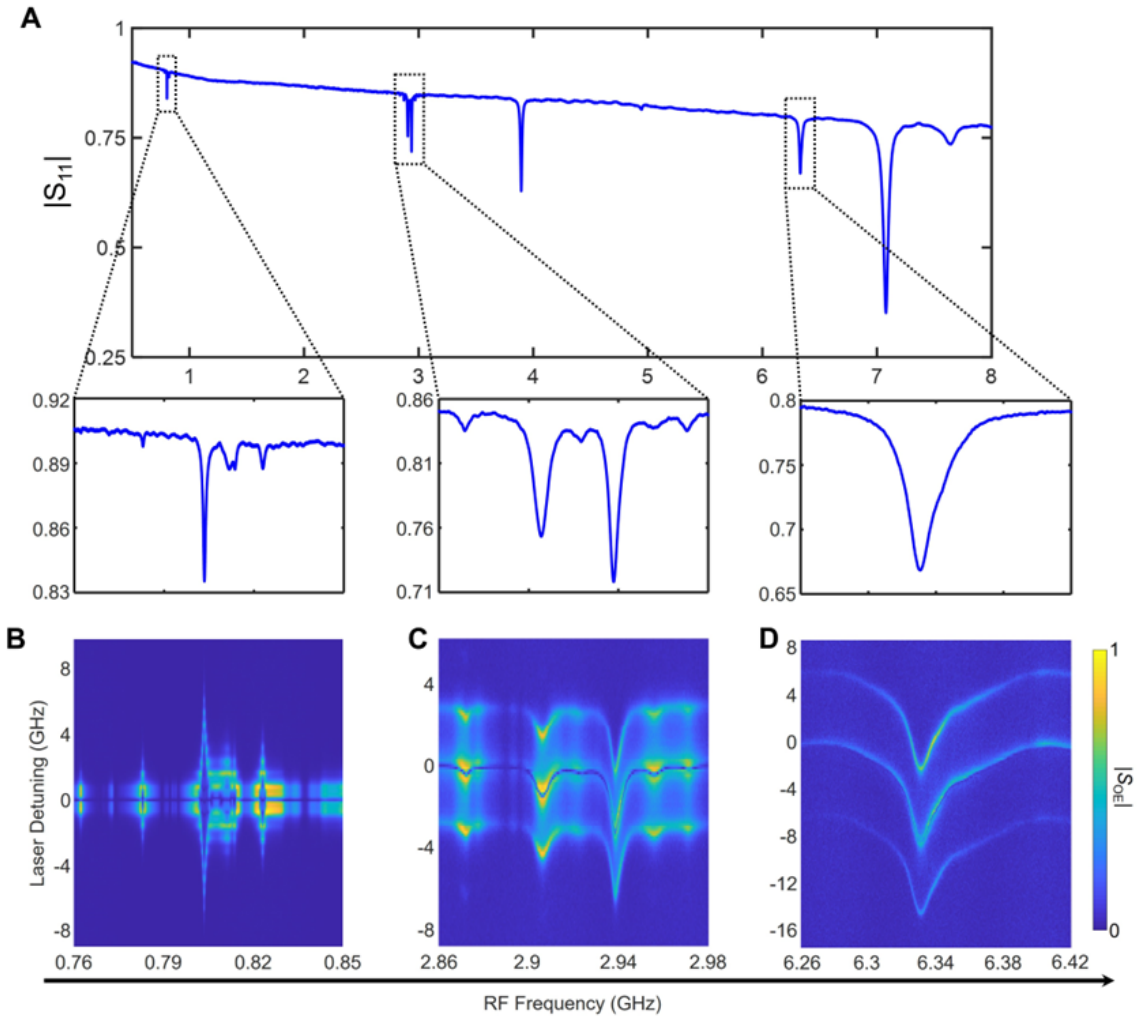

Figure 3.5: **Characterizations of the microwave-to-optical transduction.** a. RF spectrum of the IDT reflection coefficient $|S_{11}|$. The zoom-in reflection spectra correspond to the excitations of the fundamental Lamb mode, fundamental compressional mode and 5th-order compressional mode, respectively. b. Amplitude of S_{OE} as a function of the RF driving frequency and the laser detuning for the fundamental Lamb mode. The RF power is fixed at -16 dBm. c. Amplitude of S_{OE} for the fundamental compressional mode at the RF power of -6 dBm. d. Amplitude of S_{OE} for the 5th-order compressional mode at the RF power of 0 dBm.

3.4 Coherent frequency conversions in the synthetic frequency dimension

3.4.1 Optical spectra of the high-order harmonic signal generations.

We used the heterodyne measurement setup to characterize all the harmonic signal generations whose amplitudes are proportional to the corresponding frequency components in the converted RF voltage at the HPD. The theoretical results of the n-th harmonic amplitude is

$$|a_n| = \sum_k J_{n+k}(\beta) J_k(\beta) \frac{\kappa_{\text{ex}} a_{\text{in}}}{i(-\Delta + k\Omega) + \kappa/2} \tag{3.12}$$

. As we show in Eq. (10), the n-th harmonic amplitudes can be experimentally characterized by measuring the heterodyne beating note at the frequency $\omega_\mu - n\Omega$ (with a factor determined by the LO intensity). To reveal the accuracy of our heterodyne characterizations, we show in Fig. 3.6 the agreement of the measured spectrum of the first-order beating note with the theoretical result by Eq. (12), where $\Omega = 2.903$ MHz and the RF power is -2.5 dBm ($\beta = 1.29$).

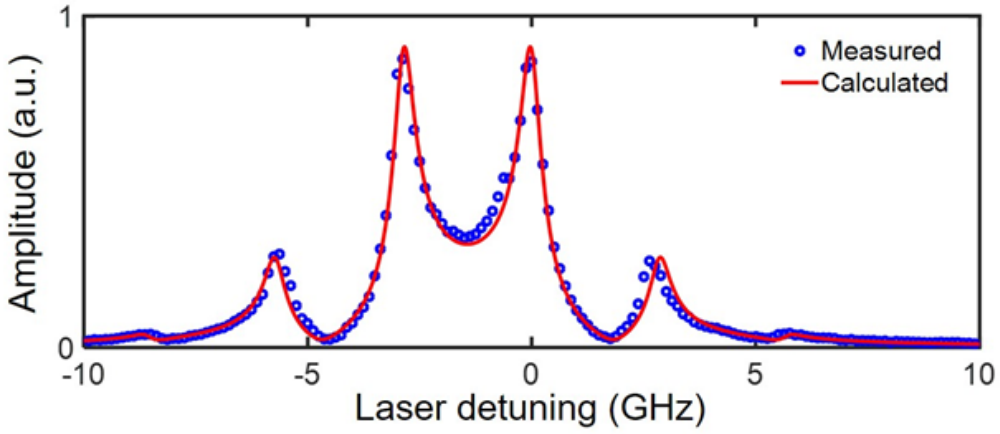

Figure 3.6: **Normalized optical spectrum of the first-order beating note obtained at $\Omega = 2.903$ GHz and -2.5 dBm RF power ($\beta = 1.29$).**

The characterization scheme also works for large modulation indices observed at $\Omega = 803$

MHz. Within our HPD bandwidth (12 GHz), we show in Fig. 3.7 the examples of the fit to demonstrate that all the substantial harmonic signals can be read out with high fidelity ($\beta = 6.90$).

3.4.2 Coherent matrix-vector multiplication

The centerpiece of performing fully connected MVM with our modulator is the coherent conversions from each input frequency site to all the sites at the output. To understand this, we consider a monochromatic laser input and an RF drive with a single microwave tone $\hat{f}(t) = \cos(\Omega t + \phi)$. At a large β, the incident photons can absorb or emit multiple phonons because of the strong optomechanical coupling. Consequently, the input optical field is scattered to a set of harmonic signals $\{a_l\}$ detuned from the cavity center frequency by $\Delta + l\Omega$, where l is the harmonic order. By solving Eq. (1), it can be derived that

$$a_l = \sum_k J_{l+k}(\beta) J_k(\beta) e^{-in\phi} \frac{\kappa_{\mathrm{ex}} a_{\mathrm{in}}}{i(-\Delta + k\Omega) + \kappa/2} \tag{3.13}$$

, where $J_v(x)$ is the v-th order Bessel function of the first kind. We perform heterodyne measurements to characterize the amplitudes of all the harmonic signals with varying input laser frequency. Fig. 3.8d and Fig. 3.8e show the exemplary optical spectra of the harmonics measured at the RF drives of 2.903 GHz and 803 MHz, respectively, highly consistent with the theoretical values. When the input laser frequency is set on the n-th synthetic lattice sites, i.e., detuned by $\Delta = n\Omega$, each a_l leads to a non-local frequency conversion from the n-th site to the m-th site, where $m = n + l$. Hence, the entire set of harmonic generations at all sidebands constitute a two-dimensional optomechanical coupling tensor

$$\mathbf{G} = [g_{mn}], m, n \in [-M, M] : g_{mn} = a_{m-n}/a_{\mathrm{in}} \tag{3.14}$$

, where $2M + 1$ is the size of the synthetic lattice determined by the modulation index β. More generally, for an optical input vector on the synthetic lattice $\mathbf{x} = (x_{-M}, \ldots, x_0, \ldots, x_M)^{\mathrm{T}}$, our modulator performs a complex-valued MVM $\mathbf{y} = \mathbf{G} \cdot \mathbf{x}$, yielding an output vector $\mathbf{y} = (y_{-M}, \ldots y_0, \ldots, y_M)^{\mathrm{T}}$. We highlight that, with $\beta_{\max} = 22.9$, a single such modulator

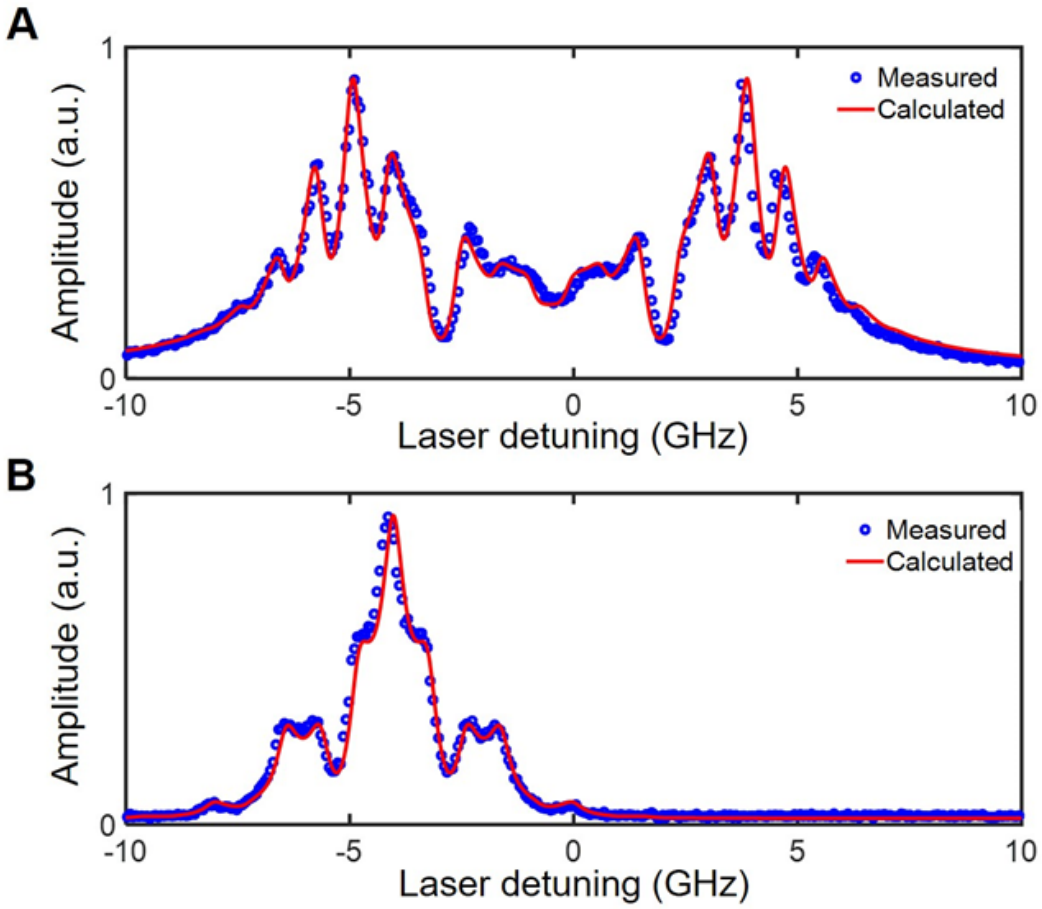

Figure 3.7: **Normalized optical spectra of the beating note obtained at Ω = 803 MHz and -17 dBm RF power (β = 6.90).** a. First-order beating note. b. $10th$-order beating note.

provides an MVM unit with a scalable size of up to 50×50 in the frequency domain.

Large-scale coherent MVM operations. In addition to the high scalability, another outstanding advantage of the frequency-domain MVM is the persistent phase coherence across the entire synthetic lattice. In contrast to conventional spatial-domain schemes, which are susceptible to various causes of decoherence such as device defects, non-uniformity and thermal fluctuations, the phase information transmitted through the synthetic lattice is intrinsically preserved by the coherent photon-phonon interactions in our modulator. To demonstrate the scalable and coherent MVM, we operate our device using the $\Omega = 803$MHz drive and set $\beta = 11.3$, which generates a 25×25 matrix $\mathbf{G}$ according to Eq. (3). A Mach-Zehnder intensity modulator $\mathbf{M_I}$ is used to synthesize a vector input of three coherent frequency components, including the carrier transmission and the two opposite-sign sideband signals with their complex amplitudes controlled by a DC bias and an RF drive at Ω, respectively. For simplicity, we tune the temporal delay of the modulations to be zero ($\phi = 0$). The output on the synthetic frequency lattice is thereby a result of the weighted complex-number summation of the corresponding columns in $\mathbf{G}$, representing the coherent MVM operation.

For the first MVM experiment, we set the laser frequency at the center optical resonance ($\Delta = 0$), and remove the carrier transmission, thus providing an input vector $\mathbf{x} = (\ldots, 0, x_{-1}, 0, x_1, 0, \ldots)^{\mathrm{T}}$ where $x_{-1} = -x_1$ (Fig. 3.9a). These two input components couple to the 25 sites on the synthetic lattice through the non-local frequency conversions, which add up to a symmetric amplitude distribution at the output (Fig. 3.9b). Next, we tune the DC bias to generate an input $\mathbf{x} = (\ldots, 0, x_{-1}, x_0, x_1, 0, \ldots)^{\mathrm{T}}$, where $|x_0| = |x_1|$ and $\arg(x_0) = -\arcsin(x_1/a_{\mathrm{in}})$ (Fig. 3.9c). Such additional component x_0 is also coherently scattered to the entire frequency lattice and induces the interference with the pattern formed by $x_{\pm 1}$, leading to an asymmetry in Fig. 3.9d. To demonstrate the coherence of the full range "edge-to-edge" connections, we then align the laser frequency to the 9th site ($\Delta = 9\Omega$), and set $\mathbf{M_I}$ to produce an input $\mathbf{x} = (\ldots, 0, x_8, x_9, x_{10}, 0, \ldots)^{\mathrm{T}}$ with $|x_8| = |x_9| = |x_{10}|$. The DC bias on $\mathbf{M_I}$ is switched between the phase relation of either $\arg(x_9) = \arcsin(x_{10}/a_{\mathrm{in}})$ (Fig. 3.9e) or $\arg(x_9) = -\arcsin(x_{10}/a_{\mathrm{in}})$ (Fig. 3.9g). From

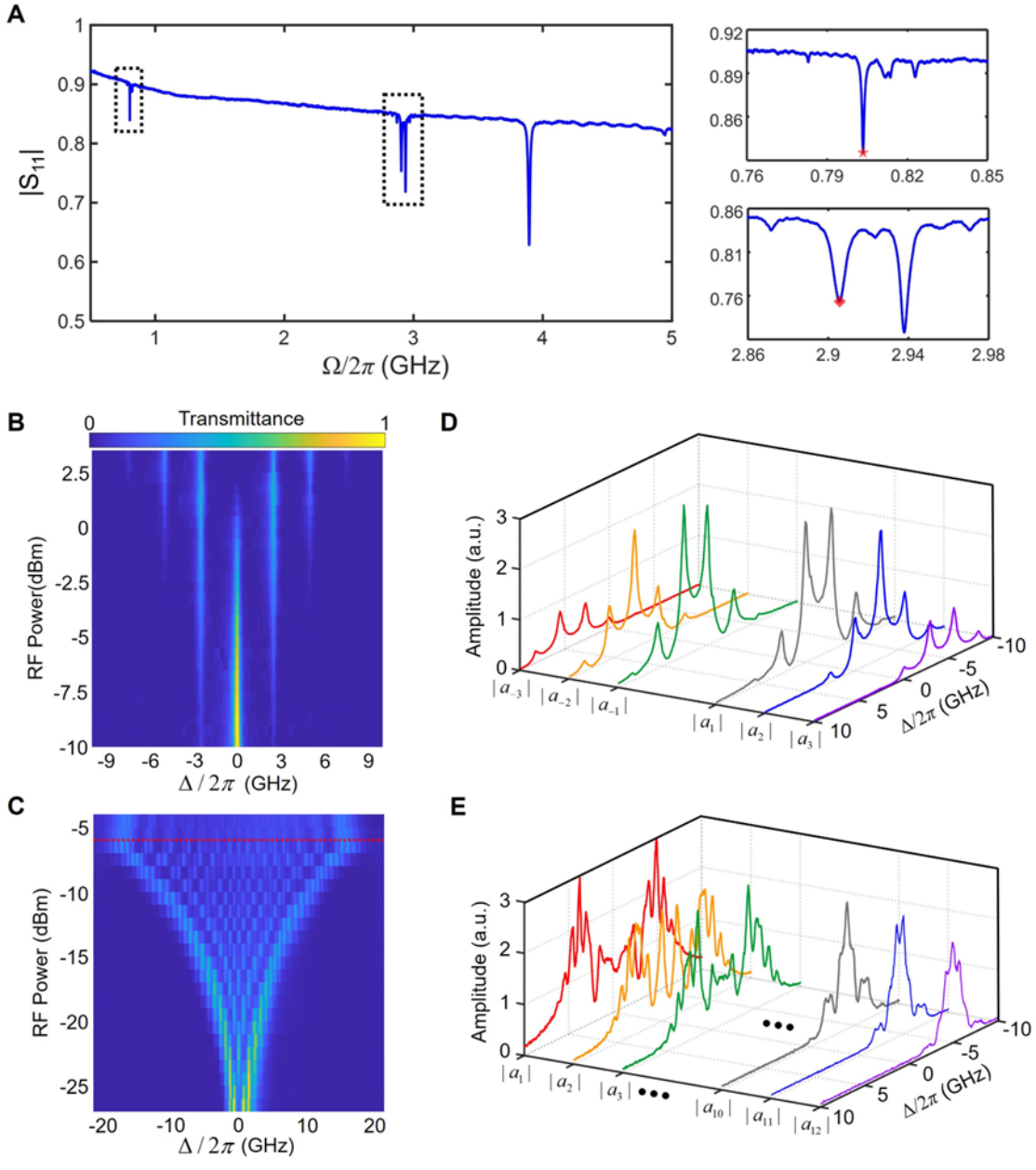
A
|S11|
Ω/2π (GHz)
B
Transmittance
RF Power(dBm)
Δ / 2π (GHz)
C
RF Power (dBm)
Δ / 2π (GHz)
D
Amplitude (a.u.)
Δ/2π (GHz)
E
Amplitude (a.u.)
Δ/2π (GHz)

Figure 3.8: **Characterizations of the acousto-optic modulation efficiency and the harmonic signal generations.** a. Reflection (amplitude) spectrum of the IDT. The mechanical resonances in the zoom-in spectra at $\sim$ 800MHz and $\sim$ 2.90GHz have pronounced modulation efficiency, whereas the resonance at 3.95 GHz has a negligibly weak modulation effect. The star and diamond marks denote the prominent frequencies (803 MHz and 2.903 GHz) with enhanced modulation efficiencies for the corresponding mechanical modes. b. Optical transmission spectra under the modulation driven at 2.903 GHz with varying RF power from -10 dBm to 3 dBm. c. Optical transmission spectra under the modulation driven at 803 MHz with RF power from -27 dBm to -5 dBm. The red dashed line denotes the threshold of an electromechanical nonlinearity above which the number of sidebands ceases increasing. d. Measured optical spectra of the non-vanishing harmonic signal amplitudes $|a_l|\,(l = \pm 1, \pm 2, \pm 3)$ at 2.903 GHz, -2.5 dBm RF drive ($\beta = 1.29$). e. Spectra of the positive-order harmonic signal amplitudes $|a_l|\,(l = 1, 2, 3, \ldots, 10, 11, 12)$ at 803 MHz, -17 dBm RF drive ($\beta = 6.90$). The higher-order harmonics decrease significantly beyond $l = 12$ at this drive. The corresponding spectra of the negative-order harmonics (not plotted) are mirror-symmetric about $\Delta = 0$.

the measured output amplitude patterns, we observe the suppression (Fig. 3.9f) and revival (Fig. 3.9h) of the negative-order sites near the opposite edge by only phase-flipping of the carrier transmission, a strong indicator of the built-in long-range phase coherence with the frequency-domain MVM operations.

3.4.3 Measuring the output of the MVM operations on the synthetic frequency lattice.

The output amplitude at each frequency site, resulted from the MVM operations (Fig. 3.9 in the main text), was interrogated by the heterodyne measurements as we have described in Section 4. The experimental setup for the large-scale MVM operations is shown in Fig. 3.10. The LO frequency $\omega_p + \omega_\mu$ is controlled by the tunable CW laser. When ω_p is set at one of the frequency sites ($\Delta = s\Omega$), the amplitude of the harmonic signal $|a_l|$ captured by the spectrum analyzer then corresponds to the amplitude at the synthetic lattice site of the order $s+l$. Therefore, we read out the output amplitudes at the synthetic frequency lattice by measuring all non-vanishing harmonic signals. We note, with a photodetector bandwidth of 12 GHz, we were able to fully interrogate up to $15th$-order harmonic signals with high fidelity. The harmonic signals at even higher order are subject to decreased detection efficiencies, which set an upper bound for the size of the synthetic lattice in our experimental demonstrations. By using a photodetector with higher bandwidth (> 40 GHz), our system can experimentally realize coherent 50×50 MVM operations with high-fidelity readout.

3.5 Cascaded modulator networks

Practical optical computations using integrated photonics require programmability with a high degree of freedom to allow on-chip optimization processes such as backpropagation training in a neural network. For the frequency-domain computing architecture, a straightforward approach to increase independently tunable parameters is to concatenate multiple modulators controlled by separate electronics. To this end, we notice the general phase modulations in the full parametric space, including the broadband elements, constitute a non-abelian (noncommutative) group $< G, \cdot >$, where the cascading of modulators defines

the binary operation " $< \cdot >$ " with the matrix-matrix multiplication. The noncommutativity can manifest as nonreciprocal frequency conversions resulted from the coupling phase anisotropy and the non-unitarity. To demonstrate the feasibility of the concatenation architecture, we implement two elements of the group $\mathbf{G}, \mathbf{M} \in < G, \cdot >$ with our device and a broadband electro-optic modulator (EOM), driven by the same microwave tone. We cascade them in both $\mathbf{G} \cdot \mathbf{M}$ (Fig. 3.11a) and $\mathbf{M} \cdot \mathbf{G}$ (Fig. 3.11b) orders and probe the responses with a laser frequency $\Delta = 0$. Since broadband EOMs typically have a low modulation efficiency with V_π at a few volts, we choose the RF drive at 2.903 GHz and add a 20-dB amplifier to the driving arm of the EOM to reach comparable modulation indices. In this scheme, the RF driving phases at both $\mathbf{G}$ and $\mathbf{M}$ count as independently programmable parameters in addition to the modulation depth. To reflect this increased programmability, we use a tunable RF phase shifter which controls the temporal delay between the two modulations. Fig. 3.11c compares the measured output amplitudes for both the concatenation orders with varying modulation phase delay. The contrast of the results clearly shows the driving phase control of the noncommutative frequency conversions, featuring the non-abelian algebraic structure.

3.6 Conclusion

In conclusion, we have demonstrated an ultra-efficient nanophotonic acousto-optic modulator on the hybrid AlN-on-SOI platform that performs large-scale, complex-valued MVM in a fully connected fashion. We reveal the advantages of high scalability and long-range phase coherence associated with the MVM in the synthetic frequency dimension. Further considerations on the engineering of the electromechanical transducer will allow the generation of multiple harmonic tones at $n\Omega$ [123, 124], which facilitates more hardware-efficient realizations towards arbitrary MVM operations. Our demonstrations open the door to a disruptively new silicon-based optical computing architecture that is scalable with significantly increased operand vector length in compact footprints. Such frequency-domain scheme also extends naturally to scalable quantum computing by incorporating optical quantum sources such as single-photon parametric down-conversion, spontaneous four-wave mixing [125,126],

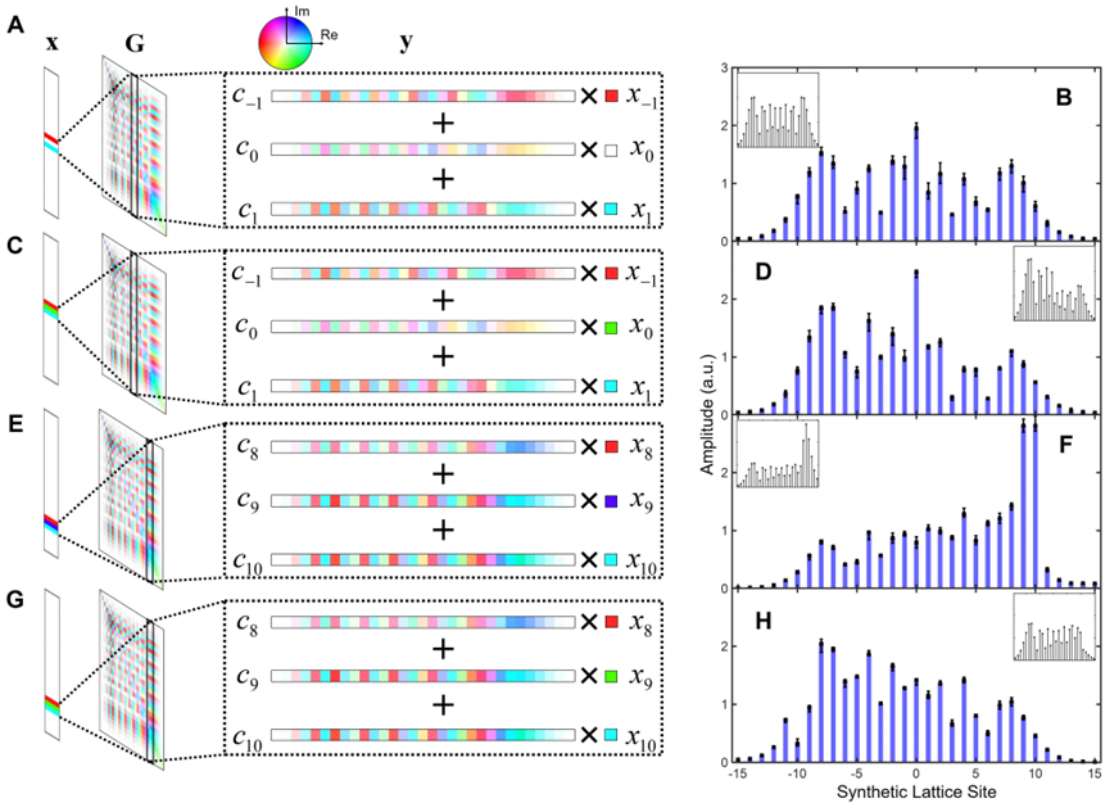
A
x
G
Im
Re
y
C
E
G
B
D
F
H
Amplitude (a.u.)
Synthetic Lattice Site

Figure 3.9: **Large-scale coherent matrix-vector multiplications in the synthetic frequency dimension.** The large matrix G is configured by driving our acousto-optic modulator at 803 MHz with -13 dBm power ($\beta = 11.3$). The vector input $\mathbf{x}$ of three coherent frequency components is synthesized and controlled by an intensity modulator $\mathbf{M}$. a. MVM with laser frequency at the 0_th synthetic lattice site ($\Delta = 0$) and $\mathbf{M}$ set at suppressed carrier transmission. c. $\Delta = 0$ and MI set with three equal-amplitude components and a negative phase on the carrier transmission. e. and f. $\Delta = 9\Omega$ and $\mathbf{M}$ set with three equal-amplitude components and positive/negative phases on the carrier transmission. b., d., f., h. Measured output amplitudes on the synthetic lattice from the settings in a., c., e. and g., respectively. c_j represents the j_{th} column of $\mathbf{G}$, and x_k denotes the input at the k_{th} lattice site. Error bars are calculated from 5 measurements. Insets in b., d., f. and h. are the corresponding results from the theoretical calculations. The discrepancies between the measurements and the theory primarily come from the background transmission of the optical cavity, which is not included in the theoretical model.

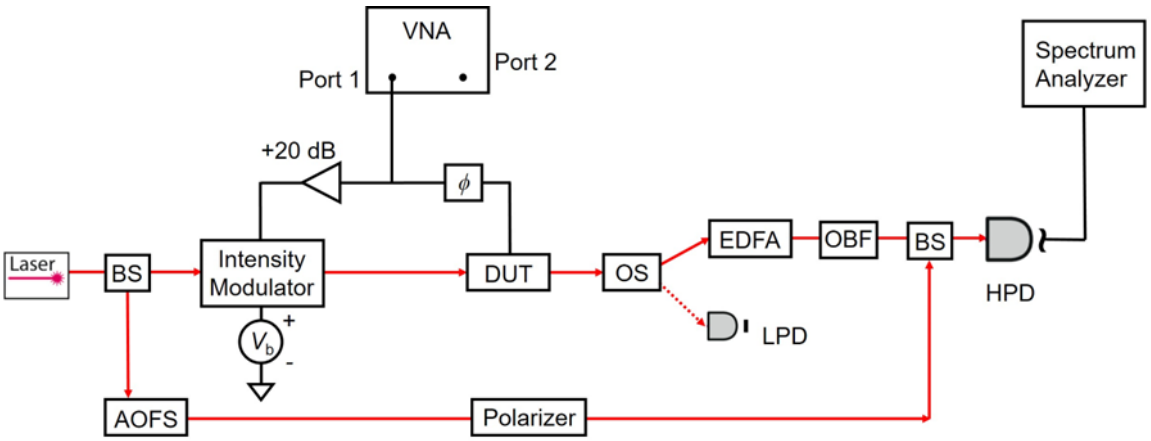

Figure 3.10: **Experimental setup of the large-scale MVM. The intensity modulator, which is driven by the VNA and a DC bias Vb, is cascaded before our device to provide a vector input of three spectrally coherent components.** The RF phase shifter, ϕ, is used to tune the modulation phase difference between the intensity modulator and our device, which can be monitored by the transmittance spectrum measurements by the LPD. An RF amplifier of 20-dB gain is applied to drive the intensity modulator in order to obtain pronounced sideband input frequency components for our device.

and microwave qubit transduction [31], where the efficient dynamic modulators facilitate frequency-bin logic gates for high-dimensional photonic qudits [127].

3.7 Appendix

3.7.1 Experimental Characterizations

We used homodyne and heterodyne measurements to characterize the modulation in terms of the microwave-to-optical transduction signal and the harmonic signal generations, respectively. The optical input with tunable frequency was provided by coupling a continuous-wave laser (TSL-710; Santec) to the on-chip input grating coupler. The IDT was driven by the transmitter port (Port 1) of a calibrated vector network analyzer (E8362B; Agilent) with tunable RF frequency and power. The optical output of the device was collected from the output grating coupler, which was subsequently sent to a 2×2 optical switch (OSW22-633E; Thorlabs) with one port connected to a low-speed photodetector (2053-FC; Newport) for the direct-current (DC) transmission measurements, and the other to a serial connections of erbium-doped fiber amplifier (PM-LNHPFA-15; PriTel), tunable optical bandpass filter (OTF-910; Santec) and high-speed photodetector (1544-B; Newport) for the characterizations of the frequency conversions. In the homodyne measurements, the down-converted signal from the high-speed photodetector was sent to the receiver port (Port 2) of the vector network analyzer. The S21 trace then measured the spectrum of the microwave-to-optical transduction signal corresponding to the generated first-order beating note in the detected optical output. We used the spectrum of S21 to identify the mechanical resonance frequencies with enhanced modulation efficiencies. For the heterodyne measurements, the laser beam was split by a 10/90 benchtop optic coupler, in which the 90 part was used as a local oscillator (LO). The LO was sent through an acousto-optic frequency shifter (TEM-110-10-55-2FP; Brimrose) and up-shifted by 102.9 MHz. The LO was combined with the optical output from our device at a 50/50 benchtop optic coupler, generating a set of spectrally resolved beating notes proportional to the modulation-induced harmonic signals, respectively. We measured the amplitudes of these harmonic signals by a real-time spectrum analyzer

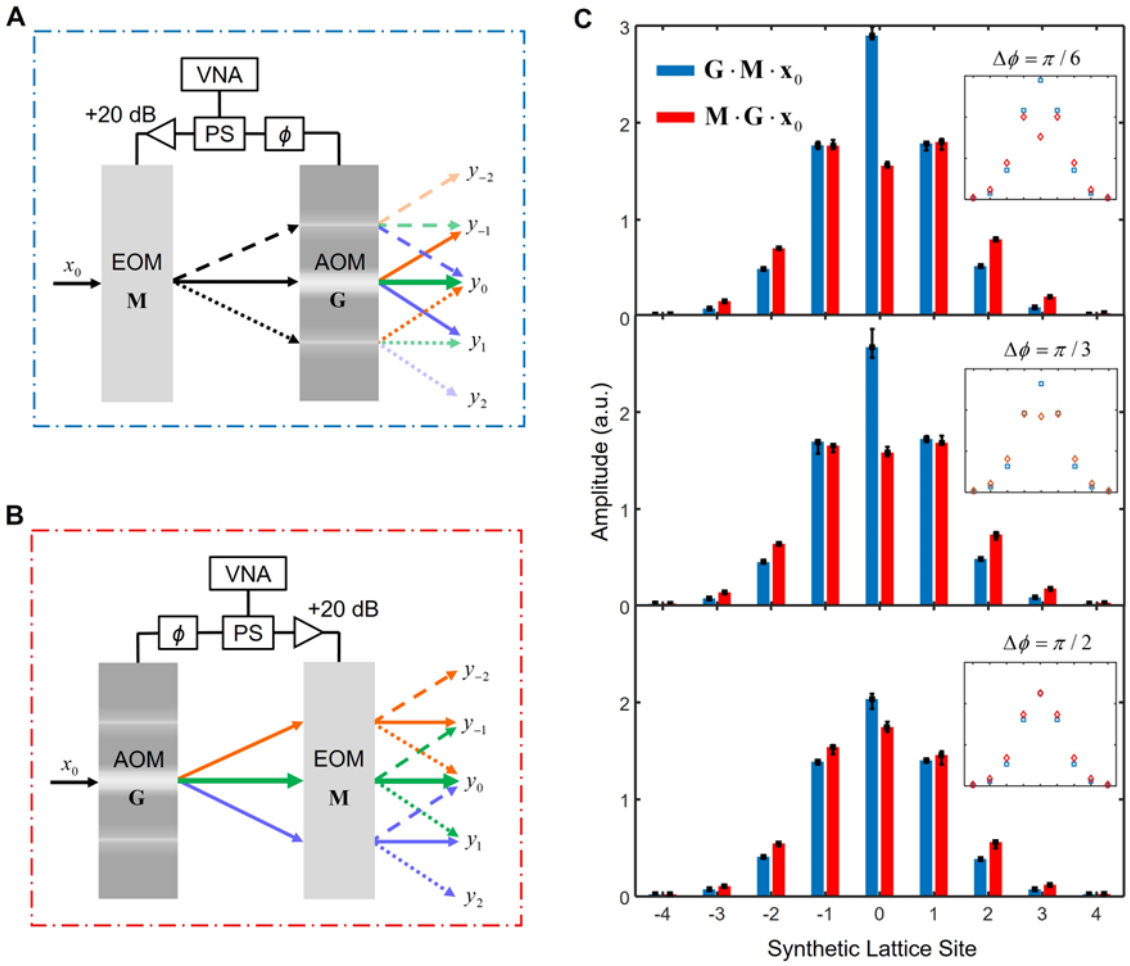
A
VNA
+20 dB
PS
ϕ
x0
EOM
M
AOM
G
y-2
y-1
y0
y1
y2
B
VNA
ϕ
PS
+20 dB
x0
AOM
G
EOM
M
y-2
y-1
y0
y1
y2
C
G · M · x0
M · G · x0
Δϕ = π / 6
Δϕ = π / 3
Δϕ = π / 2
Amplitude (a.u.)
Synthetic Lattice Site
-4
-3
-2
-1
0
1
2
3
4

Figure 3.11: **Large-scale coherent matrix-vector multiplications in the synthetic frequency dimension.** Concatenations of phase modulators. a. Setup of concatenated broadband electro-optic phase modulator (EOM, $\mathbf{M}$) and our acousto-optic modulator (AOM, $\mathbf{G}$) driven by the same vector network analyzer (VNA). A laser input at $\Delta = 0$ (x_0) goes through the EOM first and then the AOM, corresponding to $\mathbf{G} \cdot \mathbf{M} \cdot \mathbf{x}_0$. b. Setup of the concatenation in the reverse order, $\mathbf{M} \cdot \mathbf{G} \cdot \mathbf{x}_0$. Orange, green and blue lines represent the $-1st$, $0th$ (carrier) and $1st$ harmonic signals generated by the AOM, respectively. Higher-order harmonics are neglected for the illustration. Solid, dotted and dashed lines represent the carrier and $\pm 1st$ sideband signals by the EOM. y_k denotes the output of the k-th synthetic lattice sites. PS: RF power splitter; +20 dB: RF amplifier with 20 dB gain; ϕ: RF phase shifter. c. Contrast of the output between the two concatenation orders with varying phase delay $\Delta\phi$ at the two modulations. Error bars are plotted from 5 measurements. Insets are the corresponding results from the theoretical calculations.

(RSA5126B; Tektronix), and read out the results of the matrix-vector multiplications accordingly.

3.7.2 Determining the modulation index from the spectra of optical transmittance.

One of the consequences of the high acousto-optic modulation index is the generation of multiple sidebands in the optical transmission spectrum. In our sideband resolved system, we can extract the modulation index by fitting the measured spectral features of the split sidebands. To see this, here we show the exemplary fitting results under single microwave tone drives at 2.903 GHz and 803 MHz.

The theoretical values of the DC transmittance can be derived from Eq. (7) and takes the form

$$\langle a_{\text{out}} \cdot a_{\text{out}}^{*} \rangle = \sum_{n} \left| J_n(\beta) \frac{\kappa_{\text{ex}}\, a_{\text{in}}}{i(-\Delta + n\Omega) + \kappa/2} \right|^2 \tag{3.15}$$

. We use Eq. (11) to fit the measured spectra of the optical transmittance at varying RF driving power (Figs. 3.8B,C in the main text), where the parameters κ, κ_{ex}, Ω, $a_i n$ were fixed and only the modulation index β is varied to reproduce the spectral features. Fig. 3.12 shows the fit of a transmittance spectrum at $\Omega = 2.903$ GHz and 2 dBm RF power. From the agreement between the measured and calculated spectra, we deduced a modulation index $\beta = 2.15$.

For large modulation depth observed at $\Omega = 803$ MHz, the transmission eigenstate distributes to all of the sidebands spanning a wide spectral range and is superposed by the non-uniform background transmission. Nonetheless, we expect a good characterization of the spectral features by a proper fit parameter β. Fig. 3.13 shows the fit of the measured transmittance spectrum at $\Omega = 803$ MHz and -7 dBm RF power. This corresponds to the maximum modulation index of $\beta = 22.9$ obtained before the onset of electromechanical nonlinearity, where the modulation index ceases to increase proportional to the square-root of the RF power.

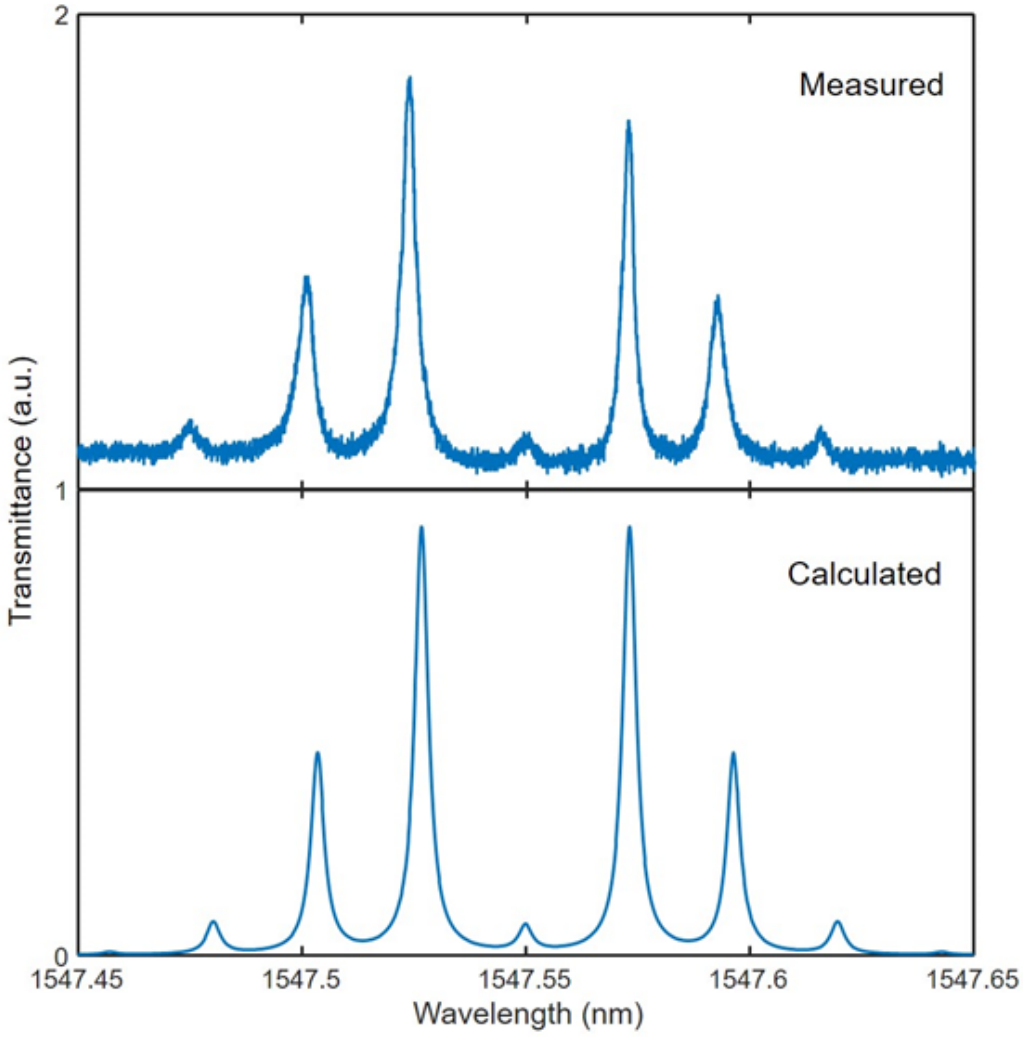

Figure 3.12: **Measured optical transmittance spectrum and the corresponding fit curve with β = 2.15.** The microwave drive is at Ω = 2.903 GHz and 2 dBm RF power (upper). The fit curve is calculated by Eq. (11) (lower). The measured spectrum is shifted up by 1 unit.

3.7.3 Driving phase dependence of the matrix-vector multiplications.

The optomechanical coupling matrix represented by Eq. (3) in the main text has a dependence on the phase of the RF drive applied on the IDT. Fig. 3.14 displaces the theoretically calculated dependence on the modulation phase ϕ when the device is driven at 803 MHz and with $\beta = 11.3$. While this phase variation maintains the amplitudes of the site-to-site couplings ($|g_{mn}|$), a strong phase anisotropy in g_{mn} can be observed, which leads to very different MVM outputs for spectrally coherent vector input. Specifically, for $\phi = 0$, the adjacent columns of $\mathbf{G}$ have minimum phase contrast, while the long-range coupling phases are considerable. Therefore, in our phase-coherent MVM demonstrations (Fig. 3.9 in the main text), we chose to set $\phi = 0$ so as to emphasize the persistence of the phase information of the long-range couplings.

3.7.4 Interrogating the noncommutativity of concatenated modulators.

Fig. 3.15 shows the experimental setups in which we realized the concatenations of our nanophotonic cavity acousto-optic modulator ($\mathbf{G}$) with a fiber-coupled electro-optic phase modulator ($\mathbf{M}$), in both $\boldsymbol{GM}$ and $\boldsymbol{MG}$ orders. We assume that the modulation phases of the RF drives $\mathbf{G}$ and $\mathbf{M}$ are ϕ_1 and ϕ_2, and the optical delay between the two modulators is τ. Under the same RF driving tone Ω, the modulation waveforms for the $\boldsymbol{MG}$ order are

$$\begin{cases} \hat{f}_{\mathrm{M}}(t) = \cos\left(\Omega t + \phi_2\right) \\ \hat{f}_{\mathrm{G}}(t) = \cos\left[\Omega(t+\tau) + \phi_1\right] \end{cases} \tag{3.16}$$

, whereas for the reverse order $\boldsymbol{FM}$, the modulation waveforms are

$$\begin{cases} \hat{f}'_{\mathbf{M}}(t) = \cos\left[\Omega(t+\tau) + \phi'_2\right] \\ \hat{f}'_{\mathrm{G}}(t) = \cos\left(\Omega t + \phi'_1\right) \end{cases} \tag{3.17}$$

. We define the modulation phase differences $\Delta\phi = \arg\left\{\hat{f}_{\mathrm{G}}(t)\right\} - \arg\left\{\hat{f}_{\mathbf{M}}(t)\right\} = \Omega\tau + \phi_1 - \phi_2$ and $\Delta\phi' = \arg\left\{\hat{f}'_{\mathbf{G}}(t)\right\} - \arg\left\{\hat{f}'_{\mathbf{M}}(t)\right\} = \phi'_1 - \phi'_2 - \Omega\tau$. In our experiments, we controlled

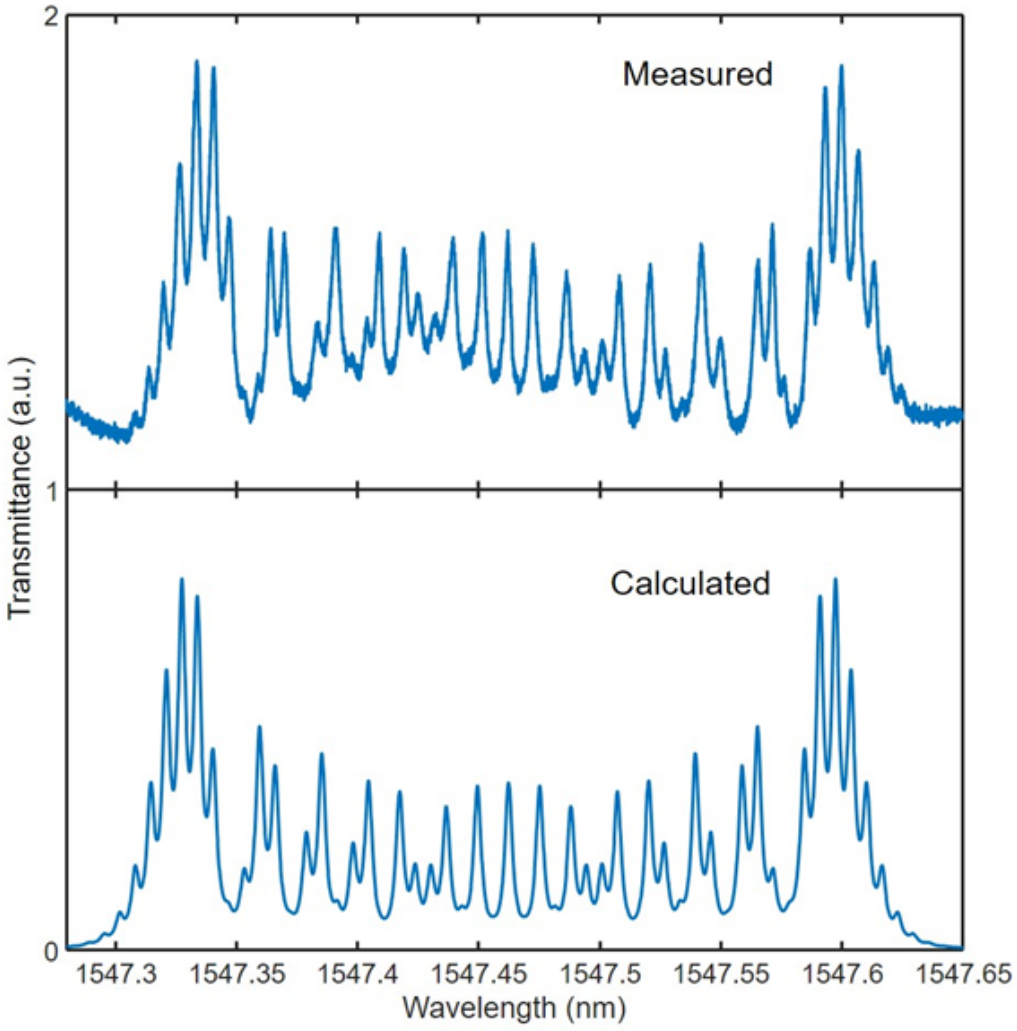

Figure 3.13: **Measured optical transmittance spectrum and the corresponding fit curve with β = 22.9.** The microwave drive is at Ω = 803 MHz and -7 dBm RF power (upper). The fit curve is calculated by Eq. (11) (lower). The measured spectrum is up shifted by 1 unit.

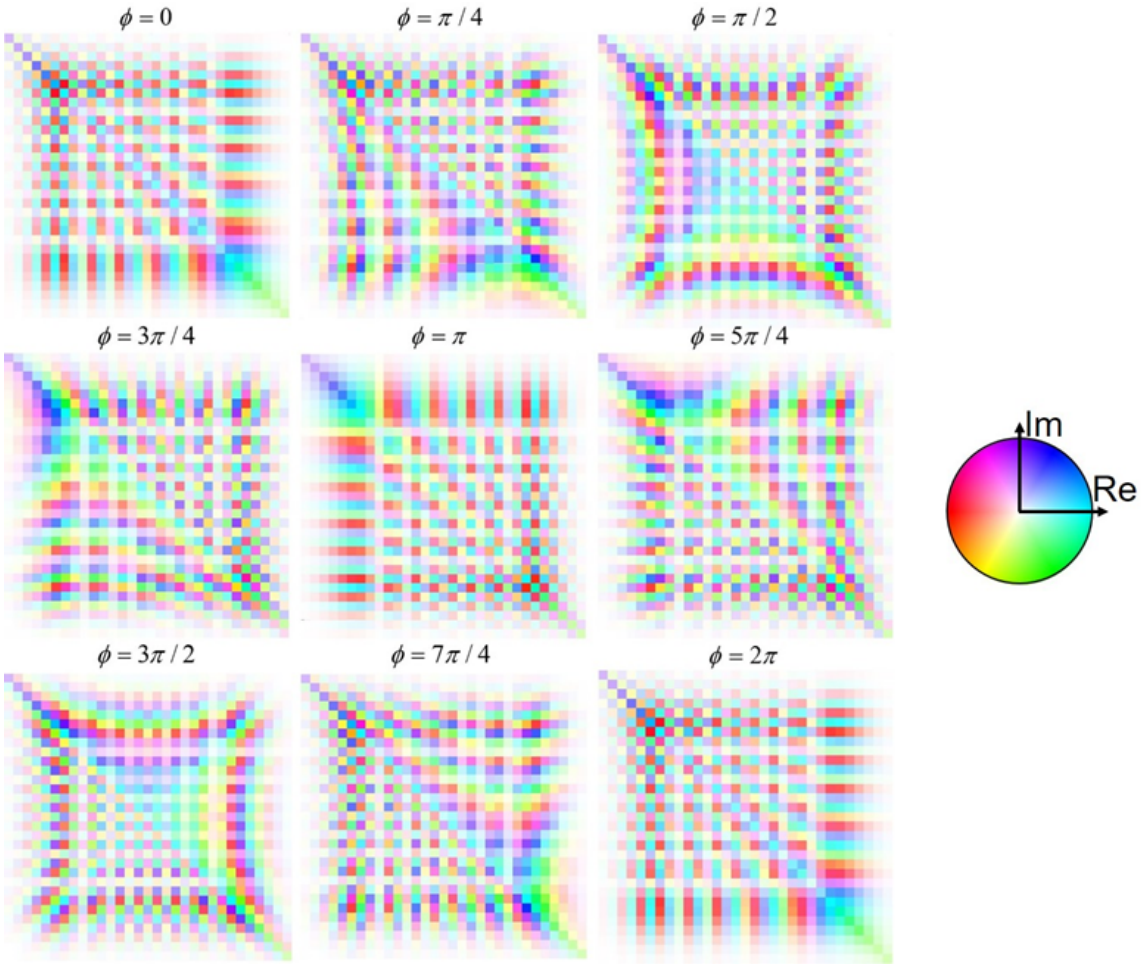

Figure 3.14: **Optomechanical coupling matrices at various microwave driving phase.** The complex-valued matrix entries are represented by the false-color mapping. Matrix dimension is 30×30 at $\Omega = 803$ MHz and $\beta = 11.3$.

$\phi_1 - \phi_2\,(\phi_1' - \phi_2')$ by the RF phase shifter with a tunable phase range $[0, 2\pi]$. We calibrated the optical phase delay τ to unify the two modulation phase differences associated with the two concatenation orders, by comparing the phase dependences of output amplitudes with the theoretical values.

To understand the noncommutativity of the non-abelian group formed by cascaded phase modulators, we analyze the matrix-matrix multiplications between $\mathbf{M} : [m_{kl}]$ and $\mathbf{G} : [g_{kl}]$. The matrix of a broadband modulator is tri-diagonal represented by the carrier transmission on the diagonal entries m_{kk} and the two opposite-sign sideband generations $m_{k(k-1)}$ and $m_{k(k+1)}$ on the off-diagonal entries ($\phi_2 = 0$). The matrix of our acousto-optic modulator is represented by Eq. (3) in the main text. For simplicity of the analytical calculations, we assume a moderate modulation index that only produces 1st order harmonics ($|k–l| < 2$). With a laser input at $\Delta = 0$, the resulted output vector through $y = \boldsymbol{G} \cdot \boldsymbol{M} \cdot \boldsymbol{x_0}$ can be expressed as

$$\begin{aligned} y_{-2} &= m_{-1,0} g_{-2,-1} \\ y_{-1} &= m_{0,0} g_{-1,0} + m_{-1,0} g_{-1,-1} \\ y_0 &= m_{-1,0} g_{0,-1} + m_{0,0} g_{0,0} + m_{1,0} g_{0,1} \\ y_1 &= m_{0,0} g_{1,0} + m_{1,0} g_{1,1} \\ y_2 &= m_{1,0} g_{2,1} \end{aligned} \tag{3.18}$$

. For comparison, the output vector through $y'^{=\boldsymbol{M}\cdot\boldsymbol{G}\cdot\boldsymbol{x_0}}$ is

$$\begin{aligned} y'_{-2} &= m_{-2,-1} g_{-1,0} \\ y'_{-1} &= m_{-1,-1} g_{-1,0} + m_{-1,0} g_{0,0} \\ y'_0 &= m_{0,-1} g_{-1,0} + m_{0,0} g_{0,0} + m_{0,1} g_{1,0}. \\ y'_1 &= m_{1,1} g_{1,0} + m_{1,0} g_{0,0} \\ y'_2 &= m_{2,1} g_{1,0} \end{aligned} \tag{3.19}$$

. Using $m_{b(k+1)} = -m_{b(k-1)} = m, m_{l(l\pm1)} = m_{b(k\pm1)}$ and $m_{kk} = m_{ll}$, we obtain $\boldsymbol{\Delta y} =$

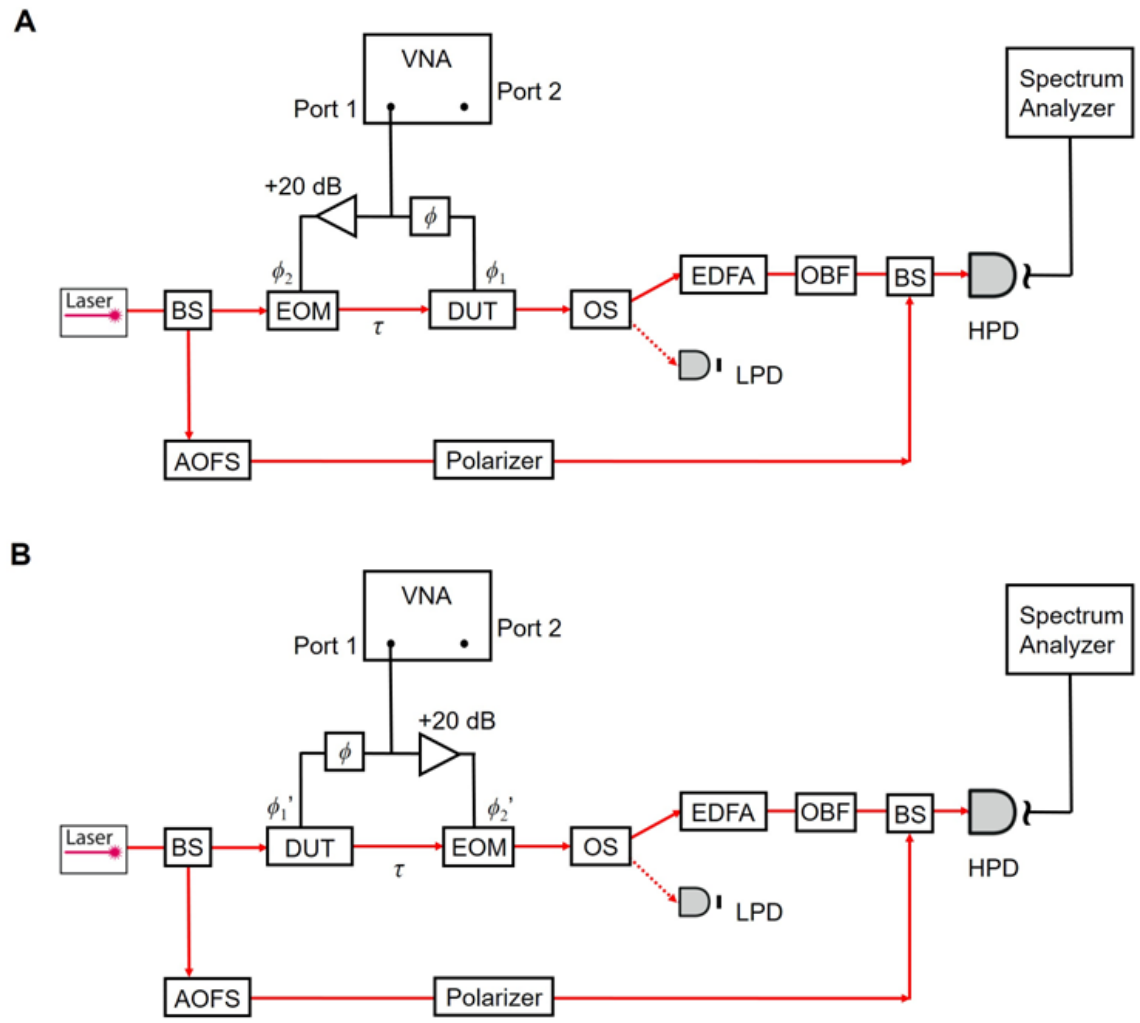

Figure 3.15: **Experimental setup of the large-scale MVM.** The intensity modulator, which is driven by the VNA and a DC bias V_b, is cascaded before our device to provide a vector input of three spectrally coherent components. The RF phase shifter, ϕ, is used to tune the modulation phase difference between the intensity modulator and our device, which can be monitored by the transmittance spectrum measurements by the LPD.

$(\mathbf{G}\cdot\mathbf{M}-\mathbf{M}\cdot\mathbf{G})\cdot\mathbf{x}_0$, where

$$\begin{aligned}
\Delta y_{-2} &= m\left(g_{-2,-1}-g_{-1,0}\right)\\
\Delta y_{-1} &= m\left(g_{-1,-1}-g_{0,0}\right)\\
\Delta y_{0} &= m\left(g_{0,-1}+g_{-1,0}-g_{1,0}-g_{0,1}\right)\\
\Delta y_{1} &= -m\left(g_{1,1}-g_{0,0}\right)\\
\Delta y_{2} &= -m\left(g_{2,1}-g_{1,0}\right)
\end{aligned} \tag{3.20}$$

.

From here, we can attribute the arising of the noncommutativity to two aspects of the optomechanical coupling matrix of our modulator: 1) unlike the broadband EOM, the transmission through the modulated nanophotonic cavity at the center frequency $g_{0,0}$ is significantly different than that from the sidebands ($g_{1,1}$ and $g_{-1,-1}$), i.e. the non-unitarity, associated with the synthetic lattice of our resonating acousto-optic modulator, therefore $\Delta y \pm 1$ are generally nontrivial and are more pronounced at larger transmission difference; 2) as we have explained in Section 8, the two-way frequency conversions between a pair of sidebands (g_k and g_{lk}) are highly phase-anisotropic and have a strong dependence on the driving phase , which result in non-vanishing contrast at the center-frequency component (Δy_0) of the output. While our demonstrations involve a broadband and a resonating phase modulators, we note that these two factors ensure the sufficient and necessary conditions for the noncommutativity of the cascaded phase modulator group with the full parametric space of $(\beta, \Omega, \phi, \omega_0, \boldsymbol{\kappa}, \boldsymbol{\kappa}_{\mathrm{ex}})$.

BIBLIOGRAPHY

[1] Brillouin, L. Diffusion de la lumière et des rayons x par un corps transparent homogène - influence de l'agitation thermique. *Annales de Physique* **9**, 88–122, (1922).

[2] Debye, P. & Sears, F. On the scattering of light by supersonic waves. *PROCEEDINGS OF THE NATIONAL ACADEMY OF SCIENCES OF THE UNITED STATES OF AMERICA* **18**, 409–414, (1932).

[3] Lucas, R. & Biquard, P. Propriétés optiques des milieux solides et liquides soumis aux vibrations élastiques ultra sonores. *Le journal de physique et le radium* **3**, 464–477, (1932).

[4] Raman, C. V. & Nagendra Nath, N. S. The diffraction of light by high frequency sound waves: Part III: Doppler effect and coherence phenomena. *Proceedings of the Indian Academy of Sciences. Section A* **3**, 75–84, (1936).

[5] Born, M. & Wolf, E. *Principles of optics: electromagnetic theory of propagation, interference and diffraction of light* (Elsevier, 2013).

[6] Quate, C., Wilkinson, C. & Winslow, D. Interaction of light and microwave sound. *Proceedings of the IEEE* **53**, 1604–1623, (1965).

[7] Chiao, R. Y., Townes, C. H. & Stoicheff, B. P. Stimulated brillouin scattering and coherent generation of intense hypersonic waves. *Physical review letters* **12**, 592–595, (1964).

[8] Adler, R. Interaction between light and sound". *IEEE spectrum* **4**, 42–54, (1967).

[9] Heiman, D., Hamilton, D. S. & Hellwarth, R. W. Brillouin scattering measurements on optical glasses. *Physical review. B, Condensed matter* **19**, 6583–6592, (1979).

[10] Tsai, C. Integrated acoustooptic circuits and applications. *IEEE transactions on ultrasonics, ferroelectrics, and frequency control* **39**, 529–554, (1992).

[11] Boyd, R. *Nonlinear optics* (Academic Press, 2008), 3rd edn edn.

[12] Garmire, E. Perspectives on stimulated brillouin scattering. *NEW JOURNAL OF PHYSICS* **19**, (2017).

[13] Rakich, P. T., Davids, P. & Wang, Z. Tailoring optical forces in waveguides through radiation pressure and electrostrictive forces. *OPTICS EXPRESS* **18**, 14439–14453, (2010).

[14] Wolff, C., Steel, M. J., Eggleton, B. J. & Poulton, C. G. Stimulated brillouin scattering in integrated photonic waveguides: Forces, scattering mechanisms, and coupled-mode analysis. *PHYSICAL REVIEW A* **92**, (2015).

[15] Van Laer, R., Kuyken, B., Van Thourhout, D. & Baets, R. Interaction between light and highly confined hypersound in a silicon photonic nanowire. *Nature photonics* **9**, 199–203, (2015).

[16] Ippen, E. Low-power quasi-cw raman oscillator. *Applied Physics Letters* **16**, 303–305, (1970).

[17] Shelby, R. M., Levenson, M. D. & Bayer, P. W. Guided acoustic-wave brillouin scattering. *Physical Review B* **31**, 5244–5252, (1985).

[18] Rakich, P. T., Reinke, C., Camacho, R., Davids, P. & Wang, Z. Giant enhancement of stimulated brillouin scattering in the subwavelength limit. *PHYSICAL REVIEW X* **2**, (2012).

[19] Pant, R. *et al.* On-chip stimulated brillouin scattering. *OPTICS EXPRESS* **19**, 8285–8290, (2011).

[20] Beugnot, J.-C. *et al.* Brillouin light scattering from surface acoustic waves in a subwavelength-diameter optical fibre. *Nature Communications* **5**, 5242, (2014).

[21] Kang, M. S., Brenn, A. & Russell, P. S. J. All-optical control of gigahertz acoustic resonances by forward stimulated interpolarization scattering in a photonic crystal fiber. *Physical review letters* **105**, 153901–153901, (2010).

[22] Bahl, G., Tomes, M., Marquardt, F. & Carmon, T. Observation of spontaneous brillouin cooling. *NATURE PHYSICS* **8**, 203–207, (2012).

[23] Kumar, B. *et al.* Renewable and metal-free carbon nanofibre catalysts for carbon dioxide reduction. *NATURE COMMUNICATIONS* **4**, (2013).

[24] Tomes, M. & Carmon, T. Photonic micro-electromechanical systems vibrating at x-band (11-GHz) rates. *PHYSICAL REVIEW LETTERS* **102**, (2009).

[25] Carmon, T., Rokhsari, H., Yang, L., Kippenberg, T. & Vahala, K. Temporal behavior of radiation-pressure-induced vibrations of an optical microcavity phonon mode. *PHYSICAL REVIEW LETTERS* **94**, (2005).

[26] Safavi-Naeini, A. H., Van Thourhout, D., Baets, R. & Van Laer, R. Controlling phonons and photons at the wavelength scale: integrated photonics meets integrated phononics. *OPTICA* **6**, 213–232, (2019).

[27] Campbell, C. *Surface acoustic wave devices for mobile and wireless communications* (Academic Press, 1998).

[28] Morgan, D. P. *Surface acoustic wave filters with applications to electronic communications and signal processing.* Studies in Electrical and Electronic Engineering (Academic Press, 2007), 2nd ed. edn.

[29] Lu, R., Manzameque, T., Yang, Y. & Gong, S. S0-mode lithium niobate acoustic delay lines with 1 dB insertion loss. In *2018 IEEE International Ultrasonics Symposium (IUS)*, 1–9 (2018).

[30] Sarabalis, C. J., Hill, J. T. & Safavi-Naeini, A. H. Guided acoustic and optical waves in silicon-on-insulator for brillouin scattering and optomechanics. *APL PHOTONICS* **1**, (2016).

[31] Mirhosseini, M., Sipahigil, A., Kalaee, M. & Painter, O. Superconducting qubit to optical photon transduction. *Nature* **588**, 599+, (2020).

[32] Crespo-Poveda, A. *et al.* Acoustically driven arrayed waveguide grating. *Optics express* **23**, 21213–21231, (2015).

[33] Crespo-Poveda, A. *et al.* Synchronized photonic modulators driven by surface acoustic waves. *Optics express* **21**, 21669–21676, (2013).

[34] Tadesse, S. A. & Li, M. Sub-optical wavelength acoustic wave modulation of integrated photonic resonators at microwave frequencies. *NATURE COMMUNICATIONS* **5**, (2014).

[35] Tadesse, S. A., Li, H., Liu, Q. & Li, M. Acousto-optic modulation of a photonic crystal nanocavity with lamb waves in microwave k band. *APPLIED PHYSICS LETTERS* **107**, (2015).

[36] Sohn, D. B., Kim, S. & Bahl, G. Time-reversal symmetry breaking with acoustic pumping of nanophotonic circuits. *NATURE PHOTONICS* **12**, 91+, (2018).

[37] Li, H., Liu, Q. & Li, M. Electromechanical brillouin scattering in integrated planar photonics. *APL PHOTONICS* **4**, (2019).

[38] Liu, Q., Li, H. & Li, M. Electromechanical brillouin scattering in integrated optomechanical waveguides. *OPTICA* **6**, 778–785, (2019).

[39] Nguyen, L. T. & Tsai, C. S. Efficient wideband guided-wave acoustooptic bragg diffraction using phased surface acoustic wave array in $LiNbO_3$ waveguides. *Applied Optics* **16**, 1297–1304, (1977).

[40] Cheng, Z. Y. & Tsai, C. S. Baseband integrated acousto-optic frequency shifter. *Applied Physics Letters* **60**, 12–14, (1992).

[41] Tsai, C. Guided-wave acoustooptic bragg modulators for wide-band integrated optic communications and signal processing. *IEEE Transactions on Circuits and Systems* **26**, 1072–1098, (1979).

[42] Pinnow, D. Acousto-optic light deflection: Design considerations for first order beam steering transducers. *IEEE transactions on sonics and ultrasonics* **SU18**, 209–&, (1971).

[43] Zhao, H., Li, B., Li, H. & Li, M. Enabling scalable optical computing in synthetic frequency dimension using integrated cavity acousto-optics. *Nature Communications* **13**, 5426, (2022).

[44] COMSOL. Multiphysics reference manual, comsol, inc .

[45] Nye, J. F. Physical properties of crystals : their representation by tensors and matrices (1985).

[46] Weis, R. & Gaylord, T. Lithium niobate: summary of physical properties and crystal structure. *Applied Physics A Solids and Surfaces* **37**, 191–203, (1985).

[47] Tsai, C. *Guided-wave acousto-optics : interactions, devices, and applications* (Springer-Verlag, 1990).

[48] Sarabalis, C. J. *et al.* Acousto-optic modulation of a wavelength-scale waveguide (2020).

[49] Shao, L. *et al.* Microwave-to-optical conversion using lithium niobate thin-film acoustic resonators. *Optica* **6**, 1498–, (2019).

[50] Xiong, C. *et al.* Aluminum nitride as a new material for chip-scale optomechanics and nonlinear optics. *New journal of physics* **14**, 95014–, (2012).

[51] Balram, K. C., Davanco, M. I., Song, J. D. & Srinivasan, K. Coherent coupling between radiofrequency, optical and acoustic waves in piezo-optomechanical circuits. *Nature photonics* **10**, 346–352, (2016).

[52] Modica, G. *et al.* Slow propagation of 2 GHz acoustical waves in a suspended GaAs phononic waveguide on insulator. *Applied physics letters* **117**, 193501–, (2020).

[53] Fu, W. *et al.* Phononic integrated circuitry and spin-orbit interaction of phonons. *Nature communications* **10**, 2743–7, (2019).

[54] Hönl, S. *et al.* Microwave-to-optical conversion with a gallium phosphide photonic crystal cavity. *Nature communications* **13**, 2065–2065, (2022).

[55] RUMYANTSEV, S. L., SHUR, M. S. & LEVINSHTEIN, M. E. MATERIALS PROPERTIES OF NITRIDES: SUMMARY. *International journal of high speed electronics* **14**, 1–19, (2004).

[56] Ruppel, C. C. W. Acoustic wave filter technology-a review. *IEEE transactions on ultrasonics, ferroelectrics, and frequency control* **64**, 1390–1400, (2017).

[57] Malocha, D. Evolution of the SAW transducer for communication systems. In *IEEE Ultrasonics Symposium, 2004*, vol. 1, 302–310 Vol.1 (IEEE, 2004).

[58] Datta, S. *Surface acoustic wave devices* (Prentice-Hall, 1986).

[59] Hashimoto, K.-y. *Surface acoustic wave devices in telecommunications : modelling and simulation* (Springer, 2000).

[60] Yu, Z. & Sun, X. Acousto-optic modulation of photonic bound state in the continuum. *Light, science & applications* **9**, 1–1, (2020).

[61] Shao, L. *et al.* Integrated microwave acousto-optic frequency shifter on thin-film lithium niobate. *Optics express* **28**, 23728–23738, (2020).

[62] Kapfinger, S. *et al.* Dynamic acousto-optic control of a strongly coupled photonic molecule. *Nature communications* **6**, 8540–8540, (2015).

[63] Li, H., Tadesse, S. A., Liu, Q. & Li, M. Nanophotonic cavity optomechanics with propagating acoustic waves at frequencies up to 12 GHz. *Optica* **2**, 826–831, (2015).

[64] Fan, L. *et al.* Integrated optomechanical single-photon frequency shifter. *Nature photonics* **10**, 766–770, (2016).

[65] MacCabe, G. S. *et al.* Nano-acoustic resonator with ultralong phonon lifetime. *Science (American Association for the Advancement of Science)* **370**, 840–843, (2020).

[66] Sohn, D. B., Örsel, O. E. & Bahl, G. Electrically driven optical isolation through phonon-mediated photonic autler–townes splitting. *Nature photonics* **15**, 822–827, (2021).

[67] Balram, K. C. *et al.* Acousto-optic modulation and optoacoustic gating in piezo-optomechanical circuits. *Physical review applied* **7**, (2017).

[68] Bochmann, J., Vainsencher, A., Awschalom, D. D. & Cleland, A. N. Nanomechanical coupling between microwave and optical photons. *Nature physics* **9**, 712–716, (2013).

[69] Amann, M., Bosch, T., Lescure, M., Myllyla, R. & Rioux, M. Laser ranging: a critical review of usual techniques for distance measurement. *Optical engineering* **40**, 10–19, (2001).

[70] Berkovic, G. & Shafir, E. Optical methods for distance and displacement measurements. *ADVANCES IN OPTICS AND PHOTONICS* **4**, 441–471, (2012).

[71] Schwarz, B. Mapping the world in 3d. *Nat. Photon* **4**, 429–430, (2010).

[72] Kim, I. *et al.* Nanophotonics for light detection and ranging technology. *NATURE NANOTECHNOLOGY* **16**, 508–524, (2021).

[73] Sun, J., Timurdogan, E., Yaacobi, A., Hosseini, E. S. & Watts, M. R. Large-scale nanophotonic phased array. *NATURE* **493**, 195–199, (2013).

[74] Poulton, C. V. *et al.* Coherent solid-state LIDAR with silicon photonic optical phased arrays. *OPTICS LETTERS* **42**, 4091–4094, (2017).

[75] Liu, Y. & Hu, H. Silicon optical phased array with a 180-degree field of view for 2d optical beam steering. *OPTICA* **9**, 903–907, (2022).

[76] Hutchison, D. N. *et al.* High-resolution aliasing-free optical beam steering. *OPTICA* **3**, 887–890, (2016).

[77] McManamon, P. *et al.* Optical phased array technology. *PROCEEDINGS OF THE IEEE* **84**, 268–298, (1996).

[78] Shaltout, A. M. *et al.* Spatiotemporal light control with frequency-gradient metasurfaces. *SCIENCE* **365**, 374+, (2019).

[79] Li, S.-Q. *et al.* Phase-only transmissive spatial light modulator based on tunable dielectric metasurface. *SCIENCE* **364**, 1087+, (2019).

[80] Zhang, X., Kwon, K., Henriksson, J., Luo, J. & Wu, M. C. A large-scale microelectromechanical-systems-based silicon photonics LiDAR. *Nature* **603**, 253–258, (2022).

[81] Rogers, C. *et al.* A universal 3d imaging sensor on a silicon photonics platform. *NATURE* **590**, (2021).

[82] Trocha, P. *et al.* Ultrafast optical ranging using microresonator soliton frequency combs. *SCIENCE* **359**, 887–891, (2018).

[83] Riemensberger, J. *et al.* Massively parallel coherent laser ranging using a soliton microcomb. *NATURE* **581**, 164+, (2020).

[84] Jiang, Y., Karpf, S. & Jalali, B. Time-stretch LiDAR as a spectrally scanned time-of-flight ranging camera. *NATURE PHOTONICS* **14**, 14+, (2020).

[85] Korpel, A. *Acousto-Optics, Second Edition* (CRC Press, 1996).

[86] Lohmann, A., Dorsch, R., Mendlovic, D., Zalevsky, Z. & Ferreira, C. Space-bandwidth product of optical signals and systems. *Journal of the Optical Society of America. A, Optics and image science* **13**, 470–473, (1996).

[87] Hinkov, V. Proton exchanged waveguides for surface acoustic waves on LiNbO3. *Journal of applied physics* **62**, 3573–3578, (1987).

[88] Bajak, I. L., McNab, A., Richter, J. & Wilkinson, C. D. W. Attenuation of acoustic waves in lithium niobate. *The Journal of the Acoustical Society of America* **69**, 689–695, (1981).

[89] Mayor, F. M. *et al.* Gigahertz phononic integrated circuits on thin-film lithium niobate on sapphire. *PHYSICAL REVIEW APPLIED* **15**, (2021).

[90] Xu, Y. *et al.* Bidirectional interconversion of microwave and light with thin-film lithium niobate. *NATURE COMMUNICATIONS* **12**, (2021).

[91] Endres, M. *et al.* Atom-by-atom assembly of defect-free one-dimensional cold atom arrays. *SCIENCE* **354**, 1024–1027, (2016).

[92] Lehtonen, S., Plessky, V., Hartmann, C. & Salomaa, M. Unidirectional SAW transducer for gigahertz frequencies. *IEEE transactions on ultrasonics, ferroelectrics, and frequency control* **50**, 1404–1406, (2003).

[93] Zhang, M., Wang, C., Kharel, P., Zhu, D. & Loncar, M. Integrated lithium niobate electro-optic modulators: when performance meets scalability. *OPTICA* **8**, 652–667, (2021).

[94] Joannopoulos, J. D., Johnson, S. G., Winn, J. N. & Meade, R. D. *Molding the flow of light* (Princeton Univ. Press, Princeton, NJ [ua], 2008).

[95] Shankar, R. *Principles of quantum mechanics* (Springer Science & Business Media, 2012).

[96] Prucnal, P. R. *Neuromorphic photonics* (CRC Press, 2017).

[97] Caulfield, H. J. & Dolev, S. Why future supercomputing requires optics. *Nature photonics* **4**, 261–263, (2010).

[98] Solli, D. R. & Jalali, B. Analog optical computing. *Nature photonics* **9**, 704–706, (2015).

[99] Liu, W. *et al.* A fully reconfigurable photonic integrated signal processor. *Nature photonics* **10**, 190–195, (2016).

[100] Nahmias, M. A. *et al.* Photonic multiply-accumulate operations for neural networks. *IEEE journal of selected topics in quantum electronics* **26**, 1–18, (2020).

[101] Hamerly, R., Bernstein, L., Sludds, A., Soljačić, M. & Englund, D. Large-scale optical neural networks based on photoelectric multiplication. *Physical review. X* **9**, 021032–, (2019).

[102] Mohammadi Estakhri, N., Edwards, B. & Engheta, N. Inverse-designed metastructures that solve equations. *Science (American Association for the Advancement of Science)* **363**, 1333–1338, (2019).

[103] Lin, X. *et al.* All-optical machine learning using diffractive deep neural networks. *Science (American Association for the Advancement of Science)* **361**, 1004–1008, (2018).

[104] Spall, J., Guo, X., Barrett, T. D. & Lvovsky, A. I. Fully reconfigurable coherent optical vector–matrix multiplication. *Optics letters* **45**, 5752–5755, (2020).

[105] Zhou, T. *et al.* Large-scale neuromorphic optoelectronic computing with a reconfigurable diffractive processing unit. *Nature photonics* **15**, 367–373, (2021).

[106] Shen, Y. *et al.* Deep learning with coherent nanophotonic circuits. *Nature photonics* **11**, 441–446, (2017).

[107] Tait, A. N. *et al.* Silicon photonic modulator neuron. *Physical review applied* **11**, (2019).

[108] Bogaerts, W. *et al.* Programmable photonic circuits. *Nature (London)* **586**, 207–216, (2020).

[109] Xu, X. *et al.* 11 TOPS photonic convolutional accelerator for optical neural networks. *Nature (London)* **589**, 44–51, (2021).

[110] Feldmann, J. *et al.* Parallel convolutional processing using an integrated photonic tensor core. *Nature (London)* **589**, 52–58, (2021).

[111] Liu, H., Dai, Z., So, D. R. & Le, Q. V. Pay attention to MLPs (2021).

[112] Ozawa, T., Price, H. M., Goldman, N., Zilberberg, O. & Carusotto, I. Synthetic dimensions in integrated photonics: From optical isolation to four-dimensional quantum hall physics. *Physical review. A* **93**, (2016).

[113] Lukens, J. M. & Lougovski, P. Frequency-encoded photonic qubits for scalable quantum information processing. *Optica* **4**, 8–16, (2017).

[114] Yuan, L., Lin, Q., Xiao, M. & Fan, S. Synthetic dimension in photonics. *Optica* **5**, 1396–1405, (2018).

[115] Bell, B. A. *et al.* Spectral photonic lattices with complex long-range coupling. *Optica* **4**, 1433–1436, (2017).

[116] Titchener, J. G. *et al.* Synthetic photonic lattice for single-shot reconstruction of frequency combs. *APL photonics* **5**, 30805–030805–7, (2020).

[117] Dutt, A. *et al.* A single photonic cavity with two independent physical synthetic dimensions. *arXiv.org* (2019).

[118] Tusnin, A. K., Tikan, A. M. & Kippenberg, T. J. Nonlinear states and dynamics in a synthetic frequency dimension. *Physical review. A* **102**, (2020).

[119] Buddhiraju, S., Dutt, A., Minkov, M., Williamson, I. A. D. & Fan, S. Arbitrary linear transformations for photons in the frequency synthetic dimension. *Nature communications* **12**, 2401–2401, (2021).

[120] Forsch, M. *et al.* Microwave-to-optics conversion using a mechanical oscillator in its quantum ground state. *Nature physics* **16**, 69–74, (2020).

[121] Jiang, W. *et al.* Efficient bidirectional piezo-optomechanical transduction between microwave and optical frequency. In *2020 Conference on Lasers and Electro-Optics (CLEO)*, 1–2 (OSA, 2020).

[122] Tian, H. *et al.* Hybrid integrated photonics using bulk acoustic resonators. *Nature communications* **11**, 3073–3073, (2020).

[123] Schuelein, F. J. R. *et al.* Fourier synthesis of radiofrequency nanomechanical pulses with different shapes. *Nature nanotechnology* **10**, 512–516, (2015).

[124] Weiss, M. *et al.* Multiharmonic frequency-chirped transducers for surface-acoustic-wave optomechanics (2018).

[125] Kues, M. *et al.* On-chip generation of high-dimensional entangled quantum states and their coherent control. *Nature (London)* **546**, 622–626, (2017).

[126] Weiss, M. *et al.* Multiharmonic frequency-chirped transducers for surface-acoustic-wave optomechanics. *Physical review applied* **9**, 014004–, (2018).

[127] Kues, M. *et al.* Quantum optical microcombs. *Nature photonics* **13**, 170–179, (2019).

[128] Beugnot, J.-C., Sylvestre, T., Maillotte, H., Melin, G. & Laude, V. Guided acoustic wave brillouin scattering in photonic crystal fibers. *OPTICS LETTERS* **32**, 17–19, (2007).

[129] Kang, M. S., Brenn, A. & Russell, P. S. J. All-optical control of gigahertz acoustic resonances by forward stimulated interpolarization scattering in a photonic crystal fiber. *PHYSICAL REVIEW LETTERS* **105**, (2010).

[130] Van Laer, R., Kuyken, B., Van Thourhout, D. & Baets, R. Interaction between light and highly confined hypersound in a silicon photonic nanowire. *NATURE PHOTONICS* **9**, 199–203, (2015).

[131] Smalley, D. E., Smithwick, Q. Y. J., Bove, V. M., Jr., Barabas, J. & Jolly, S. Anisotropic leaky-mode modulator for holographic video displays. *NATURE* **498**, 313+, (2013).

[132] Van Laer, R., Baets, R. & Van Thourhout, D. Unifying brillouin scattering and cavity optomechanics. *PHYSICAL REVIEW A* **93**, (2016).

[133] Sarabalis, C. J., Van Laer, R. & Safavi-Naeini, A. H. Optomechanical antennas for on-chip beam-steering. *OPTICS EXPRESS* **26**, 22075–22099, (2018).

[134] Tanaka, Y., Yoshida, H. & Kurokawa, T. Guided-acoustic-wave brillouin scattering observed backward by stimulated brillouin scattering. *Measurement science & technology* **15**, 1458–1461, (2004).

[135] Behroozpour, B., Sandborn, P. A. M., Wu, M. C. & Boser, B. E. Lidar system architectures and circuits. *IEEE communications magazine* **55**, 135–142, (2017).

[136] Wang, J. *et al.* Multidimensional quantum entanglement with large-scale integrated optics. *Science (American Association for the Advancement of Science)* **360**, 285–291, (2018).

[137] Kittlaus, E. A. *et al.* Electrically driven acousto-optics and broadband non-reciprocity in silicon photonics. *Nature photonics* **15**, 43–52, (2020).

[138] Zhang, H. *et al.* An optical neural chip for implementing complex-valued neural network. *Nature communications* **12**, 457–457, (2021).

[139] Li, H. *et al.* Chapter fourteen - electromechanical brillouin scattering. In Eggleton, B. J., Steel, M. J. & Poulton, C. G. (eds.) *Brillouin Scattering Part 2*, vol. 110 of *Semiconductors and Semimetals*, 287–311 (Elsevier).